

Characterization of Uncertainty
in Measurements of Wind
from the NSF/NCAR Gulfstream V Research Aircraft

Al Cooper, Dick Friesen (and, eventually, many others)

DRAFT 2/16/2015

Contents

1	Introduction	4
2	Components of the wind-sensing systems	5
2.1	General comments	5
2.2	The radome-based system	7
2.3	The gust-pod system	16
2.4	The laser air-motion sensor (LAMS)	25
3	Schuler correction for pitch	26
3.1	Basis for the correction	26
3.2	Simple illustration of Schuler oscillation	26
3.3	Illustrative example	30
3.4	Transformation of attitude angles	32
3.5	Application to research flights	33
3.6	Tests of the correction	33
4	Sensitivity coefficients	40
4.1	Angle of Attack	40
4.2	Sideslip Angle	52
4.3	True Airspeed from the Gust Pod	56
4.4	Summary of sensitivity coefficients	60
5	Studies of the Vertical Wind	61
5.1	Overview	61
5.2	The vertical velocity of the aircraft	61
5.3	Timing of measurements	68
6	Studies of the Horizontal Wind	71
6.1	Analysis of circle maneuvers	71
6.2	The complementary filter	83
7	Uncertainty components and summary	86
7.1	Radome-based system	86
7.2	Gust-pod system	92

8 Net uncertainty in measurements of wind	93
9 Potential for improvement in measurement of wind	94

1 Introduction

This report documents how measurements of wind are made from the NSF/NCAR Gulfstream V research aircraft (hereafter, GV) and provides a characterization of the uncertainty associated with those measurements. The characterization applies to the system as it existed in 2014, in particular as it operated in the DEEPWAVE research project flown from New Zealand in June-July 2014. Key aspects influencing the uncertainty in the measurements as characterized here are the presence of “OmniSTAR” GPS (Global Positioning System) measurements, providing measurements of the velocity of the aircraft relative to the earth, a calibration of airspeed provided by the Laser Air Motion Sensor (Cooper et al. [2014]), and a newly developed all-weather wind sensor or “gust pod” employing a Rosemount 858 probe mounted under the wing of the GV. These complemented the standard wind-sensing system comprised of a Honeywell Laseref IV inertial reference unit, GPS measurements from Novatel and Garmin units, and a gust-sensing system based on pressure ports in the nose radome. The results obtained here do not necessarily apply to measurements from earlier projects when not all these components were available in their present form.

Section 2 describes the components of the wind-measuring system in more detail, and Section 4 summarizes how the measurements have been calibrated, tested, and intercompared. Some related studies affecting the measurements are then presented in the next sections. This information all provides the basis for Section 7, where the contributions to uncertainty from various sources are tabulated and where there is a discussion of the basis for each estimate contributing to uncertainty in the measured wind. That section then concludes with a summary characterizing the overall uncertainty and the separate systematic and random components included in that uncertainty.

The program that performed the calculations reported here can be found on NCAR/EOL computer space in the directory /h/eol/cooperw/RStudio/DEEPWAVE/WindUncertainty and in the GitHub repository <https://github.com/WilliamCooper/WindUncertainty.git>. The former is accessible via computers like tikal.eol.ucar.edu. The main program is WindUncertainty.Rnw; other files in those repositories with suffixes .Rnw are sections in this report and are linked to the main program. Normal usage is to run this main program within “RStudio” to execute the contained R code and also, via “knitr,” to generate this text document from LaTeX statements embedded in those files. An R package ‘Ranadu’ is used extensively in the R code; it resides on GitHub as <https://github.com/WilliamCooper/Ranadu.git>. The data used reside in NCAR/EOL project archives and, in subsetted form, are archived in the directory /h/eol/cooperw/STudio/DEEPWAVE/WindUncertainty as R data files, with names ending in “Rdata.” Those files are too large to be appropriate for GitHub but can be provided from the NCAR/EOL computers. It is thus possible to reproduce this document from archived data and to repeat the included analyses with new data as needed. This document thus attempts to be “reproducible research” as that term is used by the author of knitr. References for knitr and the analysis packages in R are included in the Acknowledgements and References at the end of this document.

2 Components of the wind-sensing systems

2.1 General comments

2.1.1 Overview

Three wind-sensing systems are available for use on the GV:

1. The “standard” wind sensing system that uses pressure ports on the radome combined with airspeed measured using a pitot tube and ground-speed measured by an inertial reference unit and a global positioning system (GPS) receiver.
2. A gust-pod system consisting of a Rosemount 858 airflow sensor mounted under the wing combined with an inertial system co-located with the airflow sensor and linked to GPS measurements via a Kalman filter.
3. A laser air motion sensor described by [Spuler et al. \[2011\]](#) combined with its own IRU/GPS system. See also [Cooper et al. \[2014\]](#).

Although the measurement components differ, for each of these the measurement of wind involves the vector sum of two components, the motion of the air relative to the aircraft and the motion of the aircraft relative to the Earth. The former is the “relative wind” and is measured as a three-component vector having magnitude equal to the “true airspeed” and angles relative to the aircraft reference frame characterized by the angle of attack and the sideslip angle. The angle of attack is considered positive if the relative wind is from below the aircraft, and the sideslip angle is considered positive if the relative wind is from the starboard side of the aircraft. The relative wind defined in the coordinate system of the aircraft (conventionally with \hat{x}' forward, \hat{y}' in the starboard direction, and \hat{z}' obtained from the cross product $\hat{x}' \times \hat{y}'$ and so approximately downward but oriented to align with the aircraft reference frame) must be transformed to an Earth-based reference system (conventionally with \hat{x} toward east, \hat{y} toward north, and \hat{z} upward) so that the components can be combined to yield the Earth-relative wind. This transformation is a function of the attitude angles of the aircraft, heading (ψ), pitch (θ), and roll (ϕ), measured by an inertial reference unit in all three cases discussed here. Once in an Earth-based reference system, the relative wind vector is added to the vector representing the aircraft motion relative to the Earth to obtain the wind. The sources of the various measurements entering this processing sequence vary among the three systems and will be discussed separately below for each system.

2.1.2 The Relative Wind

In the standard aircraft coordinate system with x forward, y starboard, and z downward, the three corresponding components of the relative wind \mathbf{v} (cf. [Lenschow \[1972\]](#) and [RAF Bulletin 23](#)) are:

$$\mathbf{v} = \begin{pmatrix} u_r \\ v_r \\ w_r \end{pmatrix} = \begin{pmatrix} V^* \\ V^* \tan \beta \\ V^* \tan \alpha \end{pmatrix} \quad (1)$$

where, if V is the true airspeed, $V^* = V / \sqrt{1 + \tan^2 \alpha + \tan^2 \beta}$ is the component of true airspeed along the aircraft longitudinal (x) axis, α is the angle of attack and β the sideslip angle. The sign convention is such that the relative wind is positive when *from* the direction of the axis for each component. (The magnitude of \mathbf{v} is thus V as required.) The relative wind is therefore determined from measurements of true airspeed, angle of attack, and sideslip angle.

2.1.3 Transformation to an Earth Reference Frame

The orientations of the aircraft, the gust pod, and the LAMS are measured by IRUs located respectively in the fuselage and in the pod itself. Each independently measures heading, pitch, and roll, so the calculations of wind from the three systems can be fully independent except that, because it is considered to have the smallest uncertainty, the true airspeed measured from the fuselage system is used also for the gust pod. In each case, the IRU measurements and GPS ground-speed components are used to transform the measurements to the reference frame of the Earth.

The required transformation is described by three rotation matrices, defined in [RAF Bulletin 23](#) Eqs. 2.5 and 2.6:

$$\mathbf{T}_1 = \begin{pmatrix} 1 & 0 & 0 \\ 0 & \cos \phi & -\sin \phi \\ 0 & \sin \phi & \cos \phi \end{pmatrix}$$

$$\mathbf{T}_2 = \begin{pmatrix} \cos \theta & 0 & \sin \theta \\ 0 & 1 & 0 \\ -\sin \theta & 0 & \cos \theta \end{pmatrix}$$

$$\mathbf{T}_3 = \begin{pmatrix} \cos \psi & -\sin \psi & 0 \\ \sin \psi & \cos \psi & 0 \\ 0 & 0 & 1 \end{pmatrix}$$

where $\{\phi, \theta, \psi\}$ are $\{\text{roll}, \text{pitch}, \text{heading}\}$.

The transformation needs to be in the following order to conform to conventional definitions of the attitude angles:

1. Rotate by \mathbf{T}_1 using the roll angle ϕ (ROLL or CROLL_GP) to level the wings by a rotation about the x axis.
2. Rotate by \mathbf{T}_2 using the pitch angle θ (PITCH or CPITCH_GP) to level the aircraft by a rotation about the y axis.
3. Rotate by \mathbf{T}_3 using the heading angle ψ (THDG or CTHDG_GP) to obtain components in a true-north reference frame. At this point, the relative-wind vector in an Earth-reference coordinate system is $\mathbf{v}_r = \mathbf{T}_3(\mathbf{T}_2(\mathbf{T}_1\mathbf{v}))$ where \mathbf{v} is given by (1).

The measured ground-speeds (with components VNS, VEW, VSPD) then can be added to the relative wind to get the true Earth-relative wind. In the “R” file associated with this document, the required transformations are coded to provide a processing option, but the conventional “nimbus” routine “gust.c” provides the transformation as implemented in standard processing.

The final equations, defining the Earth-relative wind \mathbf{v}_E in terms of the three wind variables {WD_x, WS_x, WI_x} where x denotes the measuring system (and subscript-x the east component of the wind), are:

$$\mathbf{v}_E = \mathbf{v}_r + \begin{pmatrix} -VNS_x \\ -VEW_x \\ VSPD_x \end{pmatrix} \quad (2)$$

$$WD_x = \arctan 2(v_{E,y}, v_{E,x}) \quad (3)$$

$$WS_x = \sqrt{(v_{E,x}^2 + v_{E,y}^2)} \quad (4)$$

$$WI_x = v_{E,z} \quad (5)$$

2.2 The radome-based system

2.2.1 Overview

The primary measurement on the GV is that based on measurement of true airspeed via a pitot tube, airflow angles via pressure differences measured on the nose radome, attitude angles measured by an inertial reference unit, and ground-speed components measured by the same inertial reference unit and also by a Global Positioning System receiver. A cursory description of this system was provided by [Cooper et al. \[2014\]](#). A more extensive description will be provided here. Table 1 provides a summary of the measurements used to determine the wind and the characteristics of the sensors used, and the [EOL instrument web pages](#) provide additional information on these measurements.

XXX

2.2.2 Attitude angles

Attitude angles (roll, pitch, and heading) are provided by the IRU discussed in the preceding sub-section, with specifications as listed in Table 1. There are duplicate inertial systems, so a measure of uncertainty is how well they agree. For the period 3:00:00–6:00:00 on DEEPWAVE flight 15, the mean difference in pitch was 0.1° and the standard deviation in the difference between measurements was also about 0.12°, but if measurements are restricted to times where the magnitude of the roll is less than 5° then the standard deviation is only 0.017°. This may be an indication that the system performs better than indicated by the specifications, and indeed additional evidence for this is provided in Section 3. The difference in pitch and enhanced standard deviation in turns likely arise from small mis-alignment of the units relative to the longitudinal axis of the aircraft.

Measurement (VARIABLE)	Instrument	Range, Char- acteristics	Standard Uncertainty	Comments
pitch, roll (PITCH, ROLL)	Laseref IV Model HG2001 GD03	ring gyros, strap-down system	0.05°	mixed bias and random error
heading (THDG)	"		0.2°	
ambient pressure (PSF)	absolute transducer Paroscientific 1000-15A-28	0–15 PSI \approx 0–1035 hPa	0.10 hPa	(from specs, assumed to give std uncertainty)
dynamic pressure (QCF, QCR)	differential transducer PPT0005DXX2VB- 5021	0–5 PSI \approx 0–345 hPa	0.34 hPa 0.68 hPa max.	"
pressure differences, radome (ADIFR, BDIFR)	differential transducer PPT0001DXX2VB- 5021	range \pm 1 PSI \approx \pm 68.95 hPa	0.07 hPa 0.14 hPa max.	the first is "typ.", average over the range
horizontal GV velocity components (VNS, VEW)	Laseref IV Model HG2001 GD03	strap-down ac- celerometers	2.1 m s ⁻¹	0.1 m s ⁻¹ with slom updating to GPS
" "" " (GGVNS, GGIEW)	Novatel OEM-3 differential GPS	(L1/L2) correction via OmniSTAR XP	0.03 m s ⁻¹	<0.1 m s ⁻¹ when OmniSTAR is not available
vertical GV speed (VSPD)	Laseref IV (see above)		0.76 m s ⁻¹	with baro-loop updating
" "" " (GGVSPD)	Novatel GPS (see above)		0.03 m s ⁻¹ with OmniSTAR	0.1 m s ⁻¹ without OmniSTAR
air temperature	HARCO 100009-1	anti-iced, -80 to +40°C	0.3°C	needed for TAS calc.

Table 1: Characteristics of measurements from the radome-based system that are used for the standard calculation of the wind. See further discussion of each measurement in Sect. 2.2.

2.2.3 Ambient pressure

Ambient or “static” pressure is measured on the GV at pressure ports called static buttons that are located at positions on the fuselage where in normal flight the pressure is approximately the pressure present outside the airflow disturbance produced by the aircraft. Because there are residual effects of airflow that change with angle of attack and Mach number, corrections are applied to these measurements to obtain better representation of the true ambient pressure. These corrections are described in [this document on processing algorithms](#), Sect. 4.3, and in [Cooper et al. \[2014\]](#). The latter reference has additional information on the locations of the sensors and the system configuration. The transducer characteristics are listed in Table 1, and the transducer is temperature-compensated to maintain these characteristics in flight when the cabin-mounted transducer can encounter fluctuating temperature. It is a digital transducer with resolution of 0.001 hPa, equivalent to about 20-bit resolution, when sampling at 1 Hz. The characteristic response time of the sensor is 0.02 s and measurements are normally sampled at 50 Hz and filtered to 25 Hz. However, lines of length XXX and diameter XXX connect the transducer to the static buttons, and these lines affect the response time significantly, as discussed in Sect. . More information is available on the EOL instrument pages; see [this link](#). XXX XXX

2.2.4 Dynamic pressure

The dynamic pressure is the pressure difference above ambient that develops if air is compressed and adiabatically brought to rest relative to the moving aircraft. The total pressure, the sum of ambient and dynamic pressure, is sensed using a pitot tube, a tube pointed in the direction of the relative airflow and specially designed to be relatively insensitive to small-angle changes in the direction of the relative airflow. Figure 1 shows the location of the research-system pitot tube on the GV as well as one of the avionics-system pitot tubes. The excess pressure above the ambient sensed by a pitot tube or, approximately, by the center port on the radome is equal to 0.5 times the air density times the airspeed squared, so this excess pressure can be used to determine the airspeed of the aircraft. On NSF/NCAR aircraft, the measurement of dynamic pressure is made using differential sensors connected between a static source and a total-pressure source from either a pitot tube (QCF) or the front port on the radome (QCR). The sensor used, with characteristics listed in Table 1, has these additional characteristics: Specified resolution is 0.0011% of full scale or 0.0076 hPa, which is better than 16-bit resolution; maximum sampling rate 120 Hz; response time 50ms and response delay 21 ms at 50 Hz sample rate, or about one sample period. The response time is affected further by the pressure lines between the pressure ports and the transducers; see Sect. XXX for discussion of this effect. The transducer provides XXX 50-Hz output that is then filtered digitally to 25 Hz or 1 Hz in processing.¹

Because any errors affecting the measurement of static pressure also affect the difference between dynamic and static pressure, the same corrections that are applied to static pressure (for errors in the pressure delivered by the static ports) are also applied to the dynamic pressure. See

¹The specifications indicate that the appropriate time lag to apply in processing would be 21 ms but there is additional delay introduced by the sample tubing. Most processing including preliminary processing for DEEPWAVE has not introduced a delay for QCF or QCR.

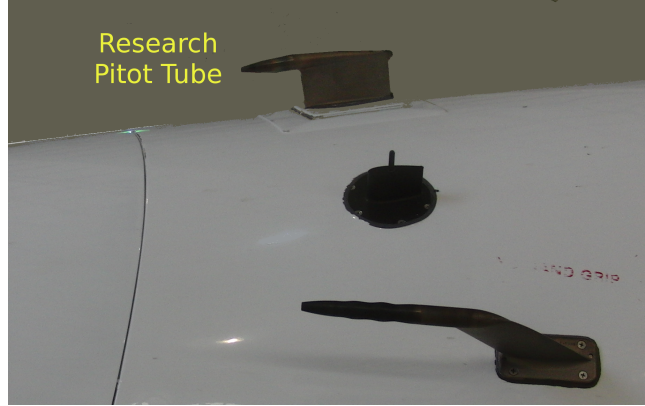


Figure 1: A pitot tube used for the measurement of dynamic pressure.

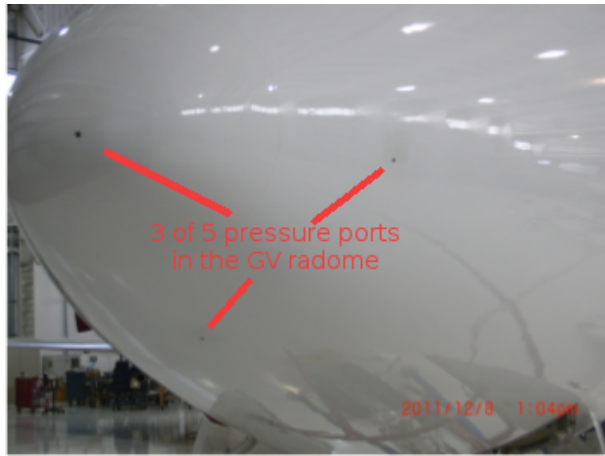


Figure 2: Photograph of the GV radome showing three of the five pressure ports on the radome used for measurement of components of the relative wind.

the EOL instrument pages for more information. Cooper et al. [2014] argue that the measurements of static and dynamic pressure, corrected for flow distortion or generation of a “static defect” at the static-pressure ports, each have standard uncertainty of 0.3 hPa and precision (for straight and level flight) of 0.1 hPa.

2.2.5 Airflow angles

The radome gust-sensing system consists of five pressure ports installed in a standard GV radome, as shown in Fig. 2. The pressure ports are connected to differential pressure sensors, one between the top and bottom ports (variable ADIFR), one between the left and right ports (variable BDIFR), and one between the center port and the static source (variable QCR). The latter provides an alternative measurement of dynamic pressure but is not normally used. The measurements ADIFR and BDIFR are obtained from differential pressure transducers, with characteristics as shown in Table 1. The transducers have specified response times of 0.05 s and resolution 0.0015 hPa, with quoted stability of about 0.03 hPa per year. These measurements are

used with procedures discussed in Section 4.1.2 to find the angle of attack and sideslip angle of the relative wind. Additional information is available at [this URL](#).

2.2.6 Components of aircraft velocity relative to the Earth

There are two sources of information regarding the ground-speed vector, an inertial reference unit (IRU) and a Global Positioning System (GPS).

1. **The IRU:** The inertial system on the GV is a Honeywell Laseref IV Model HG2001 GD03, with characteristics as listed in Table 1. There are three units on the aircraft, two of which are recorded via the ARINC data bus to standard data files. These are strap-down ring laser gyro micro inertial systems. The measurements of ground-speed components are affected by errors that arise from initial alignment errors or orientation errors resulting from gyro responses to acceleration and so often exhibit a characteristic Schuler oscillation with magnitude that can be as much as $1\text{--}3 \text{ m s}^{-1}$. This is the primary source of error in the measurements, so for aircraft velocity components it is important to remove these errors by comparison to lower-uncertainty measurements provided by the GPS that are not subject to the Schuler oscillation. In addition, there are signal delays that are accounted for in post processing to align measurements with other recorded data, and there are some inherent filters in the IRU computer that affect the signals transmitted to the GV data system. The orientation of this unit was defined and checked by initial survey to coincide with the aircraft reference axes.
2. **The GPS:** The primary GPS unit is a Novatel OEM-3 differential GPS unit (L1/L2) with OmniSTAR XP satellite update for (ionospheric) corrections. As used on the GV, it reports ground-speed components at a rate of 5 Hz, although faster rates are possible. The claimed standard uncertainty for position is 0.15 m for vertical position; the standard uncertainty in velocity is 0.03 m s^{-1} when OmniSTAR corrections are available and $<0.1 \text{ m s}^{-1}$ otherwise.

XXX

2.2.7 Temperature

A measurement of temperature is needed to calculate the wind because the conversion from dynamic pressure to true airspeed involves the temperature, as documented in [this document on processing algorithms](#). The measurements of temperature were checked against expectations for height-vs-pressure changes from the hydrostatic equation by [Cooper et al. \[2014\]](#), with the result that the measurements were validated to an uncertainty of about 0.3°C . Documentation of the temperature uncertainty will be presented in more detail in a separate document, but at this level of uncertainty the measurement of temperature will be shown to introduce negligible uncertainty to the measurement of wind. XXX

XXX

2.2.8 Examples of measurements

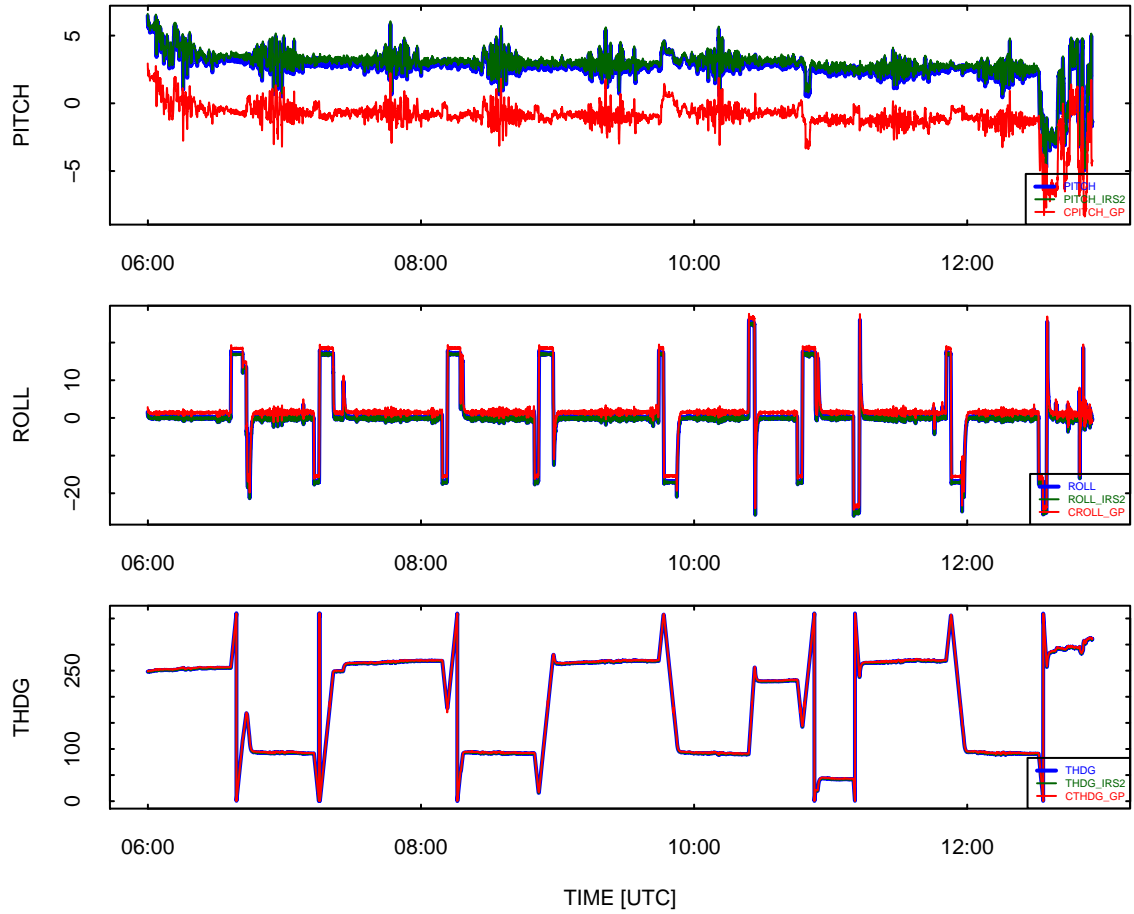


Figure 3: Attitude angles pitch, roll, and heading as measured by three independent systems, the standard Honeywell IRU (blue lines), a duplicate backup Honeywell IRU (green lines), and the C-MIGITS IRU mounted in the gust pod (red line). All plot units are degrees. Data from DEEPWAVE flight 16 (4 July 2014).

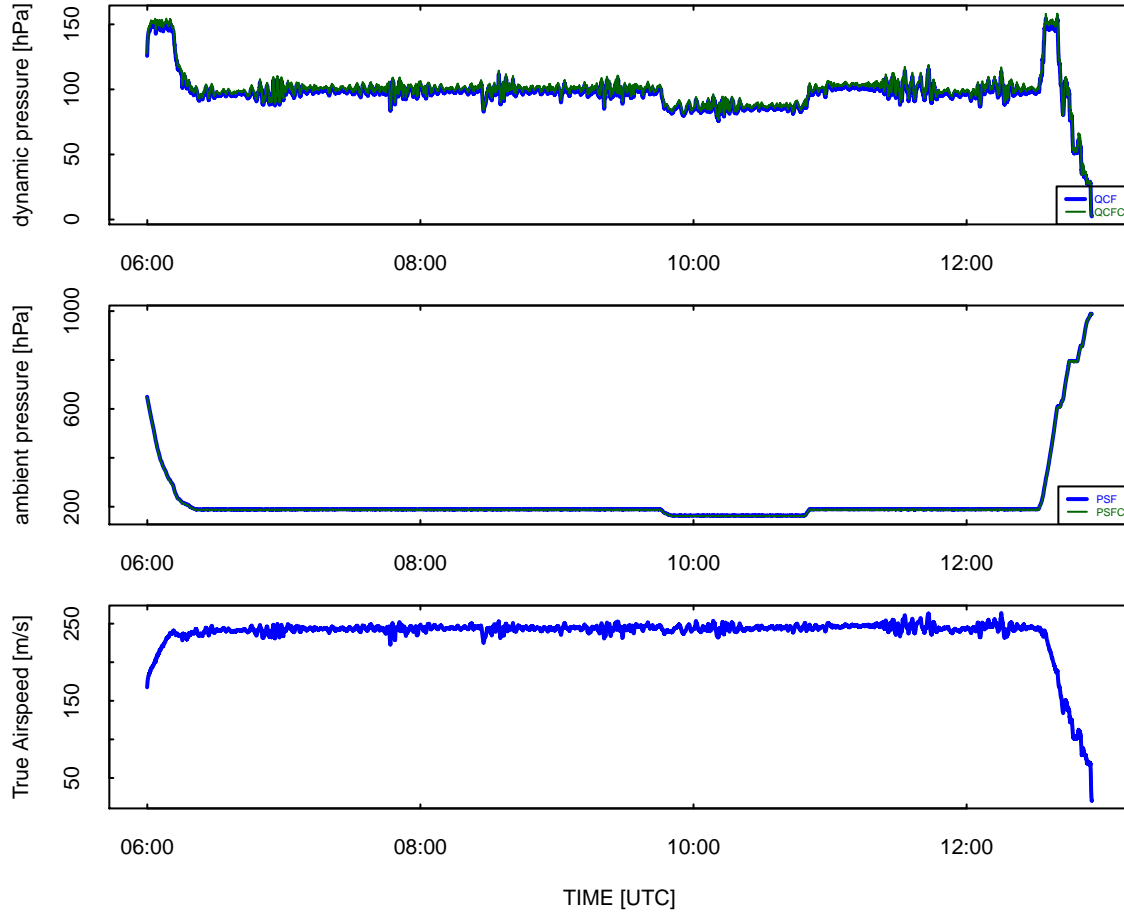


Figure 4: The measurements of dynamic pressure (QCF and, after correction QCFC), ambient pressure (PSF and corrected PSFC) and the resulting true airspeed TASX. Data from DEEP-WAVE flight 16.

Typical measurements of the attitude angles are shown in Fig. 3. The large difference in pitch is a result of the gust pod being installed in a canister below the wind where it points downward by several degrees relative to the aircraft longitudinal axis. (The pods were designed this way to provide better approaching airflow for cloud-imaging probes and other sampling from the airstream.) There is also a significant difference in heading and in roll for similar reasons.

The measurements of pressures and the true airspeed calculated from these measurements are shown in Fig. 4 for the same period as in the preceding figure. Corrections have been applied to the pressure measurements according to the calibration determined from LAMS measurements, as described by [Cooper et al. \[2014\]](#); these corrections vary with flight conditions but normally are smaller than a few hPa so are not evident in these plots. They are nevertheless crucial to reducing the uncertainty in the true airspeed to about 0.3 m s^{-1} , as shown in that reference.

Figure 5 shows the measurements of differential pressure at the radome and the resulting angle-of-attack and sideslip angle calculated from those pressure differences. The calculation is described in Section 4 of this document. Fluctuations in sideslip angle are seldom more than a

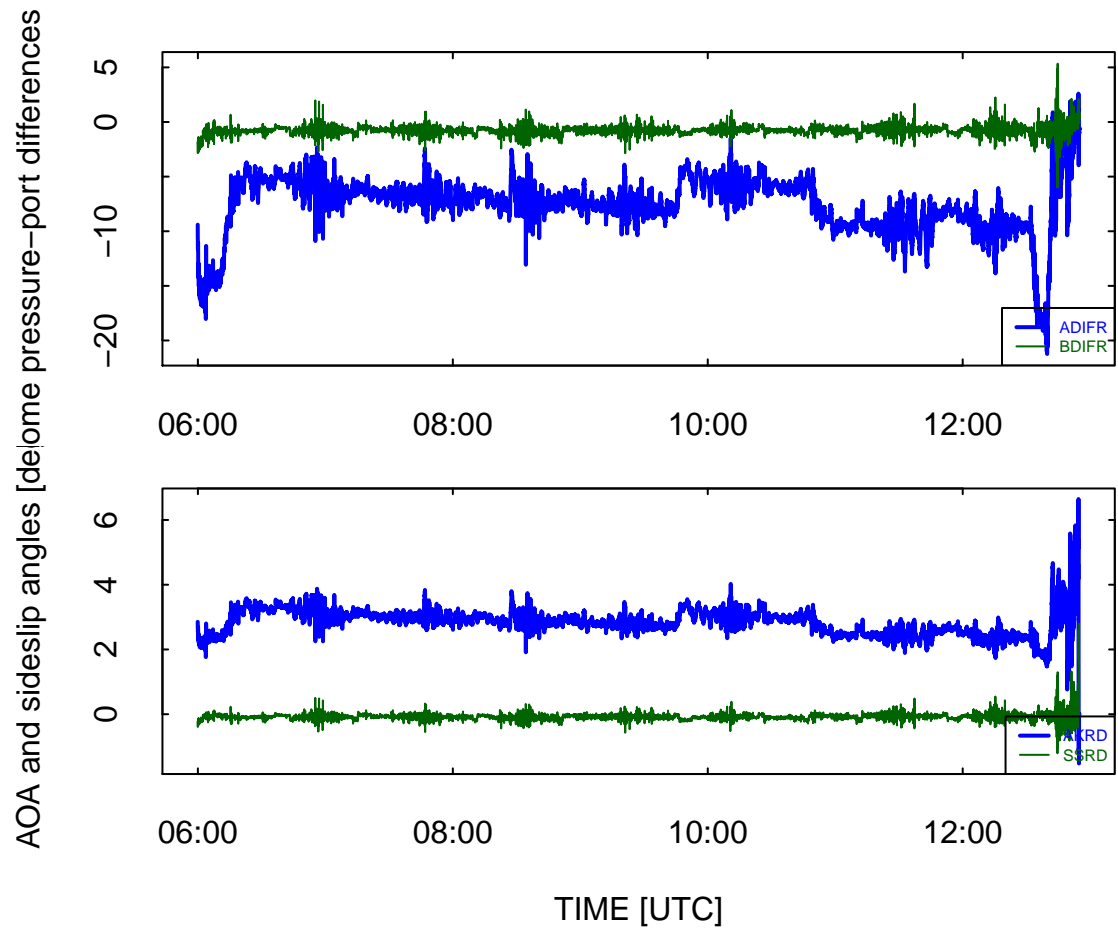


Figure 5: The pressure differences measured on the radome (ADIFR and BDIFR, respectively between the vertically separated ports and the horizontally separated ports) and the resulting airflow angles AKRD (angle of attack) and SSRD (sideslip angle). Data from DEEPWAVE flight 16.

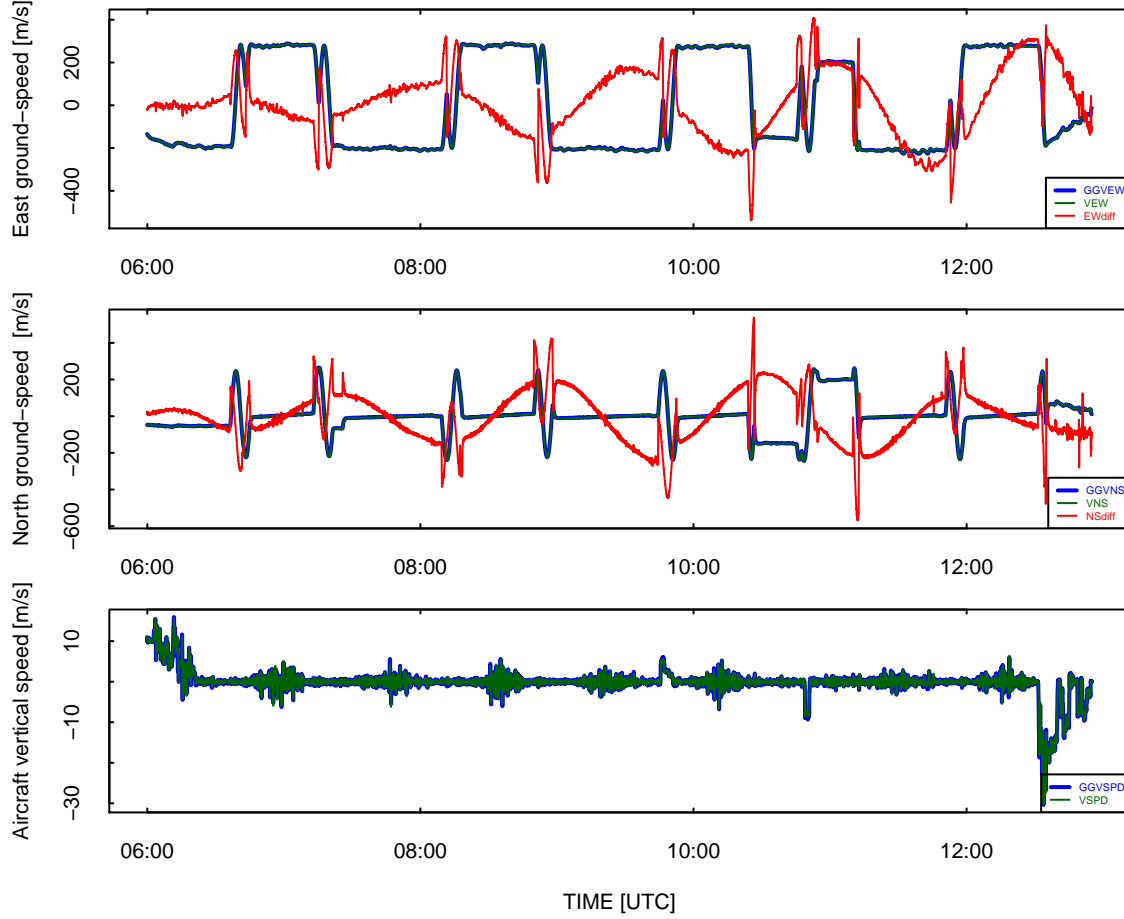


Figure 6: Top two panels: Ground-speed components as measured by the IRU and GPS, and (red lines) the difference between the two measurements multiplied by a factor of 100. Bottom panel: Aircraft vertical speed as measured by the IRU (with built-in damping to the pressure altitude) and by the GPS unit. Data from DEEPWAVE flight 16.

fraction of a degree, while there can be several-degree fluctuations in the angle-of-attack. The gradual decrease in angle-of-attack is a result of the change in fuel load on the aircraft, which requires a smaller angle-of-attack to keep the aircraft level as the weight becomes smaller.

The last set of components entering the measurement of wind consists of the measurements of the motion of the aircraft with respect to the Earth. These measurements must be combined with the measurement of relative wind to transform the measurements to an Earth-referenced measurement. Figure 6 shows the east and north components of the groundspeed as measured by the IRU and GPS. They are close enough to lie almost on top of each other in this plot, but the red lines show the difference magnified by a factor of 100. They clearly show the Schuler oscillation that results from an IRU error in pitch, having magnitude of about $1\text{--}2 \text{ m s}^{-1}$. This error is discussed in the next section, and Section XXX discusses how the IRU measurements (having good short-term response but long-term drift) and the GPS measurements (having long-term accuracy but inferior short-term response) are combined in the measurement of wind. In

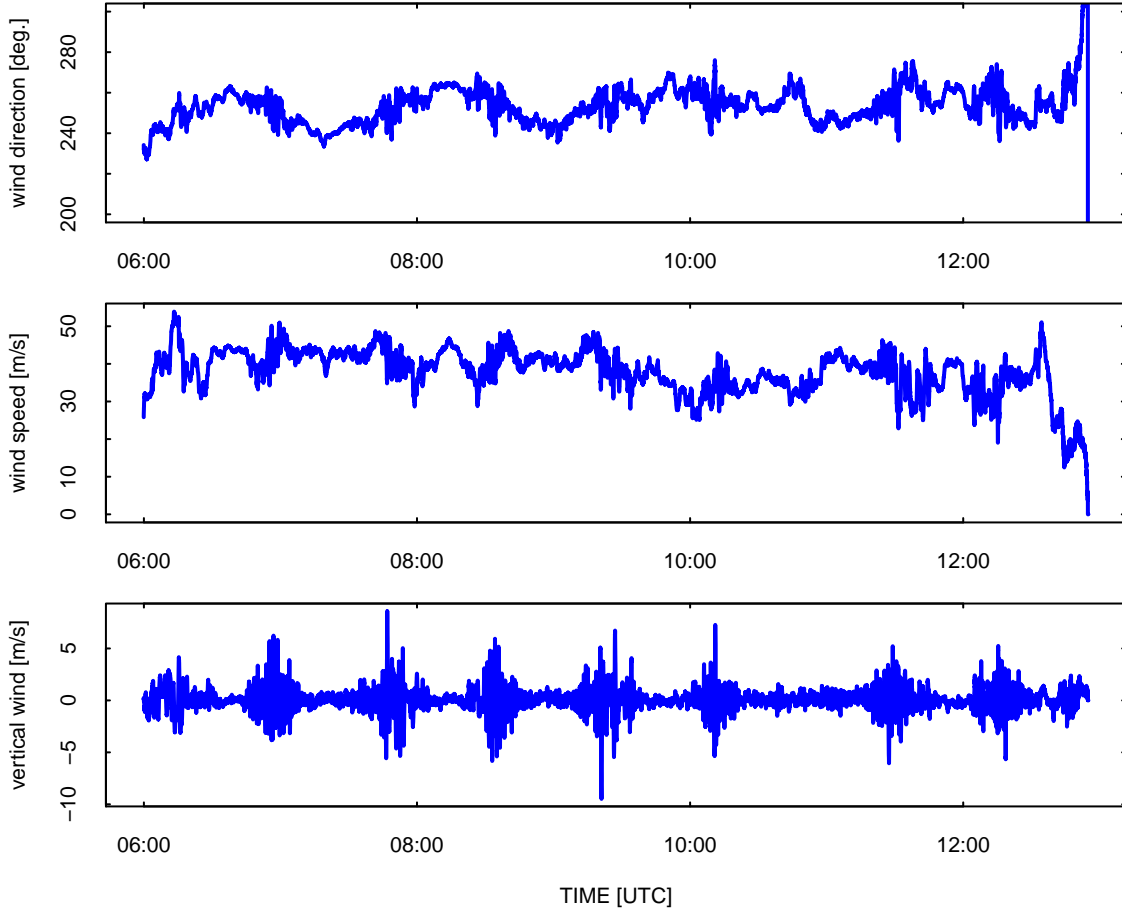


Figure 7: Wind measurements for DEEPWAVE research flight 16.

addition to the Schuler oscillation, additional perturbations associated with turns result from the mixing of pitch, roll, and heading errors when the aircraft is banked.

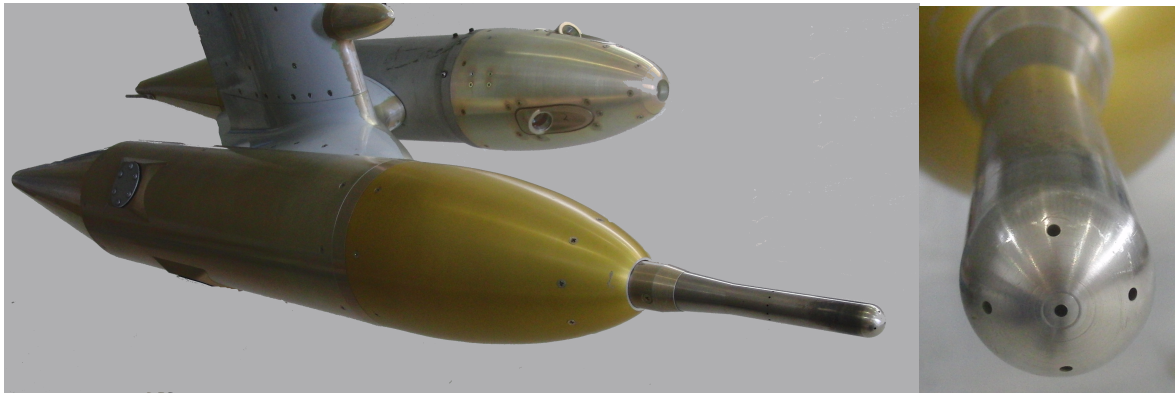
Finally, Fig. 7 shows the resulting wind measurements for this flight. These measurements will be discussed extensively in the remainder of this report, and the uncertainty associated with them will be estimated in the closing section.

2.3 The gust-pod system

2.3.1 Overview

The all-weather wind pod was developed by Allen Schanot and is available for mounting under the wing of the GV, where it was installed during the 2014 project DEEPWAVE. It was still regarded as experimental for this project, and this is the first full documentation of its characteristics. It will be called the gust-pod system here; another name used has been the all-weather wind pod, because the primary reason for its development was to provide a backup wind measurement for cases when the radome system was not available, including times when it was

blocked by ice or frozen water in the pressure lines. The gust pod fits into a standard “PMS-style” canister and uses a Rosemount 858 probe, but the location under the wing is one where there is substantial flow distortion in comparison to the free stream so an unconventional calibration is needed to use the measurements. The 858 probe is anti-iced by heaters and should be unaffected by icing or ice accumulation. Five ports are oriented forward, upward and downward 45°, and left and right 45° on the leading edge of the sensor, which has the shape of a hemisphere. There are also ports in a ring around the cylinder behind the hemisphere that provide a static source. The measurements are the pressure difference between the top and bottom ports (ADIF_GP), the pressure difference between the right and left ports (BDIF_GP), and the pressure difference between the forward port and the static ports (QC_GP). In addition, the pressure provided by the ring of static ports is recorded as PS_GP. The system incorporates a Systron-Donner C-MIGITSIII IRU, which is mounted in the pod to be able to measure vibrations and wing-flex motions that will affect the measurements of wind. This unit provides measurements of attitude angles, ground-speed components, and accelerations and uses a GPS signal in a Kalman-filter feedback loop to reduce errors in the measurements. The relevant specifications are listed in Table 2.



Photograph of the Gust Pod (bottom left) and the ports on the Rosemount 858 probe (right).

2.3.2 Attitude angles

The C-MIGITS INS/GPS unit provides measurements of the attitude angles, recorded as variables CROLL_GP, CPITCH_GP, and CTHDG_GP. The estimated standard uncertainty in measurement of pitch, 1 mrad (cf. Table 2), is supported by comparison to the cabin-mounted inertial systems; the standard deviation in the difference between the two systems was about $0.1^\circ \approx 1.7$ mrad for extensive multi-flight comparisons, while the expected difference for two systems each having standard uncertainties of 1 mrad would be 1.4 mrad. Some contribution would be expected from vibrations and wing flex that affect the gust pod, so these comparisons are good support for the approximate validity of the specifications. Some of the specifications (esp. for heading) degrade in the absence of turns or maneuvers that can be used by the Kalman filter to improve the measurements.

Measurement (VARIABLE)	Instrument	Range, Char- acteristics	Standard Uncertainty	Comments
velocity components CVNS_GP, CVEW_GP, CVSPD_GP	C-MIGITSIII	with GPS	0.1 m s ⁻¹	horizontal and vertical
pitch, roll (CPITCH_GP, CROLL_GP)	C-MIGITSIII	with GPS	1 mrad $\simeq 0.06^\circ$	
heading CTHDG_GP	C-MIGITSIII	with GPS	1.5 mrad $\simeq 0.09^\circ$	valid when in motion ^a
pressure differences,858 ports (ADIFR_GP, BDIFR_GP)	differential pressure transducer PPT0001DX2VB- 5021	range ± 1 PSI $\simeq \pm 68.95$ hPa	0.07 hPa 0.14 hPa max.	the first is “typ.”; same transducers as for radome
dynamic pressure (QC_GP)	differential pressure transducer PPT0005DX2VB- 5021 ^b	0–5 PSI $\simeq 0$ –345 hPa	0.34 hPa 0.68 hPa max.	“
ambient pressure (PS_GP)	absolute transducer Paroscientific 6000-15A-28	0–15 PSI $\simeq 0$ –1035 hPa	0.10 hPa	digital transducer

^aWithout occasional turns the heading error grows linearly at about 1–10°/hour^bcheck: 5021 or S021?

Table 2: Characteristics of measurements from the gust-pod that are used for the calculation of the wind. There is further discussion of each measurement in the text of Sect. 2.3.

2.3.3 Ambient or static pressure

Ambient pressure (variable PS_GP) is measured by a digital transducer with low uncertainty, as listed in Table 2. However, the Rosemount 858 probe is located under the wing in a location where there is significant airflow distortion, so these measurements often differ from the measurements from the static buttons on the fuselage by 10–20 hPa and significant corrections are needed if these measurements are to be used for pressure measurements. With the gust-pod, the use is as a reference for the differential measurement of dynamic pressure because the dynamic-pressure transducer is connected between the total-pressure port on the front of the 858 probe and the static ports. No calibration has been determined that would make this measurement useful as a measure of true ambient pressure, although that could be done by fitting to match the standard static pressure. In the absence of such a correction, PS_GP should not be considered an alternate measurement of ambient pressure. The use of this measurement to determine an alternate measure of true airspeed will be discussed in Section 4.3..

XXX

2.3.4 Dynamic pressure

The dynamic pressure QC_GP is measured by a differential pressure transducer, with characteristics shown in Table 2. The measurement is the pressure difference between the forward-pointing port on the Rosemouint 858 probe and the static ports on the side of that probe. Because the system is located under the wing in a region of disturbed airflow, the dynamic pressure requires unconventional correction to obtain the airspeed, as discussed in Sect. 4. This measurement is also used in the calculation of flow angles from the gust-pod pressure ports, as also discussed in that section.

2.3.5 Airflow angles

The difference between pressures at the top and bottom ports of the Rosemount 858 probe (ADIFR_GP) and the corresponding difference between right and left ports (BDIFR_GP) are also measured using differential transducers listed in Table 2. These are analog transducers that produce voltages representing the pressure differences, and those voltages are digitized and recorded by the aircraft data system.

2.3.6 Components of aircraft velocity relative to the Earth

A Systron-Donner C-MIGITSIII INS/GPS, mounted with the gust pod, provides digital representations of the ground-speed components CVEW_GP and CVNS_GP and the vertical speed CVSPD_GP. (cf. Table 2). The unit incorporates a GPS receiver and uses GPS information as input to a Kalman filter for adjustment of these measurements and others discussed in this section.

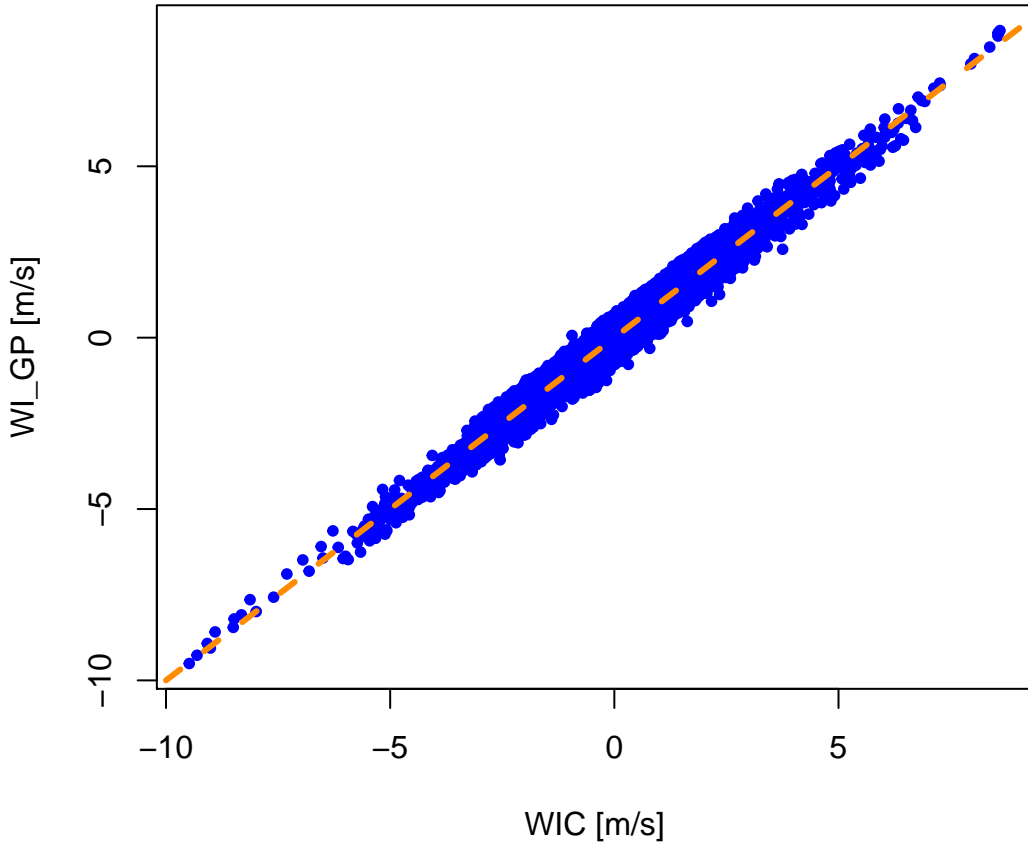


Figure 8: Comparison of vertical wind calculated from the gust pod (WI_GP) to the conventional measurement of vertical wind (WIC).

2.3.7 Temperature

Air temperature is measured in the same way as discussed for the radome system in Sect. 2.2.7, and the same variable (ATX) is used.

2.3.8 Examples of measurements

A preliminary calibration was in use for in-field processing during DEEPWAVE, but it did not perform very well. A new calibration is developed in Section 4. On the basis of that calibration, it appears that the gust pod provides a useful alternative to wind measurements based on the radome. Plots and average values are presented there to support the validity of this measurement.

The following are some plots that show the results of this processing, in this case from DEEPWAVE flight RF16 on 4 July 2014. Figure 8 shows a comparison of the vertical wind calculated from the gust pod (WI_GP) vs the conventional vertical wind (WIC). The standard deviation

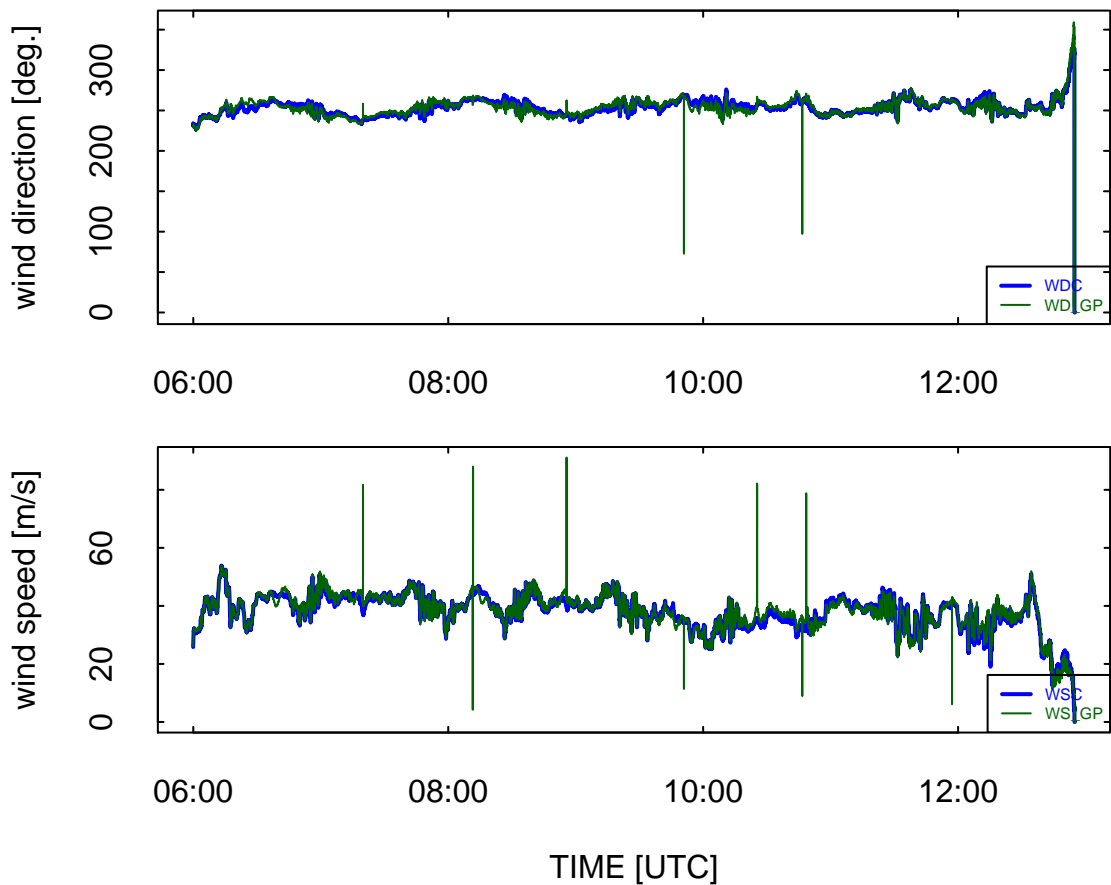


Figure 9: Comparison of vertical wind direction (top panel) and vertical wind speed (bottom panel) as determined from the gust pod and from the conventional radome-based system.

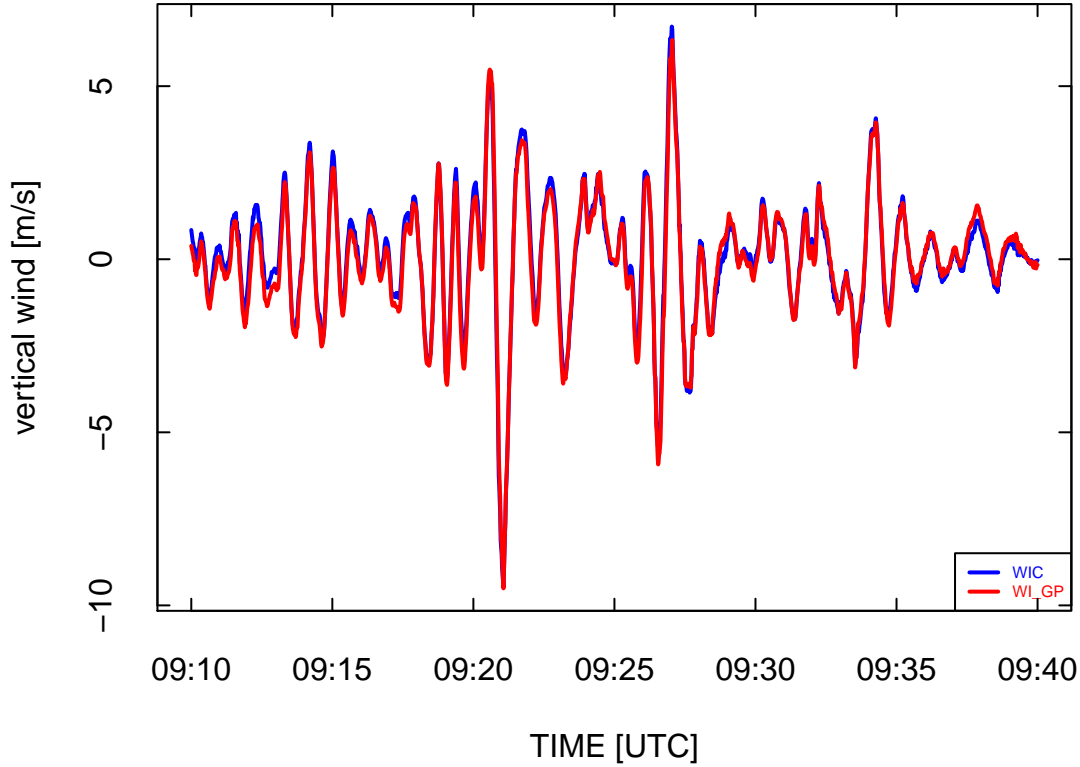


Figure 10: A 15-min segment from flight 16 of the DEEPWAVE project, showing the good agreement of the vertical wind measurements from the gust pod (WI_GP) and from the conventional wind-sensing system on the GV (WIC). The dashed orange line is a 1:1 reference line, and each blue dot represents a 1-s pair of corresponding measurements.

between the two measurements is about 0.3 m/s. This is a good illustration because this is a flight with large-amplitude waves and some of the largest vertical-wind measurements in the DEEPWAVE project, so the consistency of these measurements even to extremes in this plot indicates that the measurements from the gust pod are useful even for these large-amplitude measurements. Figure 9 shows the corresponding horizontal-wind measurements, and also shows good agreement between the gust pod and the conventional wind-sensing system. In this case, so spikes are evident in the measurements from the gust pod. These are the result of a problem with the C-MIGITS measurement of heading, which exhibits noisy fluctuations as it moves through 180°. These are a problem for the horizontal wind measurements, esp. the east component. They can be removed by spike-removal routines but are present in first-pass data files. Almost all appear in turns where the measurements from the gust pod should not be used because errors arising from misalignment of the gust-pod IRU with respect to the aircraft longitudinal axis causes mixing of the attitude angles in turns.

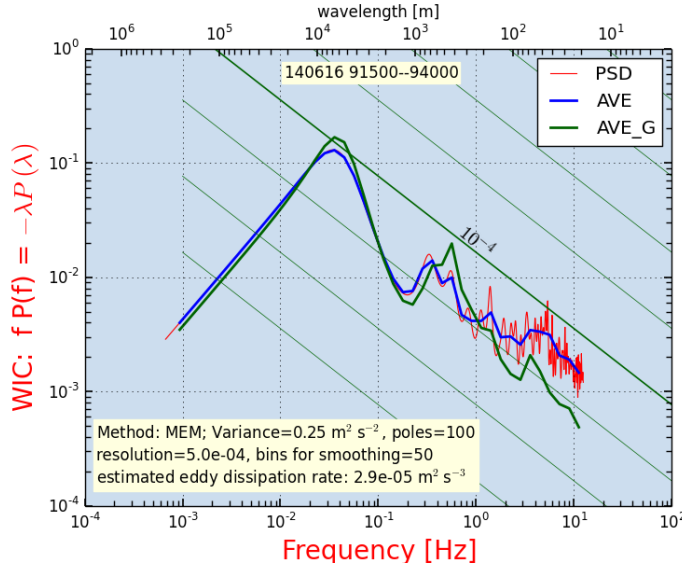


Figure 11: variance spectra for WIC (red line, and also shown smoothed as the blue line), compared to the spectrum for WIG from the gust pod (green line). Data from flight RF05, 9:15:00–9:40:00.

A small segment of flight from a period with large-amplitude waves is shown in Fig. 10. The two measurements match quite well in regard to the structure of these waves and the amplitudes of the fluctuations. The measurements of horizontal wind speed are in similar agreement, but the wind direction for this period shows an offset for the gust pod measurement relative to the conventional measurement, varying from about 5° near the start of this period to about 1° near the end. This is a result of an apparent error in heading from the C-MIGITS IRU, a common feature to see near the start of flights but one that usually was made smaller during flight by the action of the GPS updating via Kalman filter in that unit.

The result of this error in wind direction and the problems with measured heading for flight exactly southbound complicate the use of the measurements of horizontal wind from the gust pod and make them of lesser quality than the standard measurements. Fortunately, in this and most projects, the horizontal-wind measurements are available from the radome-based system on all flights and are usually not compromised even when there is loss of the measurement of angle-of-attack from plugging of the lines in the radome, because the side-mounted ports for the measurement of sideslip seldom are plugged.

Figure 11 shows the high-rate variance spectra from the two systems. There is a significant difference at frequencies above about 3 Hz, with the gust-pod distribution dropping faster but the standard wind WIC showing more variance. The high frequency spectrum from the gust pod may be more realistic; it is unusual to see high variance at these frequencies without a related generating source. These spectra were also studied for coherence, which was above 0.9 for frequencies less than 1 Hz but then fell to around 0.2 at 10 Hz. This is an indication that the two measurements are different in important ways at high frequency. This would not be the case if they were responding with different amplitudes; the signals must really be mostly incoherent at the highest frequency. The separation wing-to-fuselage is about 7 m lateral and 13

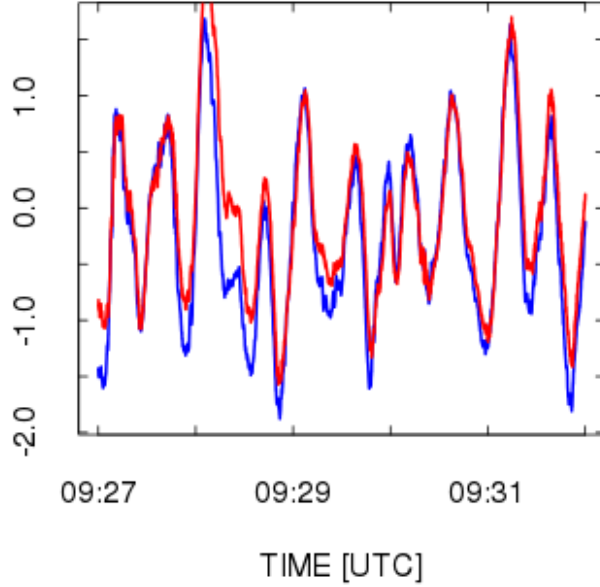


Figure 12: Comparison of WIG (red line) and WIC (blue line) after shifting WIG 1/25 s earlier to compensate for the longitudinal displacement of the sensor.

m longitudinal, so that doesn't seem enough to cause the low high-frequency coherence. The phase changes from in-phase at frequencies less than 1 Hz to 180° out-of-phase at 9 Hz, with WIG lagging, so this is consistent with the longitudinal offset. Shifting WIG relative to WIC also gave maximum coherence if WIG were shifted forward 1/25 s.

2.3.9 Mixing of Attitude Angles for the Gust Pod

The gust pod does not yet perform well in turns. The reason is that the orientation of the gust-pod IRU is not perfectly along the longitudinal axis of the aircraft, and as a result any roll of the aircraft introduces complex combinations of roll, heading, and pitch into the gust-pod IRU. It should be possible to remove these to some extent, but a procedure for correction of the angles in turns has not been developed or implemented.

The attitude angles (pitch, roll, heading) as measured by the gust-pod IRU are defined relative to the orientation of the inertial unit in the gust pod, which is not aligned with the longitudinal axis of the aircraft. The canisters on the GV are oriented with axis pointing inward and downward relative to the aircraft longitudinal axis, in order to align with normal flow at the pods. This is desirable for hydrometeor sampling and minimum drag, but it complicates the calculation of wind because roll introduced in turns, primarily a rotation about the aircraft longitudinal axis, will appear as a combination of attitude-angle changes in the gust pod. Errors arising from the initial alignment at the start of flights will also cause problems with the measured attitude

angles, and it is likely that these will be more significant near the start of flights because the build-in Kalman filter will use GPS measurements to correct such errors in the course of the flight.

This problem with the reference frame for attitude angles has two consequences:

1. Measurements from the gust pod in turns have large errors in comparison to the errors in level flight. The measurements from the gust pod should probably be flagged as of poor quality whenever the roll exceeds some threshold like perhaps $\pm 5^\circ$. The measurements usually look reasonable in turns despite this worry, but the largest errors occur there.
2. There may be an offset introduced by the mixing of sideslip and angle-of-attack, arising from the difference in roll angle, and this will affect the reference or average value of the measured vertical wind. Some flights (e.g., DEEPWAVE flight 18) have a significant offset in vertical wind from the gust pod at the start of the flight that is related to offsets in heading and roll, gradually corrected in the course of the flight via the C-MIGITS Kalman filter.

Because the weight of the aircraft decreases during the flight, so does the angle-of-attack. Because the wing flexes, the measured sideslip at the gust pod also varies with weight of the aircraft. This change in sideslip causes an offset in the mean lateral component of the wind.

These effects suggest that the vertical wind measured by the gust pod may have an offset in some cases, particularly at the start of flights, and the sideslip can also have an offset that will contribute to the lateral component of the measured wind. These are weaknesses in the measurements from the gust pod that, at this stage, do not appear easily corrected. A future study implementing Schuler tuning in a post-processing step and correcting for the entwined-angle effects may be able to reduce these weaknesses, but that will require an extensive investigation. XXX

2.4 The laser air-motion sensor (LAMS)

The LAMS did not function properly in DEEPWAVE. It will not be discussed in detail in this report because it is still under development. The characteristics and associated uncertainties in measured wind are discussed by Spuler et al. [2011] and Cooper et al. [2014]. The system consists of one or several fiber-based laser beams focused ahead of the aircraft and a collection system to detect the Doppler shift in light backscattered from aerosols. The transmitter optical components are mounted in an underwing pod, similar to that used for the gust pod, and like the gust pod the system incorporates a compact C-MIGITS inertial reference unit to measure the attitude angles and ground speed of the pod. Early measurements from this system have been used to determine corrections to the pressure measurements, and those serve an important role in reducing uncertainty in the wind measurements, as described in Cooper et al. [2014] and later in this report.

3 Schuler correction for pitch

3.1 Basis for the correction

Before discussing additional aspects of the measurement system like determination of sensitivity coefficients for the radome, it is necessary to explain and document a correction that will be used in that determination and in subsequent studies. The normal primary weakness in measurement of vertical wind is the measurement of pitch, which is provided only by inertial reference systems and therefore has the uncertainty and fluctuations associated with those systems. An inertial system aligns during initialization to detect the local vertical direction and then calculates the new vertical direction as the aircraft moves (changing the local vertical direction) and accelerates (which can cause gyros to precess). Any mis-alignment present at initialization persists but also can oscillate and can cause errors in roll and pitch to mix as the aircraft changes flight direction. The standard error associated with this measurement is 0.05° for flight duration of a few hours, and the error often increases during the flight as heading errors and accelerometer biases affect the results.

Following the work of Schuler ([Schuler \[1923\]](#)), coupling among some of these error sources leads to limits on the growth of errors and simultaneous oscillations in some of the measurement errors. In particular, an error in pitch leads to an error in horizontal acceleration, and integration of that error in horizontal acceleration leads to a position error that compensates for the original error in pitch. However, when the error in pitch is reduced to zero, errors in position and velocity have been accumulated and those lead to growth of the error in pitch in the direction opposite to the original error. The result is a Schuler oscillation having a period of $T_{Sch} = (R_e/g)^{0.5}/(2\pi) \approx 5064\text{s}$ or 84.4 min , where R_e is the radius of the Earth and g the acceleration of gravity. The existence of this coupling allows estimation of the pitch error if the error in horizontal acceleration is known. That is the case in DEEPWAVE because high-quality measurements of velocity are available from GPS and those measurements can be compared to the uncorrected measurements from the inertial systems to measure the error in velocity and, from its derivative, the error in acceleration. The specified uncertainty for the IRU, 0.05° , contributes an uncertainty in measured vertical wind of about 0.2 m/s , and it is shown later that this is the dominant contribution to uncertainty in that measurement, so improving on this can lead to significant reduction in the uncertainty associated with measurement of vertical wind.

3.2 Simple illustration of Schuler oscillation

Although the following is standard material, it is presented here to make the discussion of the Schuler oscillation self-contained and for tutorial purposes. Those familiar with the Schuler oscillation should skip this section.

Consider first the case of steady flight to the north. If, at some starting point at rest, there is a pitch error $\delta\theta$, that will cause gravity to be resolved into a NS component, as shown in this diagram where a pitch error of $\delta\theta$ produces an erroneous northward acceleration of $g \sin(\delta\theta) \simeq g\delta\theta$:

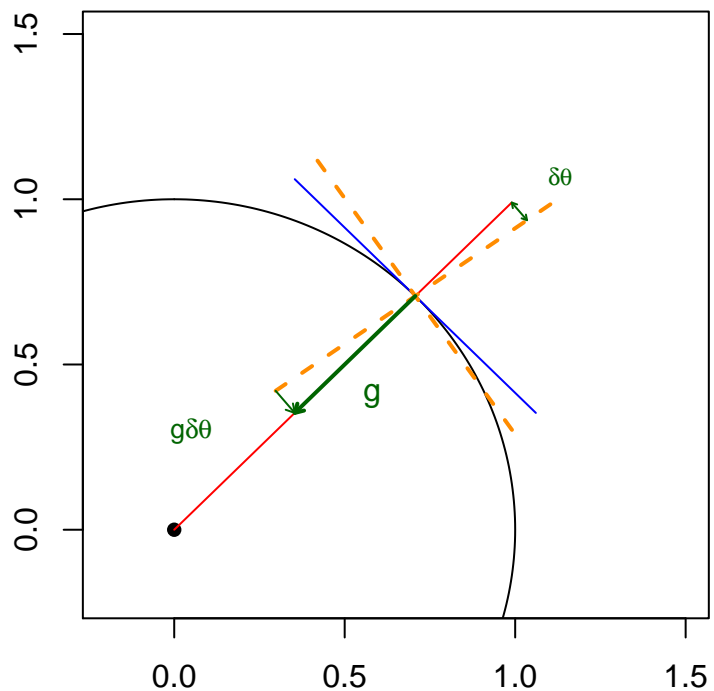


Figure 13: Illustration of how a pitch error of magnitude $\delta\Theta$ leads to a false measurement of horizontal acceleration of magnitude $g\delta\Theta$. The blue line represents the true level plane tangent to the surface of the Earth and g the magnitude and direction of the gravitational acceleration.

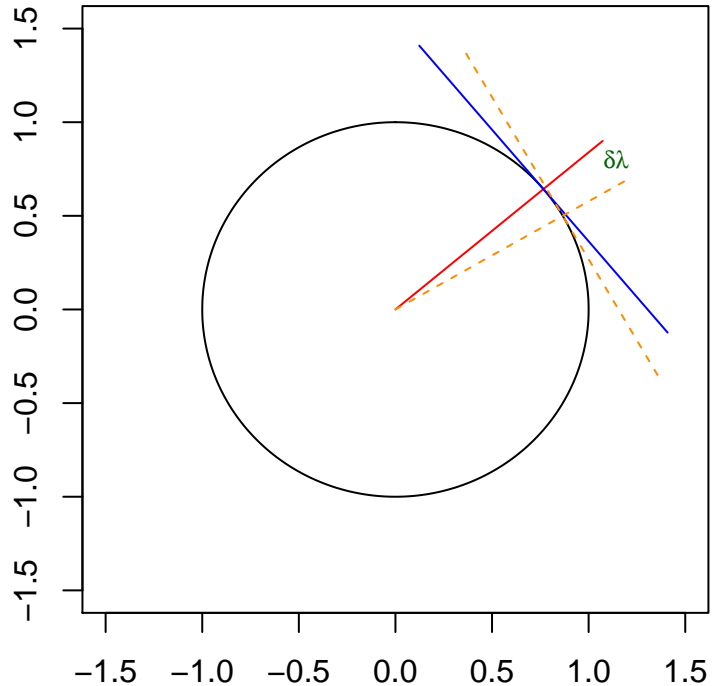


Figure 14: Illustration of how a position error, denoted here as an error in latitude $\delta\lambda$, leads to an error in the direction of the vertical axis and so to a false horizontal acceleration.

The result is that this erroneous acceleration produces a false northward velocity and, integrated, a northward error in position. However, the error then causes the integrated position to become too far north, where the calculated direction toward the center of the earth becomes biased in the opposite direction, and at some point the calculated offset from being too far north equals the pitch bias, as shown in the next figure:

However, at the point where the error in latitude cancels the error in pitch, there is an accumulated error in velocity, so the integrated solution for position overshoots the equilibrium position by an amount such that the error in pitch becomes the negative of the original error, at which point the integrated velocity is zero but the new error in pitch now causes a reversal of the position error. The result is that the errors in pitch, velocity and position all oscillate with a period equal to the Schuler period, $T_s \simeq 5064$ s, determined from $T = (R_e/g)^{0.5}/(2\pi)$.

Here are the equations predicting how this oscillation will occur:

$$v_n = \frac{dx_n}{dt} = R_e \frac{d\lambda}{dt} \quad (6)$$

$$\frac{d^2 x_n}{dt^2} = a_n \quad (7)$$

where x_n is the north coordinate of the position and a_n is the northward acceleration. However, if $a_n = a_n^* + \delta a_n$ where a_n^* is the true northward acceleration of the aircraft and δa_n is the erroneous acceleration that results from pitch and displacement errors, then

$$\delta a_n = g(\delta\lambda - \delta\theta) \quad (8)$$

with λ the latitude, $\delta\lambda = \delta x_n / R_e$ the error in latitude, and $\delta\theta$ the error in pitch. Then

$$\frac{d(\delta v_n)}{dt} = -g\delta\theta \quad (9)$$

$$\frac{d(\delta\theta)}{dt} = \frac{\delta v_n}{R_e} = -\frac{1}{g} \frac{d^2(\delta v_n)}{dt^2} \quad (10)$$

which has the solution:

$$\delta v_n = V_n \cos(\omega t + \zeta_n) \quad (11)$$

where $\omega = \sqrt{g/R_e} \simeq 0.00124$ is the Schuler angular velocity. The error in the north component of the velocity therefore oscillates with the Schuler period and a phase ζ_n . Integrating in time gives

$$\delta x_n = \int \delta v_n dt = \frac{V_n}{\omega} \sin(\omega t + \zeta_n) \quad (12)$$

The key to developing a correction to the pitch angle is that both δx_n and δv_n are observable because reference measurements are available from GPS. For example,

$$\begin{aligned} \delta x_n &= R_e (\text{LAT} - \text{GGLAT}) \\ \delta v_n &= \text{VNS} - \text{GGVNS} \end{aligned} \quad (13)$$

These observations can determine A_n and ζ_n in (11). From these, the error in pitch can be found from (9):

$$\delta\theta = -\frac{1}{g} \frac{d(V_n \cos(\omega t + \zeta_n))}{dt} = \frac{V_n \omega}{g} \sin(\omega t + \zeta_n) \quad (14)$$

Analogous equations lead to a similar coupling between the roll angle and the east component of the ground velocity:

$$\delta\phi = \frac{V_e \omega}{g} \sin(\omega t + \zeta_e) \quad (15)$$

where ϕ is the roll angle and V_e and ζ_e are determined from fits to the observed error $\delta v_e = \text{VEW} - \text{GGVEW}$.

Thus the observed errors in the components of the aircraft groundspeed can be used to find corrections to be applied to the measurements of pitch and roll.

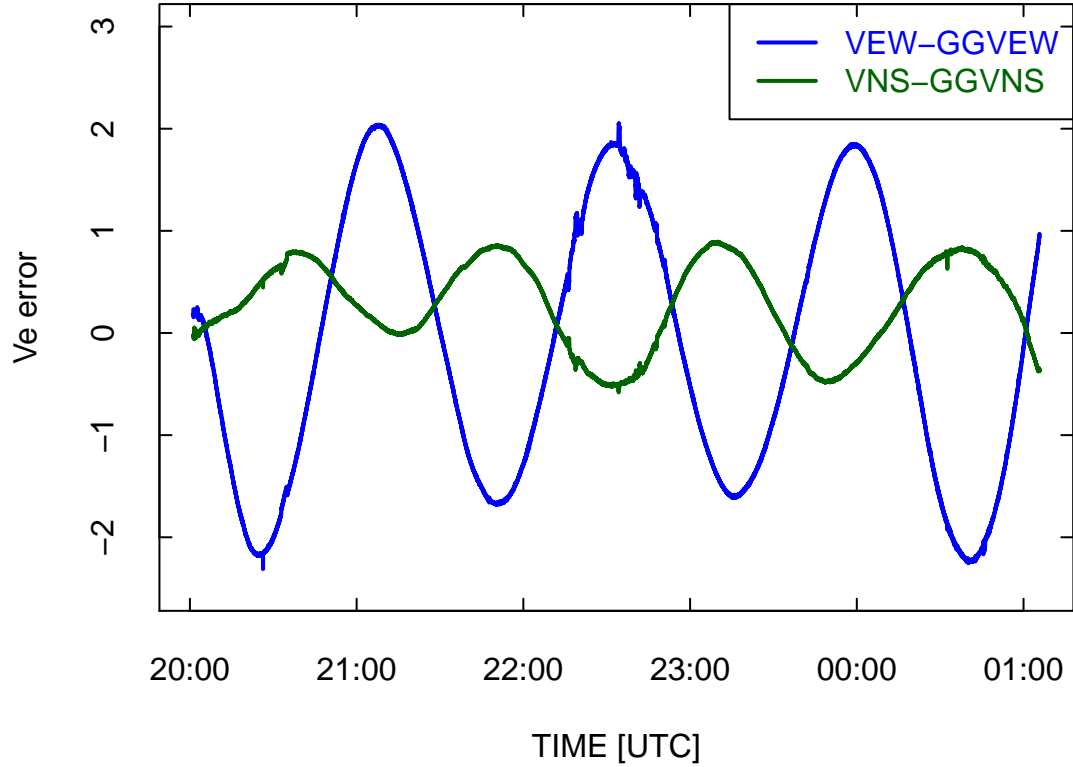


Figure 15: Errors in the NS and EW components of groundspeed as determined by comparison to GPS, for DEEPWAVE flight ff02, a ferry flight starting on 1 June 2014 and traveling from Hawaii to Pago-Pago.

3.3 Illustrative example

An example from the second ferry flight of DEEPWAVE is shown in Fig. 15. The heading for most of this flight is close to southbound and steady, so to a reasonable approximation the errors in pitch and heading will be given by the respective derivatives in the error terms δv_n and δv_e .

The errors can be determined directly from the time-derivatives of the error terms in (9) and the analogous equation for roll, restated as:

$$\delta\theta = -\frac{1}{g} \frac{d(\delta v_n)}{dt} \quad (16)$$

$$\delta\phi = -\frac{1}{g} \frac{d(\delta v_e)}{dt} \quad (17)$$

Therefore, rather than fitting variations like that shown in Fig. 15 to sine or cosine functions, it

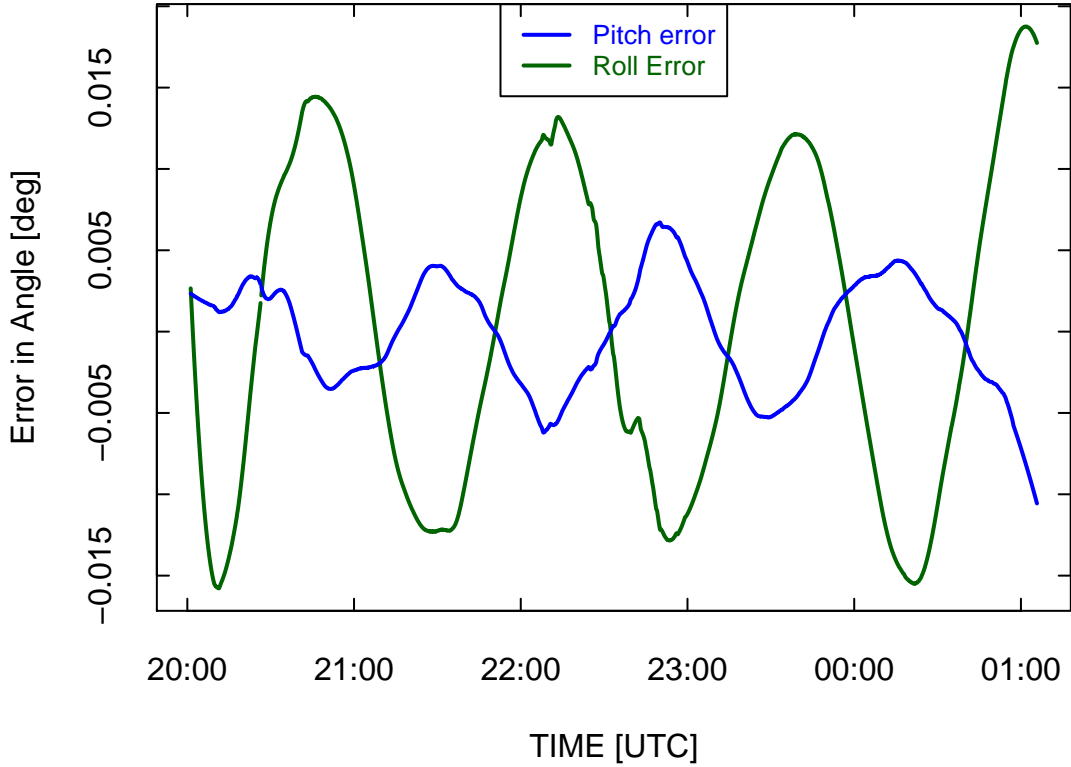


Figure 16: Deduced error in pitch and roll angles for DEEPWAVE ferry flight ff02.

is possible to obtain an estimate of the time derivatives of the velocity-error terms over some shorter interval and then use that derivative in (16) or (17) to find the errors in pitch and roll. It is important to note, though, that this gives errors in the local reference frame with axes eastward, northward, and upward, here called the l-frame, and these errors will then need to be transformed to the aircraft reference frame to get errors in the measured quantities. The choice made here is to estimate the derivatives using Savitzky-Golay polynomials, as shown in Fig. ?? . Savitzky-Golay polynomials were chosen because they are computationally efficient, don't introduce a time shift, and can provide derivatives directly. A rather long averaging period of 1009 s, or about 1/5 of a Schuler oscillation, was used to reduce noise in the result, and interpolation filled some gaps in the measurements.

The result is that the pitch error is limited to about 0.01° in magnitude for most of this flight, except for the final descent, and the roll error is limited to less than about 0.015° for the same period. This is evidence for low uncertainty in the pitch measurement for this flight, well below the specification of 0.05° . Section 3.5 contains further discussion of the errors from the research flights, where the estimated errors can be larger.

3.4 Transformation of attitude angles

In a reference frame called the *l*-frame or ENU frame, where the coordinate axes are local-east, local-north, and upward, the preceding section showed that the pitch and roll errors are related, vis (16) and (17), to the time-derivatives of the errors in horizontal velocity. Pitch and roll as used in these equations will be the respective errors in platform alignment² in the north-south and east-west directions, so these angles must be transformed to account for the orientation of the aircraft when it is not flying straight-and-level to the north. Coordinates in the body or *b*-frame of the aircraft are obtained from those in the ENU or *l*-frame by applying three rotations to account for the heading, pitch, and roll of the *b*-frame. This transformation leads to pitch errors in the body frame of the aircraft (where measured pitch and roll are measured and where the pitch measurement affects the calculated vertical wind) that are mixtures of pitch and roll errors in the *l*-frame, with the mixture dependent primarily on the heading. A positive pitch error for northbound level flight will be a negative pitch error for southbound level flight, and for eastbound flight an *l*-frame roll error becomes a *b*-frame pitch error while an *l*-frame pitch error become a negative *b*-frame roll error.

Consider a unit vector representing the orientation errors in pitch and roll in the *l*-frame, with components $\{\sin \delta\phi, \sin \delta\theta, \sqrt{1 - \sin^2 \delta\phi - \sin^2 \delta\theta}\}$ or, because the errors are always small, approximately $\{\delta\phi, \delta\theta, 1\}$. The three-angle transformation of this vector from the *l*-frame to the *b*-frame is then represented by the following matrices, with $\{\phi, \theta, \psi\}$ representing $\{\text{roll}, \text{pitch}, \text{heading}\}$:

$$R_l^b = \begin{bmatrix} \cos \psi \cos \phi + \sin \psi \sin \phi \sin \theta & -\sin \psi \cos \phi + \cos \psi \sin \phi \sin \theta & -\cos \theta \sin \phi \\ \sin \psi \cos \theta & \cos \psi \cos \theta & \sin \theta \\ \cos \psi \sin \phi - \sin \psi \sin \theta \cos \phi & -\sin \psi \sin \phi - \cos \psi \sin \theta \sin \phi & \cos \theta \cos \phi \end{bmatrix} \quad (18)$$

$$\mathbf{b}^{(b)} = R_l^b \mathbf{b}^{(l)} \approx \begin{bmatrix} \cos \psi & -\sin \psi & 0 \\ \sin \psi & \cos \psi & 0 \\ 0 & 0 & 1 \end{bmatrix} \begin{bmatrix} \delta\phi \\ \delta\theta \\ 1 \end{bmatrix} = \begin{bmatrix} \cos \psi \delta\phi - \sin \psi \delta\theta \\ \sin \psi \delta\phi + \cos \psi \delta\theta \\ 1 \end{bmatrix} \quad (19)$$

which leads to $\delta\theta^{(b)}$ and $\delta\phi^{(b)}$, the pitch and roll errors in the *b*-frame:

$$\begin{aligned} \delta\theta^{(b)} &\simeq \sin \psi \delta\phi + \cos \psi \delta\theta \\ \delta\phi^{(b)} &\approx \cos \psi \delta\phi - \sin \psi \delta\theta \end{aligned} \quad (20)$$

In turns, the roll angle is no longer negligible, so in general the full transformation should be used and the pitch error should be found from the results of (19). Because the pitch and roll

²The inertial system used is a strap-down system, so there is no actual motion of the “platform”. Instead, from measured rotations and accelerations, the system calculates the expected orientation if there were a true stabilized platform. The errors referenced here are those relative to that calculated platform orientation.

angles are applied by this full transformation, the resulting errors are obtained by subtracting the measured pitch and roll from the transformed result; e.g.,

$$\delta\theta^{(b)} = \arctan \frac{b_2^{(b)}}{b_3^{(b)}} - \theta \quad (21)$$

This pitch error should then be subtracted from the measured pitch to obtain a corrected value of the pitch for use in the calculation of vertical wind.

3.5 Application to research flights

The research flights have frequent changes in heading, with mixing of the roll and pitch errors but also accelerations that affect those errors and introduction of new errors from heading errors. The corrections to pitch therefore appear much less systematic than was the case for the ferry flight. An example, DEEPWAVE flight 1, is presented here. Figure 17 shows the measured errors in ground-speed components, and Fig. 18 shows the deduced pitch and roll errors. There are instances where the pitch error abruptly reverses sign; those are cases where the flight direction changes by about 180 deg. During turns, the full transformation leads to a result significantly different from the small-angle-approximation result, as shown by the orange line in Fig. 18, but when not turning the full-transformation results replicate the small-angle-approximation results (blue line), as indicated by the orange dashed line overlapping the blue line. The proposed solution is to use the full transformation for processing a corrected pitch variable, to be named “PITCHC”, to be used for calculation of the vertical wind. In straight-and-level flight, the needed corrections are about $\pm 0.03^\circ$ at some times, and this error can lead (for true airspeed of 220 m/s) to an error in vertical wind of about ± 0.1 m/s. Correction for this error thus should lead to a significant reduction in the uncertainty associated with the measured vertical wind.

```
## [1] 0.01912708
```

3.6 Tests of the correction

Two tests were used to test if these pitch corrections made any significant difference in the measurements of vertical wind. First, wind measurements made before and after level course reversal were compared to see if correcting the pitch reduces the difference in measurements on the two legs before and after turns. Reduction would be expected because if there is a pitch error it would reverse sign between the two legs, increasing their absolute difference. Second, flight-average and project-average vertical wind measurements were compiled without and with the pitch correction.

The following is a tabulation of five instances where the flight track reversed course and remained at the same altitude. A number of other candidates were excluded because conditions were too variable along the legs to produce a small-uncertainty estimate of the vertical wind.

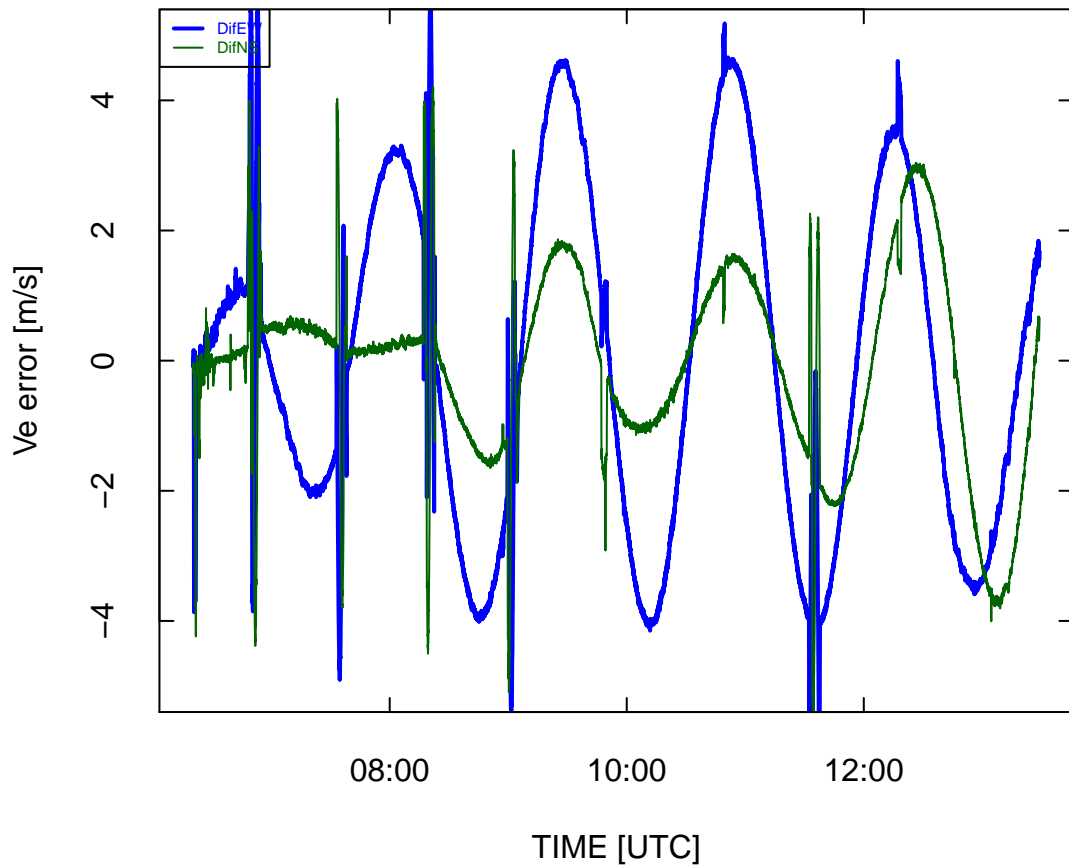


Figure 17: Measured errors in ground-speed components for DEEPWAVE flight 1. VEW and VNS are the east and north components of the ground speed measured by the inertial system, and GGVEW and GGVNS are the corresponding components measured independently by the GPS system.

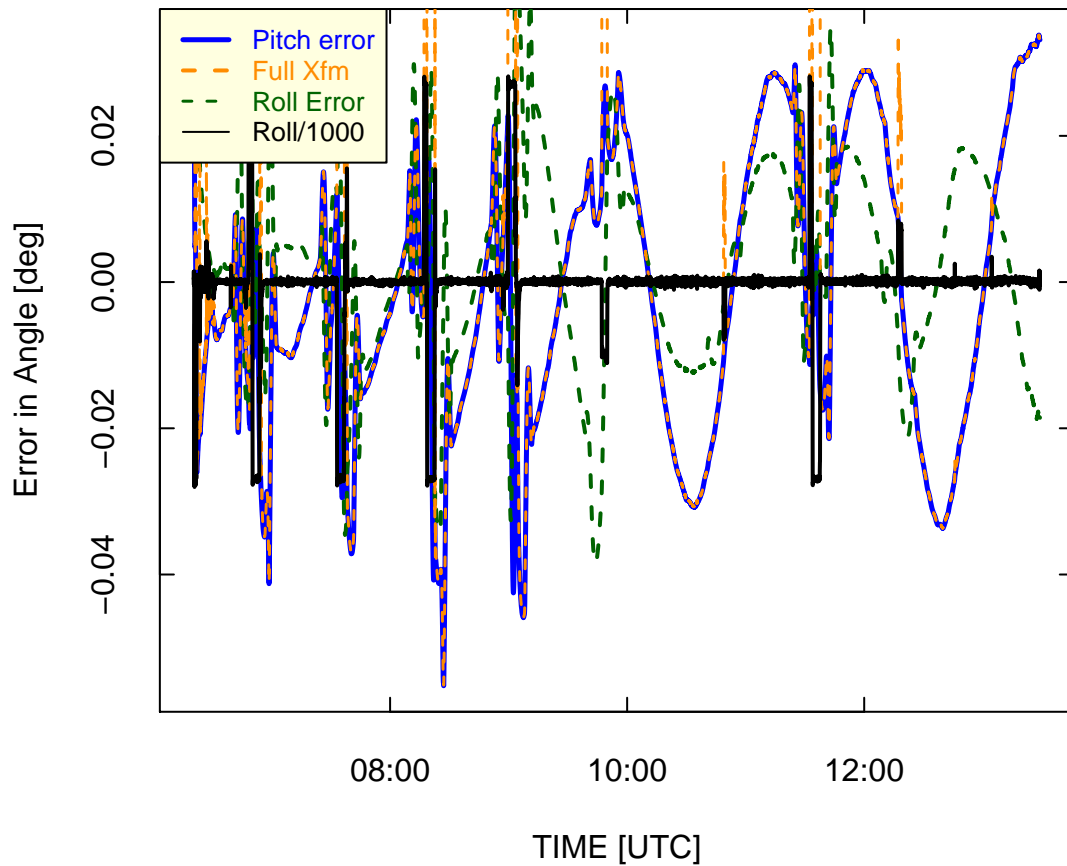


Figure 18: Errors in pitch and roll determined from the measured errors in ground-speed components, after transformation to the reference frame that is the body frame of the aircraft. The orange line labeled 'Full Xfm' uses (19) and (21), while the blue line uses the approximate result (20). The limits ± 0.03 correspond to roll angle of $\pm 30^\circ$ after division by 1000, so the regions with vertical black lines are ones with significant roll.

In each case, flight periods of about 5 min (sometimes adjusted in times of strong wind to give similar-length segments flown upwind and downwind) are listed before and after the turn, but excluding the turn, to represent approximately overlapping flight segments where it would be expected that the vertical wind would be the same.

Flight	Times before turn	Times after turn
1	81000–81600	82400–83000
2	122500–123000	123700–124300
19	83930–84430	85130–85630
21	85100–85500	90300–90730
21	95630–100130	100800–101300

The difference between average vertical wind measurements for each pair of legs was calculated before and after applying the pitch-correction algorithm developed in this section. The average absolute value of the difference before correction was smaller than 0.1 m/s, so the wind measurements were already in very good agreement for these pairs of legs and not much improvement could be expected. However, application of the pitch-correction algorithm did reduce this average to less than half the uncorrected value, as shown in Fig. 19.

```
## [1] "mean uncorrected 0.091880, corrected 0.033939"
```

The measurements were in good agreement without any pitch correction, with an average absolute value of the difference between legs of 0.09 m s^{-1} . The pitch correction kept the averages quite small and did appear to produce some improvement, reducing the mean value to 0.03 m s^{-1} . More significant than this small reduction is that the values were so small even before correction. This is a good indicator of the accuracy of the pitch measurement even without correction. A course-reversal difference of 0.1 m s^{-1} would result from a pitch error of less than 0.015° , so this suggests that the inertial system is performing significantly better than its specified uncertainty (0.05° would require). After correction, the mean difference suggests an error of less than 0.005° for the corrected values.

Table 3 lists the mean vertical wind with and without pitch correction for each of the DEEP-WAVE flights. For each flight, all measurements above 25,000 ft with true airspeed above 130 m/s and roll between -5 and 5° were included to emphasize normal research conditions. Any missing measurements were also excluded from the averages, and measurements from flights 6, 7, and 15 are not included because the first two were cases where the conventional vertical-wind measuring system malfunctioned and flight 15 was a flight devoted to calibration with little upper-level flight and frequent turns including circles.

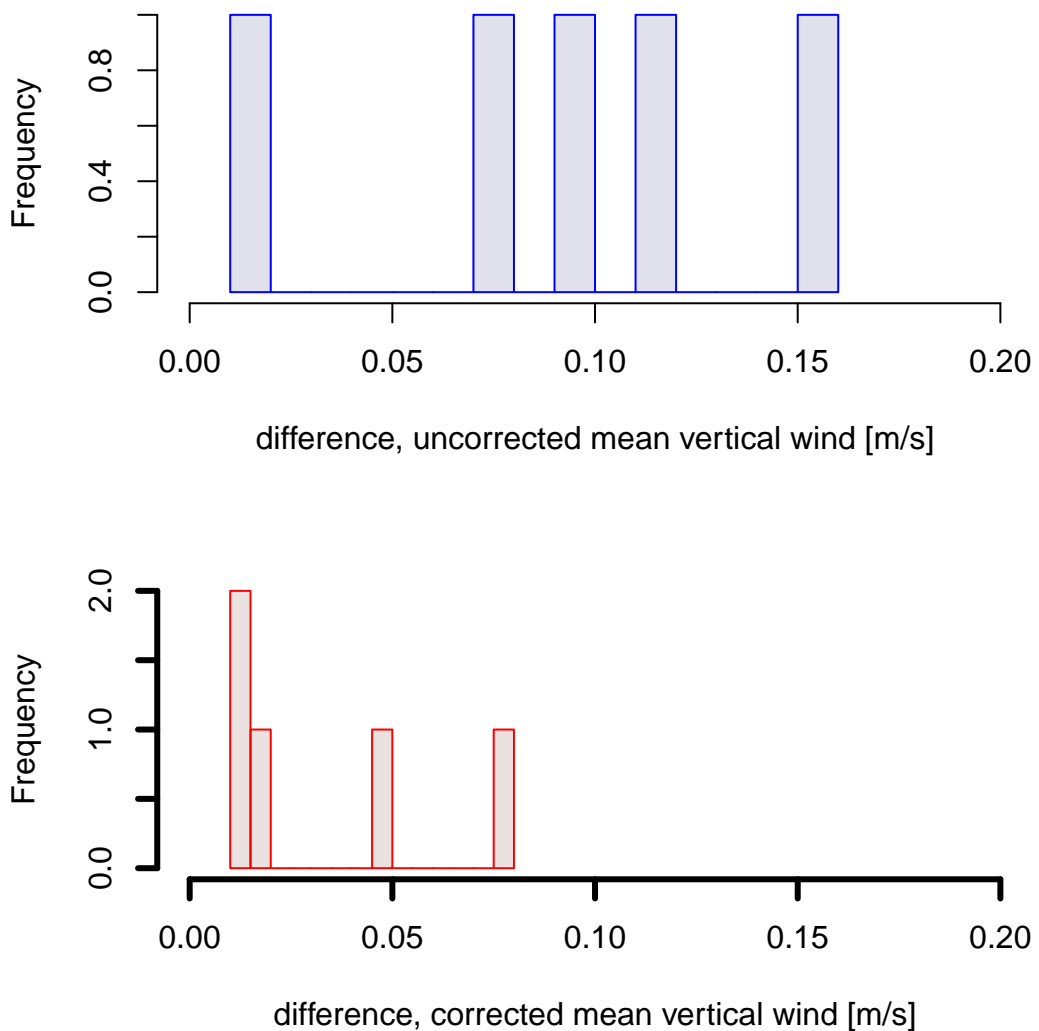


Figure 19: Absolute difference in vertical wind for flight segments before and after level course-reversal maneuvers. The top panel shows the uncorrected measurements and the bottom panel shows the result of applying the pitch correction developed in this section.

flight	mean WIC	mean corrected WIC
1	-0.01	-0.02
2	0.03	0.02
3	-0.07	-0.07
4	-0.09	-0.14
5	0.03	-0.02
8	0.01	-0.03
9	0.02	0.01
10	0.15	0.13
11	0.08	0.08
12	0.07	0.04
13	0.02	-0.01
14	0.08	0.08
16	0.07	0.05
17	0.02	0.01
18	-0.07	-0.07
19	0.08	0.08
20	0.07	0.06
21	0.11	0.08
22	0.02	0
23	0.07	0.07
24	0.03	0.03
25	-0.02	-0.02
26	0.03	0.03

Table 3: The average vertical wind for each flight, before and after application of the pitch-correction algorithm developed in this section. The data restriction applied was that the true airspeed be above 130 m/s, absolute value of the roll be less than 5° , and the flight level be above 25,000 ft (to emphasize normal research measurement conditions in the DEEPWAVE project). Flights 6, 7, and 15 are also missing, as explained in the text.

The mean value of the vertical wind, for all flights combined, was 0.03 m/s for the uncorrected measurements and 0.02 m/s for the corrected measurements, with standard deviations of

0.06 m/s, so both are well within expected tolerances. The pitch correction has little effect on these mean measurements or the overall standard deviation.

Unlike the reverse-course comparison, the small offset obtained with the pitch corrections applied does not indicate that the measurements are only uncertain within these limits, because most flights are long compared to the Schuler-oscillation period of about 84 min, so flights will average over an oscillating correction that can average to a much smaller correction than that actually applied. More significant is the standard deviation of the applied correction, which amounts to 0.082° averaged over the enter project. That magnitude of standard deviation indicates that the correction to vertical wind arising from application of the pitch-correction algorithm introduces changes with standard deviation of about 0.3 m s^{-1} project-wide. Studies of individual flights show that this varies significantly from flight to flight. This uncertainty, however, is a significant contributor to the uncertainty in vertical wind. Response to fluctuations with period small compared to the 84.4 min period of the Schuler oscillation should be affected by the pitch correction via the possible introduction of a slowly varying bias of typically 0.3 m/s long-term standard deviation.

The procedure developed here is not suited to application during normal processing of data files because it uses a fit to the entire sequence of ground-speed measurements to find the corrections. A procedure has been developed to add values of pitch and vertical wind after correction, but this must be run after the original file is generated.

The procedure developed here only applies to the Honeywell IRUs. The C-MIGITS units already incorporate Kalman feedback from a GPS signal and so already apply a correction similar to the one applied here.

4 Sensitivity coefficients

This section reviews the determination of "sensitivity coefficients" that provide parameterized measurements of the angles of the relative wind (angle of attack and sideslip angle) in terms of measured quantities like pressure differences between ports on the radome. These sensitivity coefficients are essential for measurement of the relative wind, as described in Sect. 2.1.2, Eq. (1). DEEPWAVE Flight RF15 on 3 July 2014 was devoted to calibration maneuvers, and measurements from that flight, combined with similar calibration maneuvers flown on RF11 at 40,000 ft, are used to determine sensitivity coefficients for angle of attack (AKRD and AK_GP) and for sideslip (SSRD and SS_GP). A larger data set, described below, is also used to study the representativeness and uncertainty of the resulting sensitivity coefficients. This section also discusses some aspects of the relative timing of the measurements.

4.1 Angle of Attack

4.1.1 Equations underlying the calibration

The first-order expression for the vertical wind w is

$$w = V \sin(\alpha - \phi) + w_p \quad (22)$$

where V is the true airspeed, α the angle of attack, ϕ the pitch, and w_p the vertical motion or rate-of-climb of the aircraft. The solution for the angle-of-attack is

$$\alpha = \phi + \arcsin \frac{w - w_p}{V} \quad (23)$$

If it is reasonable to assume for some period of flight that w is zero, or that it averages to zero, then

$$\alpha^* = \phi - \arcsin \frac{w_p}{V} \quad (24)$$

can be used as a reference angle-of-attack to which to fit a parameterized formula. This fit reference depends on measurements of pitch, rate-of-climb, and true airspeed. Even in the presence of waves, fitting functions of the radome measurements and other flight characteristics to this reference should average any real effects of vertical wind as long as the vertical wind over the flight segments used averages to zero.

The danger in this approach is that a particular data set may not have negligible average mean wind. For example, if a flight spent more time in the updraft regions in the ascending portion upwind of the island and less in the downdraft region downwind of the island, the mean measurement of vertical wind may not be negligible. The functions used for representation of angle of attack always include an offset term along with functions of measurements, so it may be appropriate to adjust that offset if there is evidence that the mean vertical wind should not be zero.

Other steps can be taken to check that offset coefficient, as discussed in subsequent sections. One compromise, followed below, is to determine any coefficients other than the offset term from comprehensive data sets but then revised the constant coefficient in the fit on the basis of special periods expected to average to zero vertical wind, like flight over the ocean well away from weather disturbances or special calibration flights in conditions with apparently level air motions.

In the case of the radome, the relevant variables are $\phi = \text{PITCH}$, $w_p = \text{GGVSPD}$, and $V = \text{TASX}$. The radome measures the pressure difference (ADIFR) between top and bottom ports on the radome, and this pressure is usually normalized by some measure of dynamic pressure like QCF or QCXC or QCRC. The former is preferable because the use of corrected QCXC requires the application of static-defect corrections that themselves depend on α , leading to circularity in the calculation, and QCR and QCRC are sometimes affected by icing or freezing of accumulated water even when ADIFR continues to function.

For the gust pod, the relevant variables are $\phi = \text{CPITCH_GP}$, $w_p = \text{CVSPD_GP}$, and $V = \text{TASX}$. The gust-pod measurements differ from those measured relative to the fuselage; for example, the pitch of the gust pod is several degrees different from that of the fuselage because of the way in which the gust-pod IRU is installed. However, the true airspeed V in (24) is measured better by the fuselage system, so TASX will be used for V . The equation with the appropriate variables is then:

$$\alpha^* = \text{CPITCH_GP} - \arcsin \frac{\text{CVSPD_GP}}{\text{TASX}} \quad (25)$$

"Calibration" of the angle-of-attack (i.e., determining the sensitivity coefficients) then requires determining a function $f(\{x_i\})$ of measured quantities that matches α^* determined from (25). Possible terms $\{x_i\}$ in that function may include ADIFR and related measurements of pressure and dynamic pressure as well as Mach number, and powers and products of these terms. For the Rosemount 858 sensor used with the gust pod, it is expected from theory that one element of $\{x_i\}$ will be ADIF_GP/QC_GP. Wind tunnel and theoretical studies predict how the pressure will vary on a hemispheric surface with changing angles, but those don't necessarily apply to the mounting location on the GV because there is considerable flow distortion at the under-wing location of the pod and that affects the pressure response to changes in flow angles. Therefore, the best approach is to use the above approach for that sensor also and determine a functional response that matches the calibration data.

4.1.2 Application to the radome

The best method for calibrating angle-of-attack is through the use of speed runs. In this maneuver, the aircraft is slowed to a speed near the lower range of its operating range, then accelerated to near the upper limit, and then slowed again to normal cruise. If this is done while flying a level track, the angle of attack will vary through its normal range and the pitch will vary similarly. If there is no vertical wind or if a fluctuating vertical wind averages to zero, (24) then can be used to provide a reference angle α^* that serves as reference for the parameterized fit. There were three speed runs during RF15, at the times 3:21–3:29, 4:15–4:23, and 5:01–5:11 UTC. On RF11, there was a similar speed run flown from 10:30–10:40. For the purpose of this

first determination of sensitivity coefficients for angle-of-attack, only those periods were used. In addition, because some of the measurements at minimum speed deviated from the otherwise simple fits, only measurements with true airspeed in excess of 130 m/s were used; this eliminated some of the slowest parts of the speed runs, but that is a flight speed not used in normal operation.

In the code being used (cf. WindUncertainty.Rnw), the line

```
AOAREF <- PITCH - asin(GGVSPD/TASX) / Cradeg
```

represents Eq. (24).

The sensitivity to the pressure difference between vertically separated ports is the most important part of the calibration of angle of attack. Secondary terms are sometimes needed to adjust the value to maintain a correct zero. Therefore, the fit was done in two stages. First, the four speed runs alone were used to determine the sensitivity to the pressure ratio, and then a larger dataset was used to incorporate a wider range of flight conditions to check that the fit determined from the speed runs remained representative of the larger data set.. The first fit was to the following simplified equation:

$$\alpha^* = c_0^* + c_1^* \frac{\Delta p_\alpha}{q} \quad (26)$$

A fit to the data is shown in Fig. 20 and tabulated in the following summary of the fit, which was produced by the “R” call at the top of the listing. AOAREFC is α^* with correction to pitch as in Section 3 and AQR= $\Delta p_\alpha/q$.

```
## lm(formula = AOAREFC ~ AQR, data = Data2)
## [1] "Coefficients:"
##              Estimate Std. Error t value Pr(>|t|)
## (Intercept)  4.394    0.005672 774.6     0
## AQR         20.985   0.068935 304.4     0
## [1] "Residual standard error: 0.121, dof=1977"
## [1] "R-squared 0.979"
```

This fit gave coefficients c_0^* and c_1^* equal to 4.394 and 20.985. The fit accounted for 97.9% of the variance and had a residual standard error of 0.12° , so it represented the speed runs well. In Fig. 20, the thin grey line under the thick orange dashed line represents the uncertainty in the fit result and shows that the uncertainty in representing these data with this set of coefficients is negligible. The more significant uncertainty, however, comes from the assumption that the vertical wind is zero for these periods of the speed runs. Therefore, additional studies will be used below for further evaluation of the uncertainty introduced by this assumption.

This calibration would be affected by a time difference between the IRU measurement of pitch and the data-system sampling of the pressures involved, especially that from the radome. The IRU outputs measurements with a time delay that can be variable and unknown but is expected to be <0.1 s, and normal processing uses an adjustment of 60 ms to compensate for this delay. To guard against this delay affecting the calibration, a series of fits like that leading to the above

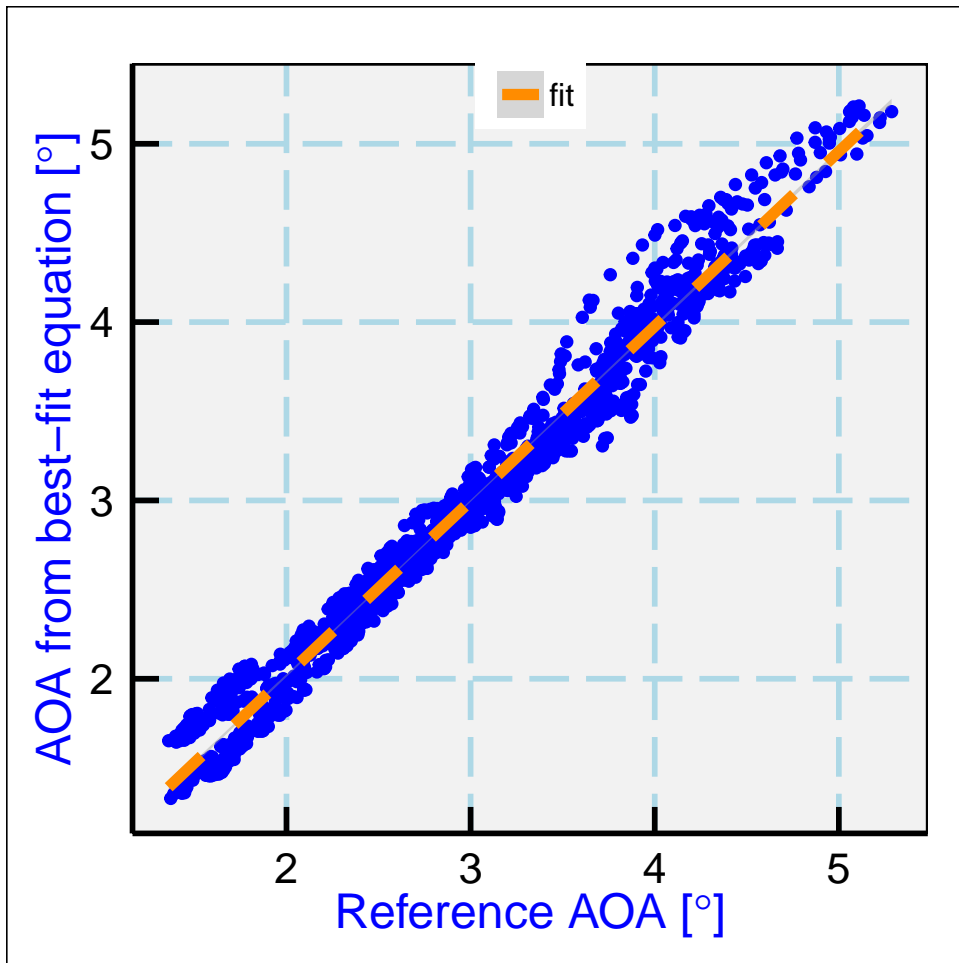


Figure 20: The angle-of-attack determined from the fit to pressure measurements from the radome, as a function of the reference angle provided by Equation (26), for the combination of data from all four speed runs as listed in the text.

formula and coefficients were performed after shifting the measurement of pitch by various time intervals, both forward and backward. For shifts within about 0.5 s, the results did not change significantly, although the fit with adjustment of pitch *backward* by about 0.5 s had the smallest standard error. Equivalently, a similar standard error was obtained if the measurement of the pressure ratio from the radome (δp_α) were moved forward in time by a similar amount. Neither of these shifts seems likely at this magnitude, and the change in standard error was only about 0.002° , so we interpret this as indicating insensitivity of the calibration to small shifts in time. That is likely a result of the calibration data being from speed runs where the flight speed is gradually increased and then decreased, so any effect of a lag partially cancels in such data segments.

The calibration would also be affected by pitch errors such as are discussed in Sect. 3. Therefore the correction procedure discussed in that section was applied to these data before finding the preceding fit. In comparison to the fit without this correction, the standard error was changed only negligibly and the two fit coefficients changed by -0.007 and -0.004, respectively, so this correction also had only minor effect on the fit, with changes comparable to or smaller than the standard errors in these coefficients. This insensitivity perhaps arises because the period of the calibration spanned a few hours and so included enough time for the Schuler oscillation of pitch to average over the dataset used for calibration.

Previous studies of the radome where low-altitude flight segments were included indicated that an additional term was needed in the calibration to adjust the zero for vertical wind for flight in the boundary layer over the ocean. The standard calibration determined in that way is that given in the RAF document on [Processing Algorithms](#):

$$\alpha = c'_0 + \frac{\Delta p_\alpha}{q} (c'_1 + c'_2 M) \quad (27)$$

with coefficients $\{c'\} = \{4.604, 18.67, 6.49\}$. The last term provides some adjustment dependent on Mach number and corrects an offset often seen in vertical wind at low airspeed.

Figure 21 shows the angle of attack determined from this fit vs. that from the standard formula. The plotted shapes show the distribution in values for centered intervals in the predicted angle-of-attack of $(1/3)$ degree, where the blue shapes and orange line are the results from the fit to the speed-run measurements and the green shapes are the distributions that would result from using the standard calibration. The standard calibration is close to that determined from the speed runs, but the RMS difference between predicted values and fit values increases from 0.12° for the speed-run fit to 0.15° for the standard fit. The difference is most evident for measurements at large angle-of-attack, where the standard coefficients produce increasingly higher values as the angle-of-attack increases.

Because the standard fit in use for the GV include an additional terms representing dependence on Mach number, the benefit of using such a fit for DEEPWAVE is worth considering. The primary reason for that fit has been that otherwise the measurements of vertical wind at low level tend to be biased, but most of the useful flight data from DEEPWAVE was at intermediate or high levels so this may not be a concern for this project.

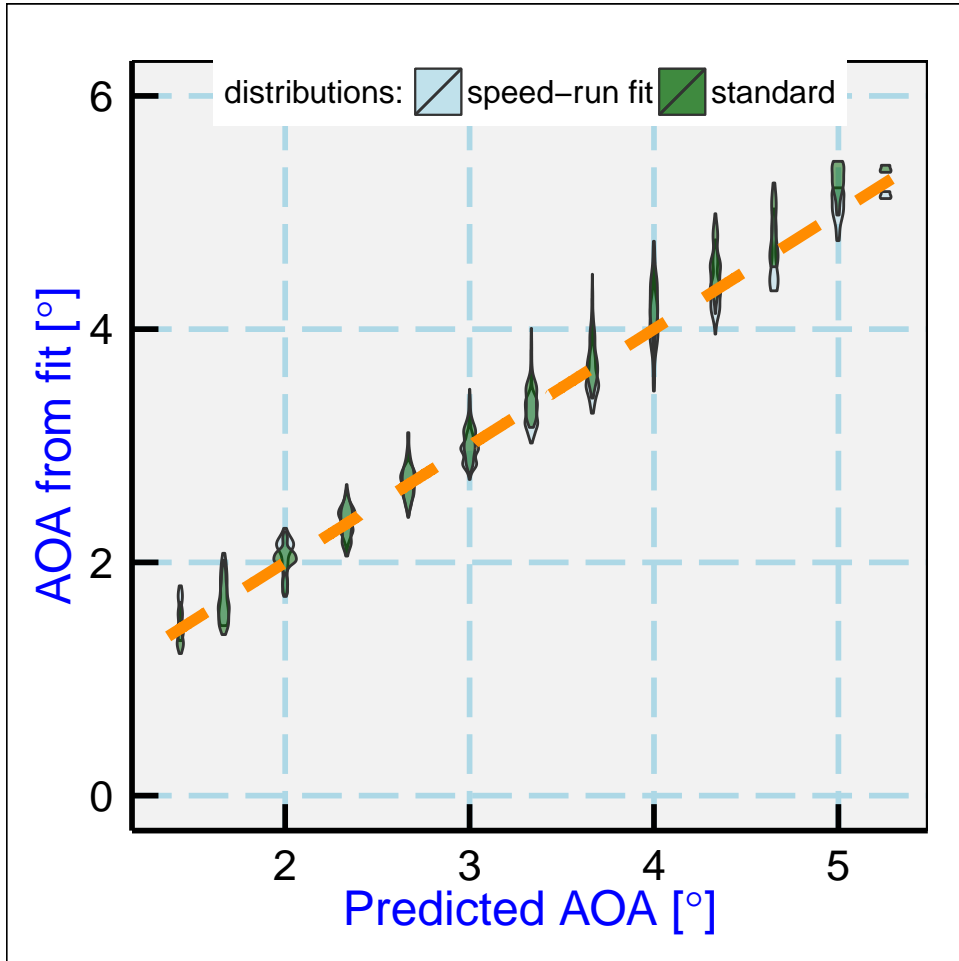


Figure 21: The angle of attack determined from the simple fit to the pressure ratio from the radome, as a function of the angle-of-attack predicted for zero vertical wind from the formula in the text (blue shapes), and the corresponding distribution that would result from using the standard calibration (green shapes). The shapes show the distributions for measurements in centered bins at (1/3)-deg increments in the predicted angle-of-attack. The dashed orange line is the best fit to the speed-run measurements.

```

## lm(formula = AOAREF ~ AQR + AQRM, data = Data2)
## [1] "Coefficients:"
##              Estimate Std. Error t value
## (Intercept)    4.387   0.005403 812.04
## AQR           17.925   0.216766  82.69
## AQRM          4.293   0.288610  14.87
##              Pr(>|t|)
## (Intercept) 0.000e+00
## AQR         0.000e+00
## AQRM        1.644e-47
## [1] "Residual standard error: 0.115, dof=1976"
## [1] "R-squared 0.981"

```

Fitting (27) to the speed-run data gave a standard error that is reduced by $<0.006^\circ$, so for those measurements this small improvement does not seem to justify adding another term to the fit. This will be revisited later in this section with an expanded data set.

The next step was to expand the data set to include flights from a range of altitudes including up to FL450, and to see if it is necessary to refine the fit to include additional terms like that in Eq. 27 to constrain the zero of the angle-of-attack while preserving the measured sensitivity as in (26). The expanded dataset included RF14, with a FL450 leg from 11:30 to 12:20 UTC; RF16, with a FL430 leg from 9:30 to 11:00 UTC; RF03, all measurements above 35,000 ft flight altitude (to incorporate a long flight where fuel burn-off changed the angle of attack); and an expanded section from RF11 (in addition to the speed runs) from 7:00 to 10:00 UTC, to include a long leg at FL400.

Various fit equations were explored involving terms including the Mach number, the air density, the measured pressures, and various products and powers of these terms including terms multiplied by the basic pressure ratio already included in (26). None of these produced enough improvement over the single-term fit to warrant their inclusion; the best improvement in the residual standard error was about 2%.³

The results from the two-coefficient fit to the larger data set, using

$$\alpha = c_0 + c_1 \frac{\Delta p_\alpha}{q} , \quad (28)$$

led to best-fit coefficients $\{c_0, c_1\} = \{4.46, 21.414\}$ and a standard error of 0.13 for 17,715 measurements. The small increase in standard error in comparison to the speed-run measurements is expected because this expanded data set includes regions more likely to have non-zero vertical wind, which contributes to this error. Expanding this fit to include a third coefficient as in (27) resulted in negligible improvement (0.001°) in the standard error, and introduction

³Additional terms that did improve the fit significantly were those correlated with the terms in Eq. 24, esp. pitch, but including such terms is not consistent with finding a fit that would represent the angle-of-attack in conditions with non-zero vertical wind. For example, including "PITCH" as a term in the fit resulted in a coefficient for this term of about 0.4, and such a large correlation between resulting measurements of angle-of-attack and pitch would bias the response to a true vertical wind. As an extreme example, inclusion of a term based on the right side of Eq. 24 leads to a perfect fit, but use of such a fit would ensure that all measurements of vertical wind would be zero. For this reason, pitch and vertical aircraft motion were excluded from the candidate terms in the fit.

of a set of eight possible dependencies while exploring for better fits only led to reduction in the standard error by 0.003° , so more complicated equations than (28) do not appear to be needed.⁴ Another fit considered with this expanded data set was to set the slope parameter to the value obtained from the speed-run data, 20.985, and then fit using the expanded data set to determine a value of the offset coefficient that minimized the mean vertical wind. That gave a value for the first coefficient of 4.428 and a standard error negligibly different from that for the two-coefficient fit, so that is another indication that the speed-run dataset and the expanded dataset give consistent results.

The recommended calibration for DEEPWAVE, determined with correction of the pitch errors as discussed in Sect. 3, is (28) with these values for the coefficients: $\{c_0, c_1\} = \{4.46, 21.414\}$.

Evaluation of all the points in the larger dataset using three fits, that from the larger dataset, from the speed runs alone, and using the "standard" fit discussed above, gave only very small differences in the results: the angle-of-attack evaluated from the larger-dataset coefficients resulted in values $0.034 \pm 0.007^\circ$ larger than those from the speed-run coefficients and $0.033 \pm 0.042^\circ$ larger than those from the standard coefficients, so using any of these formulas would give about the same results. Still another determination of the sensitivity coefficients was based on the full set of measurements from all flights in the DEEPWAVE project; that led to coefficients $\{4.437, 21.193\}$ and a difference in angle of attack relative to the reference data set above of $-0.007 \pm 0.004^\circ$. One measure of uncertainty in the results from applying these fits is that the various fits differ by about 0.03° in resulting angle-of-attack.

In Fig. 22 the values of angle-of-attack obtained using the fit to data from the expanded dataset are compared to those obtained using the fit to the speed-run dataset.

The standard errors in the coefficients for the larger dataset are respectively 0.0041 and 0.053, so the coefficients are tightly constrained by the fit. Surprisingly, the correlation between error terms was very high and positive, increasing the combined effects of these errors in any calculation of angle-of-attack. The larger dataset provided results consistent with those from the speed runs alone but contained 17,721 measurements vs. only 2,019 for the speed-run dataset, so the larger set provides an opportunity to examine the consistency of results from subsets of the measurements. For this purpose, randomly selected but exclusive subsets of the data were selected repeatedly and the fit coefficients were determined from each of these subsets. In one example, the dataset was divided randomly into 100 subsets and the fit coefficients calculated for each of those subsets, and then this process was repeated 50 times. The resulting standard deviations in the fit coefficients were 0.070 and 0.88. Repeating this for different subset sizes N indicated that the standard deviations in the coefficients scaled in a manner consistent with \sqrt{N} behavior, suggesting that the results are not biased by isolated outlier measurements such as would occur from regions with true vertical wind. The subsetting also revealed that the individual coefficients were highly correlated, with correlation coefficient 0.99. The effect of this is that the two error terms add almost linearly, not in quadrature, in their effect on the final uncertainty in angle of attack.

⁴This simpler representation applies to the normal research flight levels of the DEEPWAVE project, levels above about 10,000 ft. Because expanded representations were needed in other projects to represent low-level flight data, and low levels are not included in this expended data set, it may be necessary to revisit this calibration with more terms if lower-level flight segments are to be analyzed.

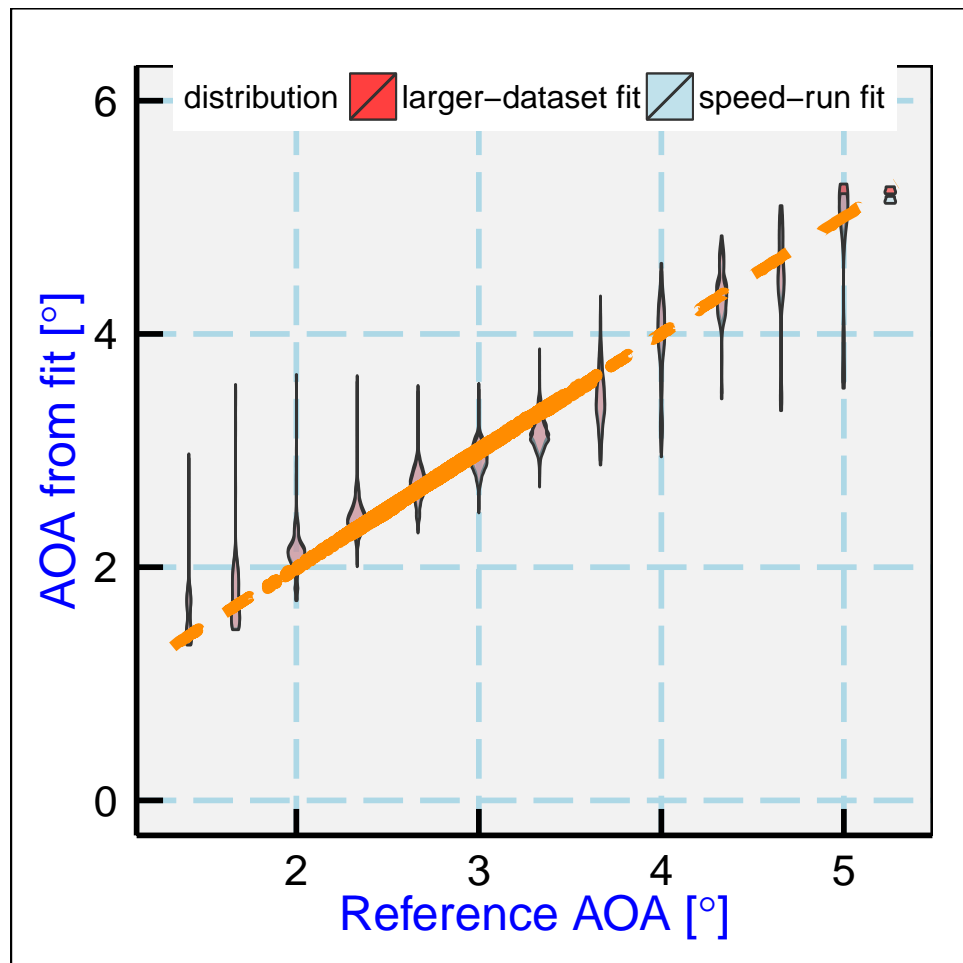


Figure 22: Distributions in the angle-of-attack determined from the two-coefficient fit to the expanded dataset, plotted with the distributions that would result from use of the equation based on the speed-runs only. The pink color denotes regions covered by both distributions.

The effect of these errors on the resulting angle of attack, for this dataset, was evaluated by applying randomly generated Gaussian fluctuations to the coefficients and calculating the net effect on the parameterized representation. The resulting standard error in angle-of-attack was 0.001° . However, because the speed-run values and standard values gave deviations relative to this calibration of about 0.03° , that may be a better estimate of the uncertainty in angle of attack from possible bias, with the smaller standard error representing the random component of that uncertainty. The net effect on vertical wind produced by 0.03° uncertainty in the sensitivity coefficients for angle-of-attack is therefore estimated to be about 0.1 m/s from uncertainty in the calibration.

One additional test was used to check the consistency of the measurements and to ensure that the project-mean vertical wind would be near zero for research-flight conditions. All flights that appeared to provide good data for the calibration procedure were combined into one dataset. The excluded flights were 6 and 7 (where there were problems with plugged lines in the radome), and 15 (the calibration flight, mostly at lower than research flight altitude). Also, the period from 9:50 to 10:30 UTC on flight 23 was excluded because the radome measurements looked suspicious and might have been affected by blockage. Pitch corrections as discussed in the preceding section were applied to these flights, and then the following tests were used to exclude periods not significant for the calibration: a) measurements where the true airspeed was less than 130 m/s, to exclude periods of anomalously high angle-of-attack, esp. during takeoff and landing when flaps and/or landing gear might be deployed; (b) periods when the roll angle was less than -5° or more than $+5^\circ$, to exclude turns; and (c) periods of flight below 35,000 ft pressure altitude, to emphasize the altitudes most used during research flights. More than 400,000 measurements were available for the fit after these exclusions.

```
## lm(formula = AOAREF ~ AR, data = DataC)
## [1] "Coefficients:"
##             Estimate Std. Error t value Pr(>|t|)
## (Intercept)  4.437    0.001058   4196      0
## AR          21.193   0.013873   1528      0
## [1] "Residual standard error: 0.118, dof=417799"
## [1] "R-squared 0.848"
```

The result was fit coefficients 4.437 and 21.193. These coefficients are similar to those determined for the subset data used previously, but they could be used instead if the goal is to minimize the offsets in mean vertical wind for the project because, for the constraints used, they will force a project-mean vertical wind of 0. A test of these coefficients for the segment of flight 12 away from the influence of South Island indeed led to a mean wind very close to zero, and flight-by-flight averages also as reasonably small with these coefficients.

4.1.3 Application to the gust pod

A similar approach was taken for the gust pod, but with variables translated to apply to the gust-pod instead of the radome: $\Delta P_\alpha = \text{ADIF_GP}$, $q = \text{QC_GP}$, $p = \text{PS_GP}$, and the Mach number M was that determined from the uncorrected measurements p and q from the gust pod. Apparently because of the under-wing location in disturbed airflow, a fit involving more terms was needed

to represent the reference measurements from Eq. 25. After exploration of various possible terms, the fit selected to represent the gust-pod was the following:

$$\alpha = b_0 + \frac{\Delta p_\alpha}{q} (b_1 + b_2 M) + b_3 \frac{q}{p} \quad (29)$$

```
## lm(formula = AOAREF_GP ~ AQR_GP + AQRM_GP + RR2_GP, data = Data2)
## [1] "Coefficients:"
##              Estimate Std. Error t value
## (Intercept) -0.9033   0.007859 -114.93
## AQR_GP       3.6024   0.068945   52.25
## AQRM_GP      4.2861   0.137577   31.15
## RR2_GP       1.3299   0.033660   39.51
##              Pr(>|t|)
## (Intercept) 0.000e+00
## AQR_GP      0.000e+00
## AQRM_GP     1.157e-173
## RR2_GP      4.461e-252
## [1] "Residual standard error: 0.099, dof=1975"
## [1] "R-squared 0.989"
```

The results of this formula are compared to the reference data in Fig. 23. The best-fit coefficients were $\{b_i\} = \{-0.903, 3.602, 4.286, 1.330\}$ and the square of the correlation was 0.989 with residual scatter (residual standard error) of 0.099. The fit was thus even better than that obtained for the radome for these same speed runs.

As for the radome, an all-project fit was obtained for the gust pod. In this case, different flights were excluded: 2, 3, 4, 11, 15, 17, 18, 19, 23, 24, 25 and the flight period from 8:05–8:40UTC on flight 1. In most cases, this was because the CMIGITS IRU providing gust-pod measurements of pitch seemed to have larger than normal deviations that appeared suspicious, so it was thought preferable to fit without those periods of suspicious measurements. The fit summary is as follows:

```
## lm(formula = AOAREF_GP ~ AQR_GP + AQRM_GP + RR_GP, data = DataC)
## [1] "Coefficients:"
##              Estimate Std. Error t value Pr(>|t|)
## (Intercept) -0.8058   0.002366 -340.6     0
## AQR_GP       3.2396   0.030400  106.6     0
## AQRM_GP      5.3580   0.049026  109.3     0
## RR_GP        1.2744   0.007171  177.7     0
## [1] "Residual standard error: 0.163, dof=315554"
## [1] "R-squared 0.861"
```

These coefficients $\{-0.806, 3.240, 5.358, 1.274\}$ may be preferable to the coefficients obtained above if it is desirable to minimize the all-project mean vertical wind for the gust-pod measurements.

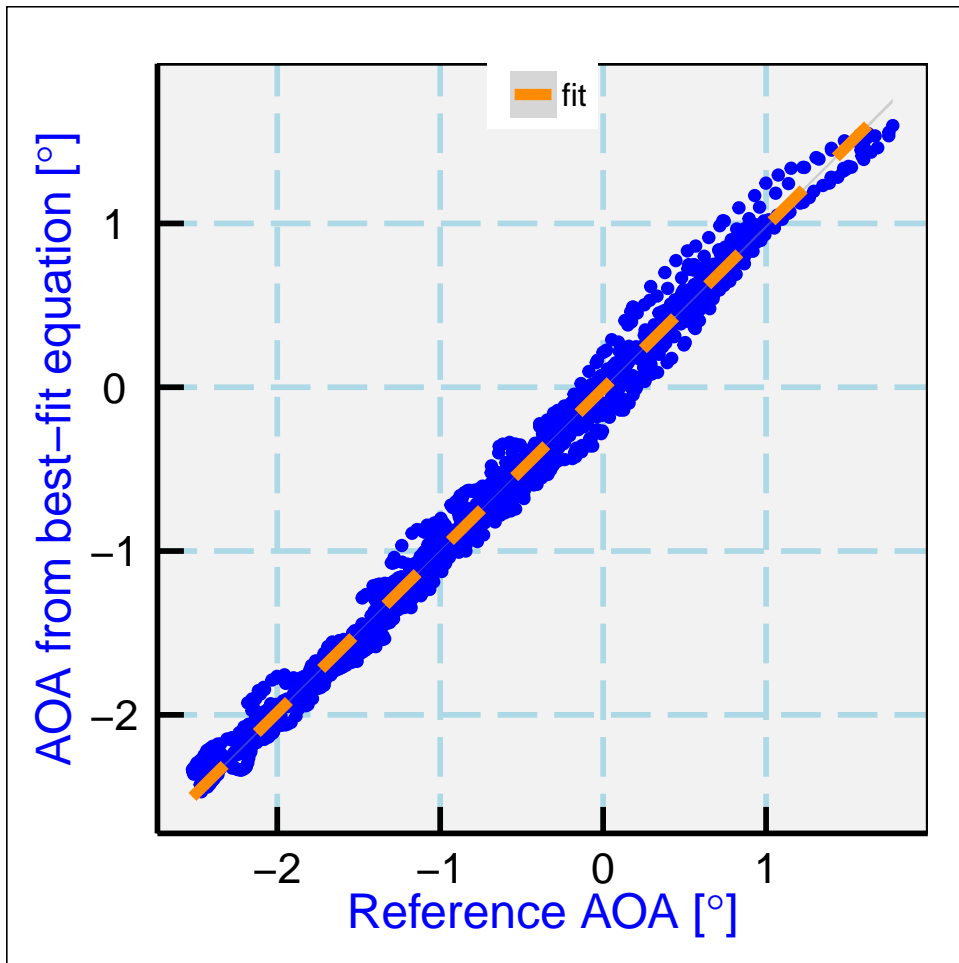


Figure 23: For the gust pod, the angle-of-attack determined from the fit as a function of the reference angle provided by (25), for the combined four speed runs. Compare to Fig. 20, the corresponding plot for the radome.

4.2 Sideslip Angle

4.2.1 Equations underlying the calibration

Calibration of the sideslip angle is more difficult, both because the equations are more complicated and because the maneuver is very hard to fly. Ideally, the sideslip maneuver should only change yaw angle and heading without change in roll, altitude, or angle-of-attack, but that is impossible to fly. It is practical, however, to minimize roll and change in altitude, and that was how these maneuvers were flown. The three sets of yaw maneuvers were at these times: 3:32:00–3:35:30, 4:31:00–4:33:30, and 5:26:40–5:29:30 UTC. Because the yaw maneuvers on rf11 (10:25:00 to 10:30:00) were flown in the old way, they were not combined with these new measurements, but it does not appear that the sideslip calibration has any significant dependence on altitude. In the case of yaw maneuvers, the calibration is based on the expectation that the horizontal wind remains constant. The first-order equations for the east and north components of the wind, u and v , are:

$$\begin{aligned} u &= -U_a \sin(\Psi + \beta) + u_p \\ v &= -U_a \cos(\Psi + \beta) + v_p \end{aligned} \quad (30)$$

where U_a is the true airspeed, Ψ the heading, β the sideslip angle, and u_p and v_p are the eastward and northward ground-speed components of the aircraft. These two equations lead to the following reference formula for β :

$$\beta^* = -\Psi + \arctan\left(\frac{u_p - u}{v_p - v}\right) \quad (31)$$

where the second term represents a correction for the change in direction of motion of the aircraft, which is difficult to avoid in the yaw maneuver. The measurements thus provide β^* , an estimate of the sideslip during the yaw maneuvers.

There is, however, a circular component in (31) because it involves the wind components and those require β for their measurement when sideslip changes. To reduce the feedback from this term, the horizontal wind components u and v were low-pass-filtered with periods ranging from 5–60 s and the filtered values were used in (31). Filtering made small differences in the fit coefficients but increased the residual error significantly, but 60-s filtering was still selected because that is a period long in comparison to the yaw maneuvers so it should reduce possible bias in the fit coefficients from use of the older sensitivity coefficients and any associated fluctuations in the wind measurements during maneuvers.

4.2.2 Application to the radome-based and gust-pod systems

For both systems, a relatively simple fit was sufficient, in the following form:

$$\beta = e_0 + e_1 \frac{\Delta p_\beta}{q} \quad (32)$$

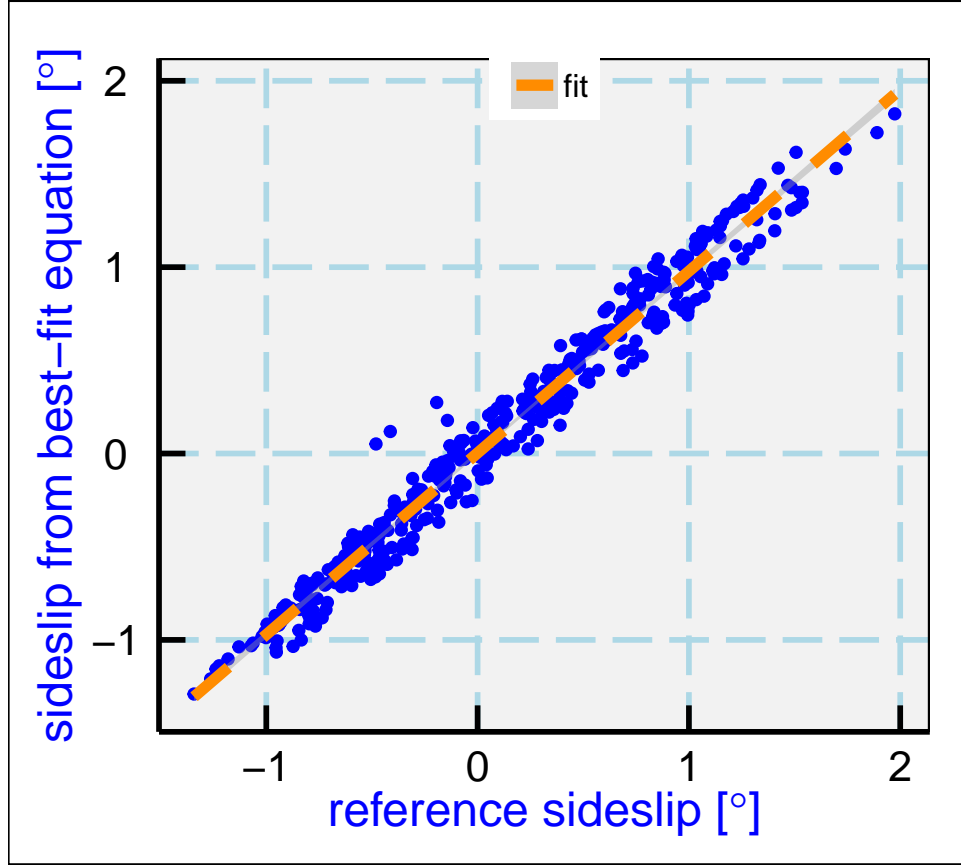


Figure 24: The sideslip attack determined from the fit, as a function of the reference angle provided by Equation (31), for the combination of data from all three yaw maneuvers listed in the text. The gray area underlying the dashed orange line denotes the standard-uncertainty range for the fit.

where Δp_β is the pressure difference between horizontally separated pressure ports and q the dynamic pressure. For the radome, $q = \text{QCF}$ and $\Delta p_\beta = \text{BDIFR}$; for the gust-pod, $q = \text{QC_GP}$ and $\Delta p_\beta = \text{BDIF_GP}$. The resulting fit for the radome is listed below:

```
## lm(formula = SSREF ~ BQR, data = DataV)
## [1] "Coefficients:"
##                   Estimate Std. Error t value
## (Intercept)  0.09186   0.005428 16.92
## BQR        22.30232   0.170349 130.92
##             Pr(>|t|)
## (Intercept) 7.321e-50
## BQR          0.000e+00
## [1] "Residual standard error: 0.114, dof=441"
## [1] "R-squared 0.975"
```

The best-fit coefficients were $\{e\} = \{0.092, 22.302\}$, the squared correlation was 0.97 and the residual standard error was 0.114, as listed above. The plotted measurements and this fit are shown in Fig. 24. The near-zero first coefficient is a forced result from using calculated wind

components in (31). The sideslip offset that is represented by this term will be determined later by other means; cf. Section 6.1.2.)

The standard calibration in use for the GV has coefficient $e_1=21.155$, slightly smaller than the value determined from this calibration.

For the gust-pod, the same approach was followed, giving a fit with characteristics as listed below:

```
## lm(formula = SSREF_GP ~ BQR_GP, data = DataV)
## [1] "Coefficients:"
##             Estimate Std. Error t value
## (Intercept) -3.621     0.02624 -138.01
## BQR_GP       12.184     0.13284   91.71
##             Pr(>|t|)
## (Intercept) 0.000e+00
## BQR_GP      2.305e-289
## [1] "Residual standard error: 0.164, dof=441"
## [1] "R-squared 0.950"
```

The squared correlation of this fit was 0.95 and the residual standard error was 0.164° . The best-fit coefficients were $\{-3.621, 12.184\}$. The difference in first coefficient vs the radome is a result of the offset in heading between the aircraft longitudinal axis and the gust pod. The detailed report for the fit is listed above, and the result of applying these sensitivity coefficients to the measurements from the gust pod is shown in Fig. 25.

An additional study is needed to determine the sensitivity coefficients for sideslip. An offset in sideslip, arising from an erroneous first coefficient e_0 in the calibration, would produce an offset in the lateral component of the measured wind, and that erroneous lateral component would enter the calibration equation to again give a first coefficient near zero. An offset therefore must be determined in another way. Two candidates for finding the offset are reverse-heading maneuvers, during which the horizontal wind component lateral to the aircraft should remain constant but change sign, or circle maneuvers, during which an offset in sideslip will appear as a sinusoidally varying perturbation to the wind. Later in this report, a set of circles, flown with constant roll, will be used in Section 6.1 to obtain a better estimate of the sideslip offset. .

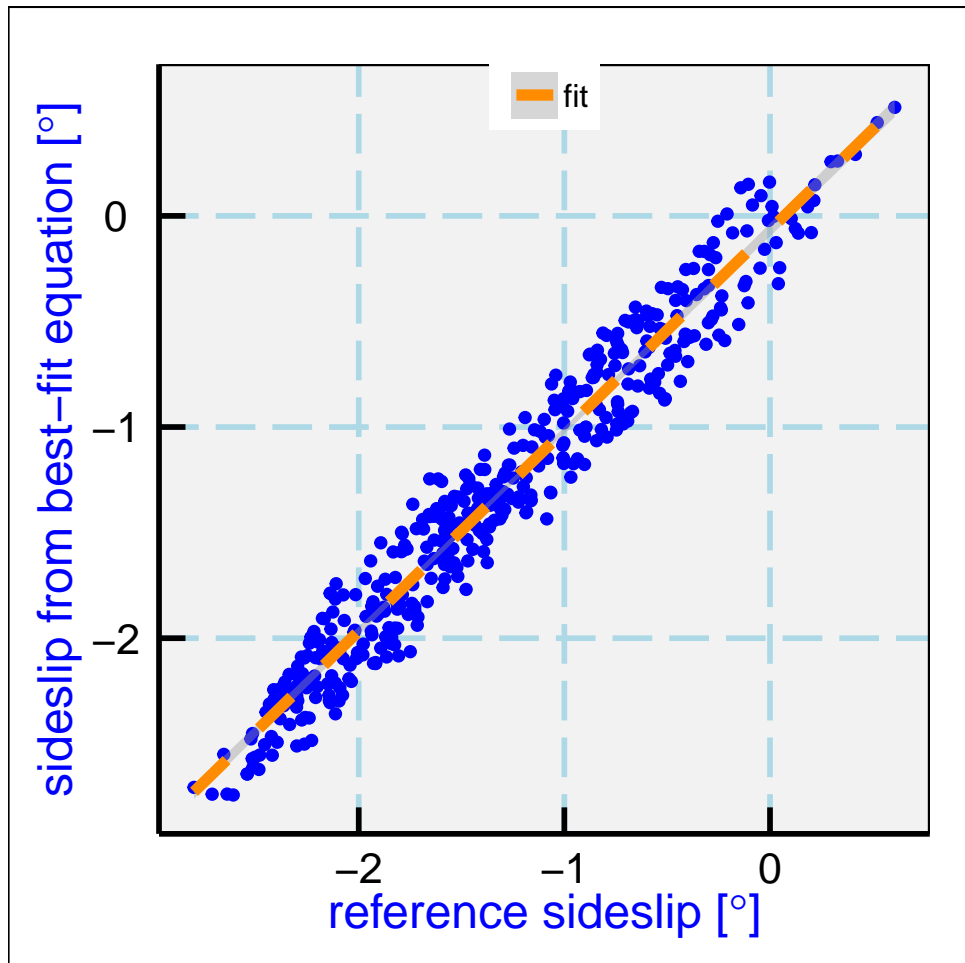


Figure 25: As in the preceding figure but for the gust-pod system.

4.3 True Airspeed from the Gust Pod

The measurements ADIF_GP and BDIF_GP, normalized by QC_GP, are used with the calibrations in the preceding section to find the angle-of-attack and sideslip. In addition, to find the relative wind, a measurement of true airspeed (TAS) is needed. In an effort to allow the gust-pod system to operate independently of the standard radome-based system, it is desirable to determine the true airspeed directly from the gust-pod measurements. However, the standard system has been calibrated to low uncertainty by reference to the Laser Air Motion Sensor, so for the purpose of calibration that true airspeed (TASX) will be used as a reference. Once the gust-pod measurement of true airspeed is calibrated, the gust-pod system still measures wind without future reference to the standard system, but the calibration process links the two systems to have a common reference for TAS.

Therefore, the next step needed to use the gust pod wind-sensing system is to determine a functional relationship between gust-pod measurements and the true airspeed. The approach taken is to fit the basic pressure ratio q/p as measured by the 858 probe to match the corresponding pressure ratio provided by the conventional measurements of dynamic and static pressure. The relationship represents the true ratio of dynamic to static pressure, so using that ratio the normal calculation of true airspeed can be used to determine the TAS measured by the gust pod. For this purpose, all the measurements from the calibration flight (RF15) were used qualified only by requiring TASX>130 m/s.

The measurements entering the resulting fit are as follows: $q=QCXC$ is the reference dynamic pressure, $p = PSXC$ is the reference ambient pressure, $q_g = QC_GP$ is the gust-pod dynamic pressure, $p_g = PS_GP$ is the gust-pod static pressure, M is the Mach number determined from the reference measurements, M_g the Mach number determined from the gust-pod static and dynamic pressure, and $\Delta P_{\alpha,g} = ADIF_GP$ is the pressure difference between top and bottom pressure ports on the gust-pod sensor. The following equation was found to provide a useful representation of the reference ratio q/p in terms of quantities measured only by the gust-probe system:

$$\frac{q}{p} = b_0 + b_1 \frac{q_g}{p_g} + b_2 M_G \frac{q_g}{p_g} + b_3 \left(\frac{q_g}{p_g} \right)^2 + b_4 \frac{\Delta p_{\alpha,g}}{q_g} + b_5 M_G + b_6 \left(\frac{\Delta p_{\alpha,g}}{q_g} \right)^2 + b_7 \frac{\Delta p_{\alpha,g}}{q_g} M_G \quad (33)$$

This complexity in the equation was needed to obtain a good fit (with residual error translating to a typical error in true airspeed of about 0.5 m/s for typical DEEPWAVE research legs), and all terms were indicated to be significant in the fit. The fit details are listed below:

```
## lm(formula = B1 ~ B2 + BxM + I(B2^2) + AQR_GP + MachG + I(AQR_GP^2) +
##      I(MachG * AQR_GP), data = DataV)
## [1] "Coefficients:"
##                               Estimate Std. Error t value
## (Intercept)           1.2251    0.031366   39.06
## B2                  28.3047    0.838568   33.75
## BxM                -30.2417    0.959959  -31.50
## I(B2^2)              14.1312    0.410195   34.45
## AQR_GP             -0.5810    0.004283 -135.66
```

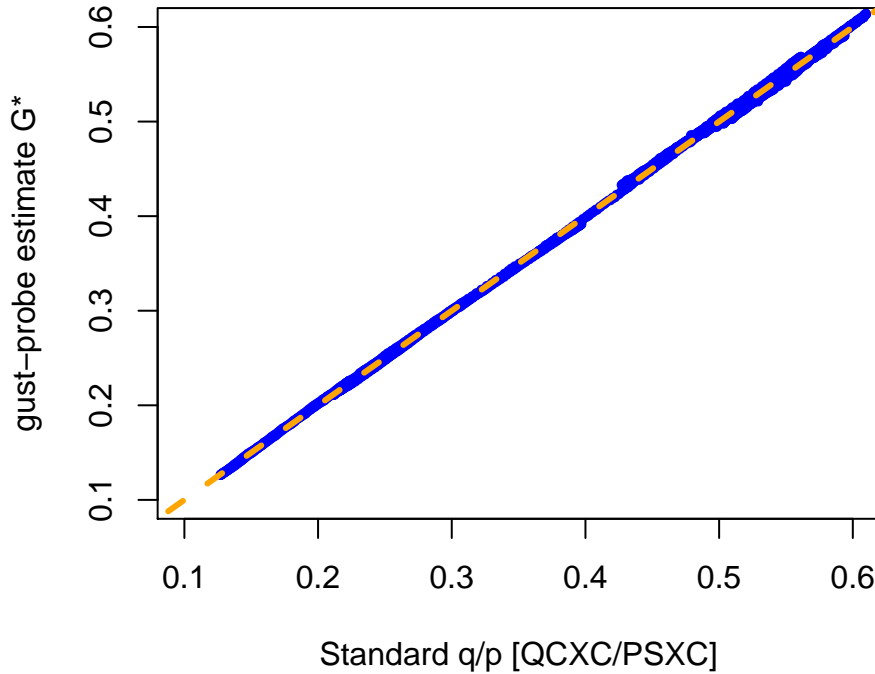


Figure 26: The estimate of q/p obtained from the right side of (33), determined entirely from measurements provided by the gust pod, plotted against the standard measurement obtained from QCXC/PSXC. The coefficients are listed in the text.

```

## MachG           -7.8344   0.224550  -34.89
## I(AQR_GP^2)    0.1492   0.002822   52.85
## I(MachG * AQR_GP) 1.2385   0.007353 168.43
## Pr(>|t|)        
## (Intercept)    6.917e-323
## B2             1.186e-243
## BxM            3.501e-213
## I(B2^2)         1.822e-253
## AQR_GP          0.000e+00
## MachG           9.544e-260
## I(AQR_GP^2)    0.000e+00
## I(MachG * AQR_GP) 0.000e+00
## [1] "Residual standard error: 0.002, dof=22394"
## [1] "R-squared 0.999"

```

The resulting fit is shown in Fig. 26. With this result for G^* from (33), the true airspeed can then be obtained using the usual formula, with G^* used in place of q/p :

$$V = \sqrt{2 \left(\frac{(c_p - R_a)}{R_a} \right) (1 + G^*)^{\frac{R_a}{c_p} - 1} \left(\frac{c_p}{c_v} R_a T \right)} \quad (34)$$

where c_p , c_v , and R_a are the specific heat of air at constant pressure, the specific heat of air at constant volume, and the gas constant for air and p is the static pressure, q the dynamic pressure, and T the absolute temperature.

The resulting true airspeed is compared to the conventional measurement in Fig. 27. The fit provides a reasonable representation of TASX, with a standard error of about 0.4 m/s. This is not much larger than the estimated uncertainty in TASX (about 0.3 m/s), so wind calculations might be based on this value if necessary. However, there is serious danger of over-fitting with this many coefficients and variables, even though the fit was improved significantly with each addition; indeed, the standard error in the q/p fit was reduced by 50% with the addition of the last two variables in the fit. Because of the danger that this variable might not perform as well when used outside the range of this fit (which was $\text{TASX} > 130$, $|\text{ROLL}| < 5$, and $\text{GGALT} > 5000$), it still should be better to base wind measurements from the gust pod on the conventional TASX combined with the relative-wind angles from the gust pod. However, if it is desirable to have a wind measurement that is completely independent of the standard radome-based system, using true airspeed measured with this fit might provide a useful alternative.

In particular, for the DEEPWAVE flights where the standard vertical wind measurement was compromised by an obstruction in the pressure-sensor lines of the radome, the best vertical wind will be that calculated using (29) for the angle of attack but conventional TASX for the true airspeed, because the pressure ports used to determine TASX are not obstructed.

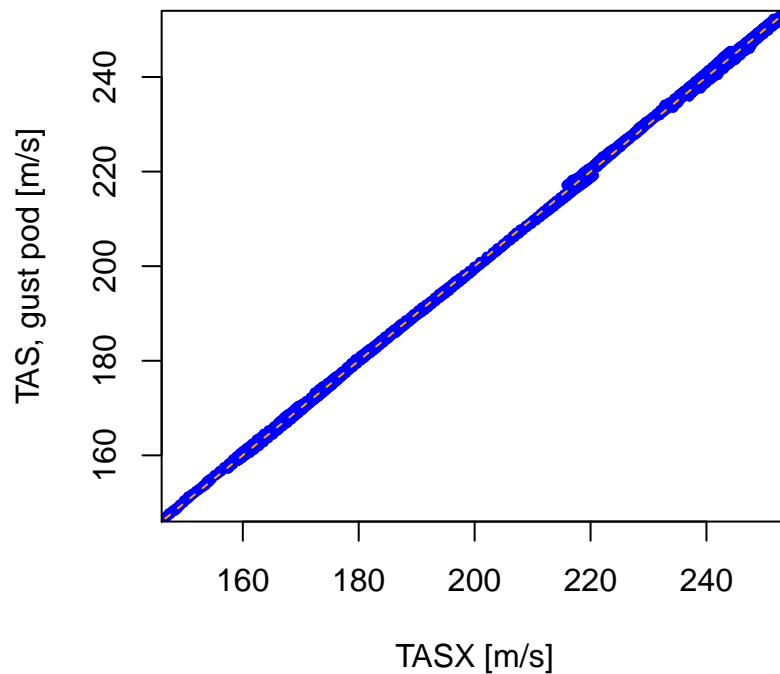


Figure 27: True airspeed obtained from the gust pod, plotted against corresponding measurements from the conventional measurement system (TASX)

4.4 Summary of sensitivity coefficients

4.4.1 Angle of Attack

Radome: Eq. (28), coefficients $c_{0,1} = \{4.46, 21.414\}$.⁵

Gust pod: Eq. (29), coefficients $\{b_{i=0,3}\} = \{-0.903, 3.602, 4.286, 1.330\}$ ⁶

4.4.2 Sideslip Angle

Radome and gust pod: Eq. (32), coefficients $\{e_0, e_1\} =$

$\{0.092, 22.302\}$ for the radome,⁷

$\{-3.621, 12.184\}$ for the gust pod.

4.4.3 True Airspeed, Gust Pod

Equation (34), with (33) and coefficients $\{b_{i=0,7}\} =$

$\{1.2251, 28.3047, -30.2417, 14.1312, -0.581, -7.8344, 0.1492, 1.2385\}$.

⁵See also the alternative coefficients $\{4.437, 21.193\}$ discussed on page 49.

⁶See also the alternative coefficients $\{-0.806, 3.240, 5.358, 1.274\}$ discussed on page 50.

⁷However, see the revision of the first coefficient that follows in Section 6. The value listed in the concluding summary of that section, in Section 6.1.3, should supersede the value listed here.

5 Studies of the Vertical Wind

5.1 Overview

The preceding sections provided extensive information on how vertical wind is measured and how the radome-based system is calibrated. Here, two additional topics not covered well there are discussed to complement those earlier discussions. The sections here deal with the choice and quality of the variable characterizing the vertical motion of the aircraft and some issues related to the relative timing of the measurements entering the calculation of vertical wind.

5.2 The vertical velocity of the aircraft

5.2.1 Available measurements

There are several independent measurements of the vertical motion of the aircraft:

Variable	Source
VSPD	Honeywell IRU
VSPD_A	Avionics system (Honeywell IRU)
GGVSPD	GPS receiver, possibly with OmniSTAR corrections
CVSPD_GP	CMIGITS IRU, gust pod
CVSPD_LAMS	CMIGITS IRU, LAMS pod

The standard vertical wind calculation depends on a measurement of vertical motion of the aircraft, which has been VSPD (from the IRU) or VSPD_G or GGVSPD (from the GPS) or, much earlier, WP3 from a baro-inertial update loop using VSPD. This updating is no longer used because the Honeywell IRU providing VSPD already incorporates such updating. For the systems based on the gust pod or LAMS, additional vertical-velocity measurements are provided by their pod-mounted IRUs, respectively CVSPD_GP and CVSPD_LAMS.

Because VSPD as provided by the Honeywell IRU is controlled against the known instability of IRU measurements in the vertical by updating to a reference value provided by pressure altitude, it has some drawbacks: pressure altitude is not really a measure of altitude but of pressure, so the reference altitude can be biased, and the IRU-imposed baro-inertial loop has unknown response characteristics and uncertainty. The advantage of an IRU variable over a GPS measurement has been, until recently, better response at high frequency at the expense of absolute accuracy. GPS measurements have now improved, esp. with OmniSTAR, so it is worth considering what variable or combination of variables should be used in the calculation of vertical wind.

For horizontal wind, the standard solution in use since the early 1990s has been a complementary-filter solution where the difference between IRU and GPS measurements is low-pass filtered and the result is added to the IRU measurement. This preserves the high-frequency response of the IRU measurement but causes the low-frequency components to match the GPS measurements, thus providing both absolute accuracy and valid high-frequency measurements. It seems worthwhile to explore a similar approach for the vertical wind, to see if there is an advantage to a

variable that is provided by an analogous complementary filter. When OMNISTAR is available, the measurement of vertical aircraft motion is so good that it may be preferable to use that directly, so that will be explored here also.

Some of the following references a variable GGVSPDB, a highest-resolution version of GGVSPD. GGVSPDB was used in this evaluation to ensure that the reduced resolution in GGVSPD did not influence the variance spectra, but GGVSPD is the usual variable used in wind calculation. It has sufficient resolution for that purpose.

In standard processing, two vertical-wind variables are produced from the radome-based system, WI and WIC. These are called, respectively, “Wind Vector, Vertical Gust Component” and “GPS-Corrected Wind Vector, Vertical Gust Component”. They are calculated by adding the relative wind measured by the radome system to the vertical motion of the aircraft, either VSPD (WI) or GGVSPD (WIC). The former is directly from the Honeywell IRU; the latter is produced by the GPS receiver and may benefit from OmniSTAR accuracy (flagged by GGQUAL equal to 5).

The names are not really appropriate. Neither is the gust component; both are the full vertical wind including relative wind and aircraft motion. Also, WIC is not GPS-corrected, it is completely based on the GPS and does not use the IRU at all except for the attitude angles need to determine the relative wind (the same for both). These calculations employ the nimbus function “gust”, which implements the algorithm described in Sect. 2.1.

In addition, the Honeywell IRU provides a measurement of vertical acceleration. In a special calculation, this was integrated to get velocity and the result compared to VSPD. The results of the integration and the variance spectrum of that result were quite similar to VSPD, provided that a feedback loop was used to avoid exponentially growing errors from positive feedback, so there is no advantage to using that integrated acceleration in place of VSPD. (It was hoped that some of the filtering imposed on VSPD could be avoided.)

5.2.2 Variance spectra for components affecting the vertical wind

For evaluation of these measurements of aircraft velocity, it is useful to compare the variance spectra among them, including coherence and phase, and to evaluate the contribution made to the vertical wind. For this purpose, one flight from DEEPWAVE, RF16 (4 July 2014) was used because it provided a good example of relatively intense and prolonged vertical motion, with the core 6 h period of the flight from 6:30:00 – 12:30:00 having a standard deviation in vertical wind of 1.0 m/s. Much of the variation in vertical wind was from waves, so the field was not fully developed turbulence, but the signals to be resolved had enough intensity that noise floors on the measurements were not a problem.

Figure 28 shows variance spectra calculated for the entire 6-h period, for a number of measurements entering the vertical-wind calculations. The thick blue trace shows the spectrum for the standard vertical wind measurement WIC, with a pronounced broad peak near 10 km wavelength, a relatively small inertial subrange extending only to about 2 km, and (after smoothing in 50 logarithmic intervals across the range of the plot) uncertainty estimates that range from about 5% at the lowest frequencies to <1% at the highest frequencies.

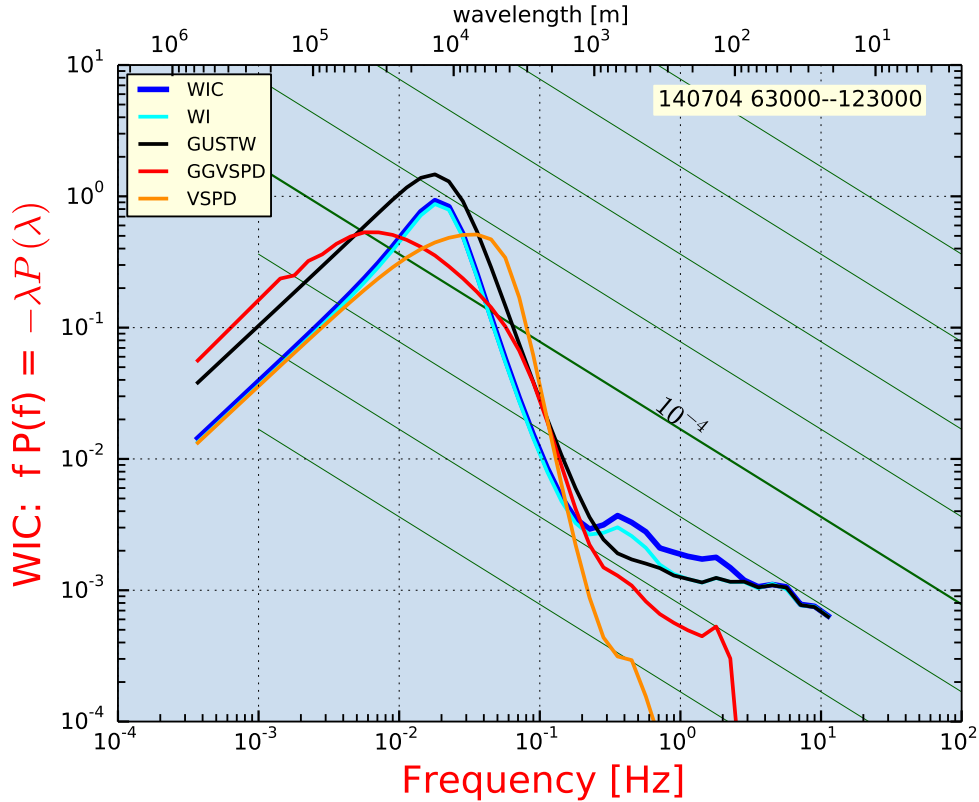


Figure 28: Variance spectra [units: m^2s^{-2} , density functions per logarithmic interval in frequency expressed in Hz] for various components entering vertical-wind calculations. Data are from DEEPWAVE flight 16, 6:30:00–12:30:00 UTC. The thick blue trace is that for the vertical wind variable WIC; others show either measurements of the aircraft vertical motion (VSPD, GGVSPDB) or, as GUSTW, the relative-wind contribution to WIC. The green diagonal lines show the slope expected for an inertial subrange and, for the heavy line labelled “ $!10^{-4}$ ”, corresponding to an eddy dissipation rate of $1 \times 10^{-4} \text{ m}^2\text{s}^{-3}$. Other green reference lines are displaced by an order of magnitude in eddy dissipation rate. Calculation method: all-poles or maximum-entropy method, with 100 poles, resolution 0.0005, with results smoothed in 50 bins in the logarithm of frequency. Total variance is $1.36 \text{ m}^2\text{s}^{-2}$.

The two measures of vertical aircraft motion, GGVSPD (from the GPS receiver) and VSPD (from the inertial reference unit) have important differences in their properties. At high frequency, VSPD (orange line) decreases rapidly with increasing frequency, so it makes negligible contribution to the vertical wind (WI) at frequencies above 1 Hz. In contrast, GGVSPD (red line) does not show a similar steep drop in variance until after about 2 Hz, and it continues to make an important contribution to WIC over the frequency range from about 0.3 to 3 Hz. The absence of spectral variance above about 0.3 Hz in VSPD appears to be the result of internal filtering of this signal in the inertial unit, and indeed some limited information on the properties of the signals does indicate filtering at about this frequency. Because the aircraft motion clearly has components in this frequency range (based on the ride in turbulence), it appears that WI should not be used for frequencies above about 0.3 Hz.

The inertial-system variable VSPD is also subject to pressure damping, and this may account for the difference between GGVSPD and VSPD at long wavelength. The aircraft normally flies with reference to the pressure altitude, so in a region of varying altitude at a given pressure there are fluctuations in the aircraft geometric altitude (red line) not reflected in the pressure altitude (orange line). Both contribute in ways that result in essentially the same spectral variance for frequencies below 0.3 Hz, as shown by the near coincidence of the blue and cyan lines, so the difference is not significant. Here also, though, the red line representing the GPS measurement is a better measure of how the vertical wind should be affected, because the pressure-damped orange line will not show real vertical motion of the aircraft as it remains on a pressure surface.

For these reasons, WIC is the preferable variable to use for vertical wind. This also answers the question posed earlier regarding the possibility of using a combination of measurements from inertial and GPS systems to obtain better frequency response. The IRU measurements turn out to have poorer frequency response and lead to apparent biases for frequencies around 1 Hz, so this is not a useful combination. Instead, it appears best to use the GPS-provided measurement of vertical aircraft speed without further modification.

There is still some reason for concern about the spectral response of GGVSPD at frequencies around 0.5–1 Hz, because there is no evidence that the GPS is providing valid response at this high rate. The unit used only provides measurements at 5 Hz and these measurements are interpolated and filtered to higher frequency, so the cut-off apparent in Fig. 28 is a result of that sampling and may remove a real signal at higher frequency.

The black trace (labeled GUSTW) is the vertical component of the relative wind. The sum of GUSTW and GGVSPD determines WIC, and the alternate measure of vertical wind WI is the sum of GUSTW and VSPD from the inertial reference unit. GUSTW has higher spectral variance than WIC for frequencies below 0.3 Hz, so at these frequencies the aircraft motion tends to counter the relative wind and reduce the measured variance. This would be the case, for example, if there were negligible vertical wind and the relative wind arose entirely from the vertical motion of the aircraft. On the other hand, for frequencies around about 0.5 Hz the spectral variance in the vertical wind exceeds that in the relative wind so the aircraft responds approximately in phase with the vertical gusts.

The high-frequency variance spectrum has a slope differing a small amount from the expected $-5/3$ spectrum, and that is cause for some concern, but the turbulence in this region was not very well developed or consistent so this is probably not cause for alarm. Very good agreement with

expectations has been seen in cases of boundary-layer measurements where well-developed turbulence at small scales is expected, but in those cases the intensity of turbulence at small scales was greater also. This is reason to continue to be suspicious of the response around 0.5–1 Hz.

Some of the relative magnitudes shown in Fig. 28 may change for different intensities of turbulence. However, some tentative conclusions seem indicated by this figure and the discussion above:

1. Consider eliminating the variable WI from the data archives. VSPD, on which WI is based, has problems at both high and low frequency. Providing this variable could lead to the mistaken expectation that this is the uncorrected version of WIC. The argument for using a variable based on VSPD has been that this formerly represented the high-frequency contribution better than a GPS variable. That is not the case any longer, because GPS measurements have improved greatly and the presently available IRU-provided measurements are obviously filtered at high frequency.
2. VSPD does not have better frequency response than GGVSPDB at high frequency, as might be expected; the reverse is the case, possibly because of filters imposed on VSPD in the inertial unit itself. This argues for direct use of GGVSPDB in the vertical-wind calculation, at least when OMNISTAR corrections are available.
3. The relative-wind variance spectrum exceeds that of the vertical wind, indicating that the contribution from aircraft motion counters the relative-wind contribution at all but the highest frequencies. The variable GGVSPDB is close to 180° out-of-phase with the relative wind (GUSTW in Fig. 28) for frequencies smaller than 0.2 Hz. At low frequency, the motion of the aircraft probably produces the vertical component of the relative wind; at intermediate frequency (near 0.1 Hz) the aircraft perhaps responds to the vertical wind so as to move out-of-phase with it, exaggerating the measured vertical component of the relative wind. There is a transition in phase from being above 180° to being below 180° as the frequency increases through 0.05 Hz, perhaps representing a transition from where the pilots or autopilot cause motions that produce the relative-wind vertical component to where the vertical wind causes the aircraft response.
4. At high frequency (>0.3 Hz), the gust component dominates over the aircraft response, the coherence between them falls to values between 0.1–0.5, and the phase relationship becomes variable before settling near zero at 0.5 Hz.

An example where there was very low turbulence is shown in Fig. 29. The intensity of vertical-wind fluctuations was quite small for this flight segment, with a standard deviation in vertical wind of only about 0.2 m/s. Some features of this plot are explained below:

1. The measured vertical wind at high frequency (>1 Hz) is a white-noise spectrum with intensity that can be matched by generating a random-noise signal with peak amplitude of 0.15–0.2 m/s, which would lead to a random error of about $(0.15-0.2)/\sqrt{12} \simeq 0.05$ m/s. The noise is dominated by the relative-wind contribution; there is essentially no contribution at these frequencies from the motion of the aircraft. The noise arises almost entirely

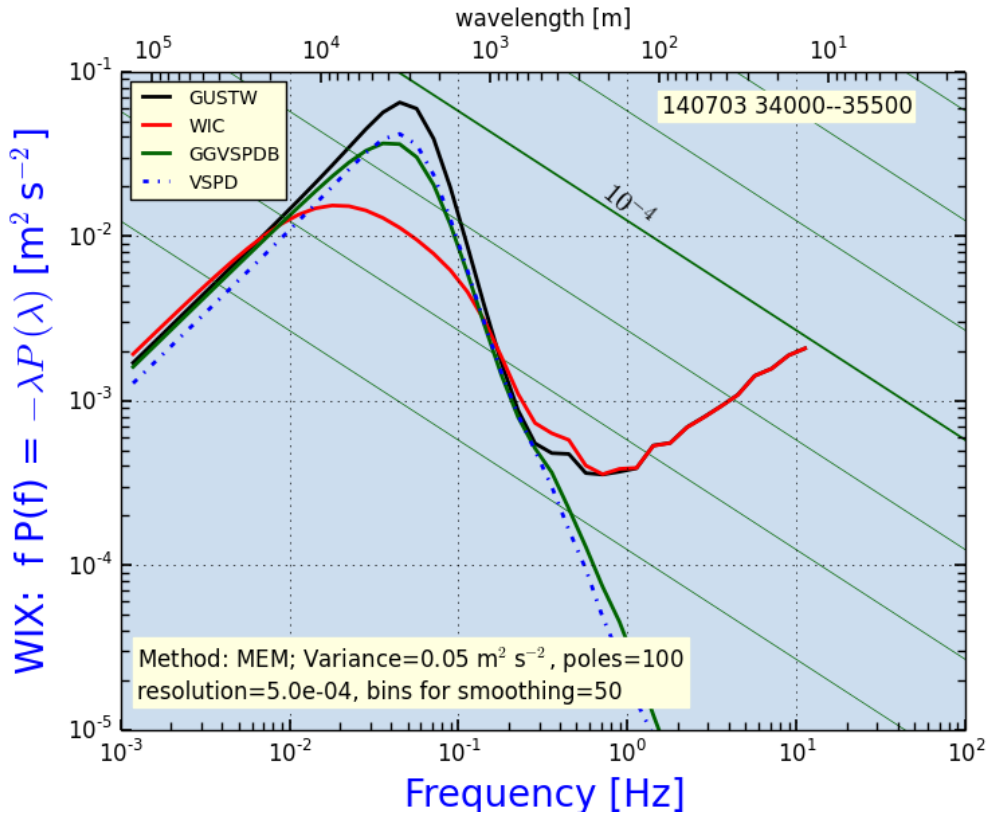


Figure 29: Variance spectra for the vertical wind (here, WIX) and for the contributions to it made by the relative wind (GUSTW) and the aircraft motion (GGVSPDB). Also shown for comparison is the spectrum for the IRU-provided aircraft motion (VSPD, dashed line). Data from DEEPWAVE flight 15, 3:40:00–3:55:00.

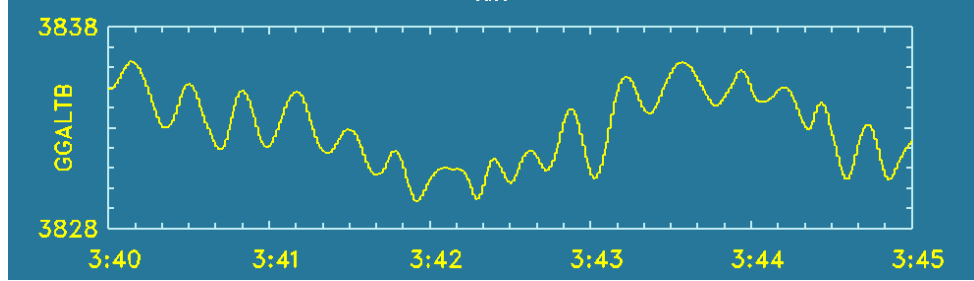


Figure 30: The GPS-measured altitude during a flight segment in very smooth air. Data from DEEPWAVE flight 15, variable GGALTB.

from the angle-of-attack contribution to the relative wind, and specifically from the measurements “ADIFR” and “QCR”, which exhibit noise spectra for frequencies above 1 Hz. In ADIFR, the noise is at a level that would arise from a white-noise signal with peak amplitude of 0.4 hPa or a random error of about 0.1 hPa. Similar noise is present in both QCR and QCF, so it may be linked to the nature of the transducers used or to some effect originating in the pressure lines connecting the transducers to the ports. The specifications for the pressure transducer that measures ADIFR assert a standard uncertainty of about 0.03 Hpa, and as sampled and digitized by the data system the resolution is about 0.002 hPa (± 70 hPa for 2^{16} range digital encoding). Thus the white-noise spectrum indicates a random error about three times greater than expected from the transducer characteristics. This needs further investigation because it imposes an important limit on capability to measure low-intensity turbulence.

2. The relative-wind contribution (GUSTW) and the aircraft-motion contribution (GGVSPDB) both have peaks at about 0.05 Hz, with cancelling contributions so that no peak occurs at that frequency in the resulting vertical wind. This peak arises from the autopilot controlling the aircraft, which has a noticeable oscillation about the set altitude with a period of about 15–20 s. A regular oscillation with this period is quite evident in Fig. 30.
3. The disagreement between VSPD and GGVSPDB even at low frequency is another indication that the IRU-provided value (VSPD) should not be used, because the GPS-measured value at low frequency is surely a better measurement than is possible from the IRU. (OMNISTAR corrections were present throughout this flight.)
4. The difference between WIC and GUSTW near 0.3 Hz, seen also as a possible effect in Fig. 28, indicates that both the relative wind and the aircraft motion are making contributions that add at these frequencies. The spectrum of vertical wind here may be suspect because it is not clear if the amplitude of this contribution from the GPS measurements should be trusted at these frequencies. [XXX exploration of high-frequency GGVSPDB might be useful if such are available; they were not present in the 25-Hz file I used.]

5.3 Timing of measurements

It is necessary that the different measurements entering the calculation of vertical wind be sampled at the same time. That is particularly difficult in the case of samples from the inertial reference system and GPS because they produce sample streams according to their own timing and not in response to requests from the aircraft data system. The variables involved in calculating the vertical wind are:

- Angle of attack, from transducers attached to radome ports via lines that can introduce small lags. No lag is currently used in processing.
- Pitch, from the IRU, transferred to the aircraft data system after some delay that must be removed in processing. The standard processing has a “delay” of -80 ms; i.e., the measurement is advanced in time by 80 ms so as to apply to a time later than when it is received. It is hard to understand how this is justified.
- Other attitude angles (heading and roll), which enter in minor ways if the aircraft is not flying a straight-and-level course. The timing of these can probably be neglected for calculations of vertical wind, but the standard variables are also given a time lag of -80 ms.
- True airspeed, measured using the pitot-tube measurement of dynamic pressure, used also with a measurement of temperature. While no lag is assumed for dynamic pressure, the reference total temperature for DEEPWAVE is RTHR1 (tentatively), and a time lag of -1 s is used for this measurement. (No lag is assumed for RTRL, another candidate for the reference temperature.)
- The vertical speed of the aircraft, taken for the preferred vertical wind variable from GGVSPDB, the variable produced by the Novatel GPS receiver employing OMNISTAR corrections when possible. This variable is only sampled at a rate of 5 Hz, and no time lag is used in processing.

It is useful to try to determine appropriate lags from the data and from appropriate maneuvers. For example, in pitch maneuvers (in which the pitch is alternately increased and decreased with typically a 10-s period) if the timing of measurements of pitch and angle-of-attack are not matched or if the measurement of vertical speed of the aircraft is not timed correctly there will be a residual measured vertical wind, so these maneuvers are particularly stringent tests of relative timing of the signals.

An approximate formula for the vertical wind w is

$$w = V \sin(\alpha - \phi) + w_p \quad (35)$$

where V is true airspeed, α is angle-of-attack, ϕ is pitch and w_p is the vertical velocity of the aircraft. This equation can be used to adjust relative timing among the signals to minimize

the variance in vertical wind during the pitch maneuvers. A good example is that from DEEPWAVE flight 15, 3:15–3:18 UTC. As initially processed using standard processing at the time of DEEPWAVE, the standard deviation in vertical wind through the pitch maneuvers was 0.4 m/s while the variance in vertical motion of the aircraft was 5.6 m/s. A long-standing criterion for acceptable pitch maneuvers is for less than 10% of the imposed velocity to enter the vertical wind, so by this criterion the test was successful. However, a plot of the vertical wind shows a clear match to the imposed velocity, so it is worthwhile to see if better results are possible.

Speed runs have been used to determine the sensitivity coefficients for determining α from the measured pressure differences on the radome, so the sensitivity coefficients should not be adjusted on the basis of the pitch maneuvers. The relative timing of the measurements entering Eq. 35, however, can be adjusted to determine if the residual vertical wind can be reduced. The sensors producing V and α are located close together and are processed in the standard manner by the data acquisition system, so these can be assumed to determine the reference time. However, the other variables ϕ and w_p are determined by independent systems and may have timing offsets from the standard measurements, so these are the variables whose lags are explored here.

The approach was to shift the measurements forward or backward in time and, using Eq. 35, recalculate the vertical wind. The best result obtained in this way was to shift PITCH forward 0.04 s and shift GGVSPDB backward 0.04 s. Almost as good was to shift PITCH forward 0.08 s and shift GGVSPDB backward 0.04 s. This reset the assumed lag in PITCH to zero while imposing a small lag of -0.04 s in GGVSPDB. For the purpose of this study, to avoid the phase lag produced by filters at the high-frequency limit, Savitzsky-Golay filtering was used for GGVSPDB with 4th-order polynomials applied over 25-measurement intervals to smooth the original measurements. The resulting standard deviation in WIX was 0.22 m/s, vs 0.23 with no shift in GGVSPDB, so it may be preferable to leave the assumed lag for GGVSPDB at zero to avoid the awkwardness of advancing the measurement in time.

With the assumed time lag in PITCH removed, the resulting measurement of vertical wind during the pitch maneuver is shown in Fig. 31. The standard deviation in measured wind through the pitch maneuvers is only 4% of the imposed vertical motion of the aircraft.

There is little signal corresponding to the imposed vertical motion or variations in pitch, and the measured standard deviation in vertical wind is about the same as that for measurements just before and just after the pitch maneuvers. It thus appears that the measuring system is able to remove the effects of the pitch maneuvers with essentially undetectable residual.

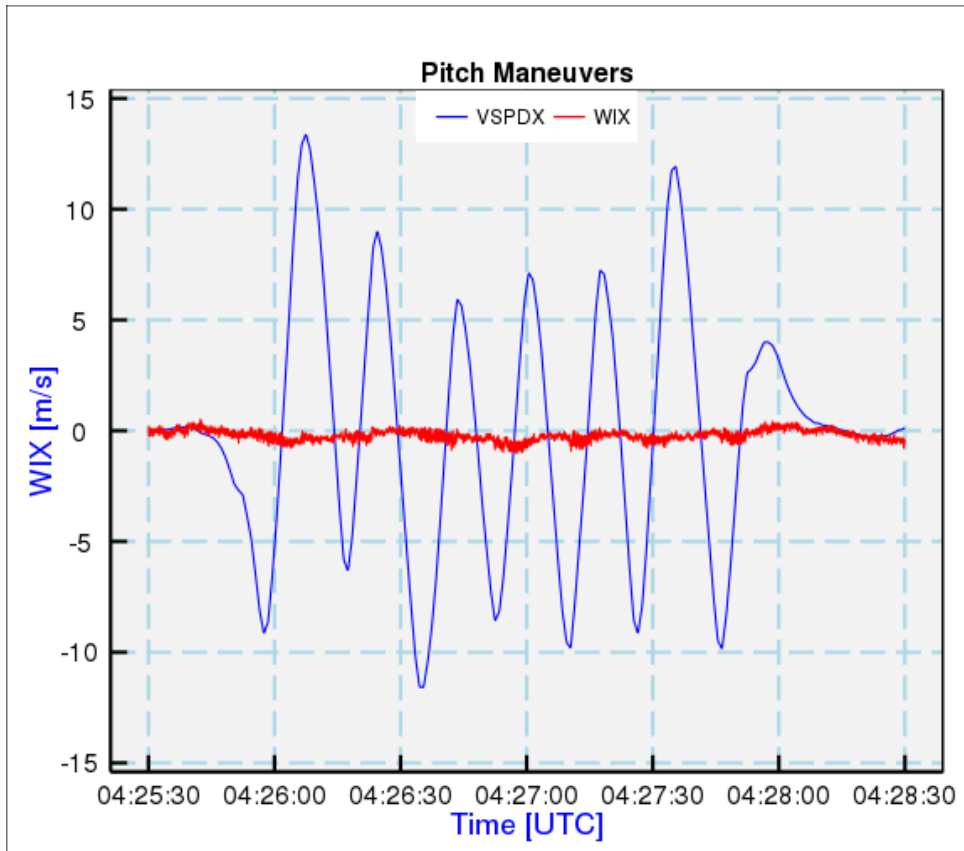


Figure 31: Vertical wind measured during pitch maneuvers. The variable VSPDX (which is GGVSPDB interpolated, filtered, and shifted) shows the vertical motion imposed on the aircraft, and WIX shows the resulting measurement of vertical wind.

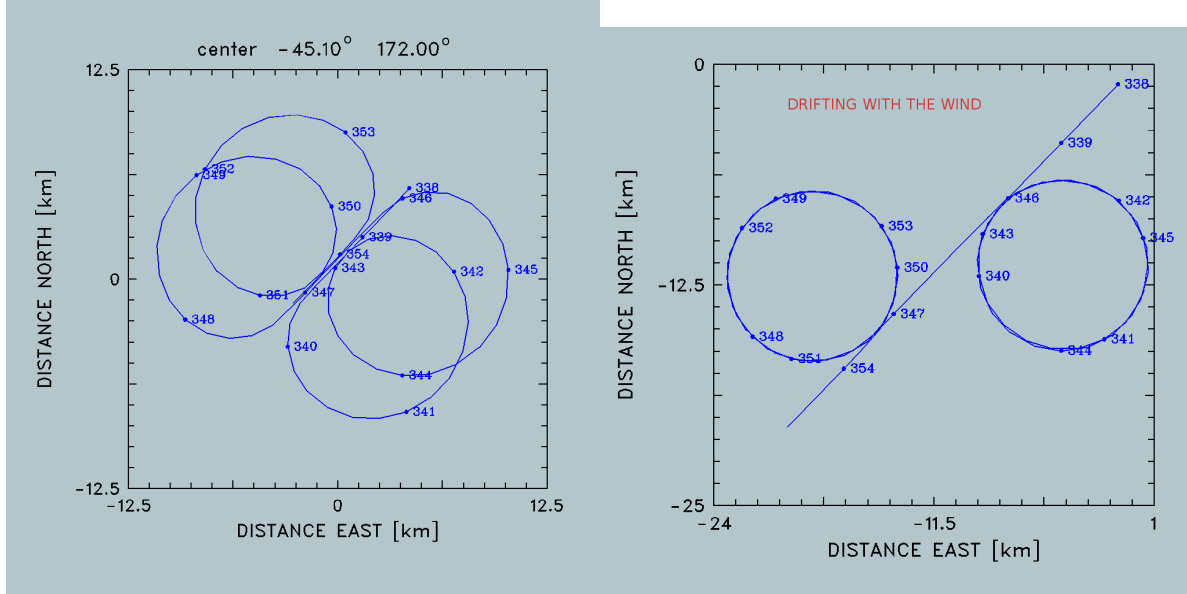


Figure 32: Example of circle flight pattern, DEEPWAVE flight 15, 3:38:30–3:54:30 UTC. Left side: normal flight track; right side, flight track plotted in a reference frame drifting with the horizontal wind.

6 Studies of the Horizontal Wind

6.1 Analysis of circle maneuvers

6.1.1 Data Used

During the DEEPWAVE project, some circle patterns were flown to help characterize and check the wind measurements. An example that will be used here was on flight 15, 3:38:30–3:54:30 UTC, as shown in Fig. 32. This and other circle maneuvers are discussed in this sub-section.

6.1.2 Constraints arising from the assumption that the wind is steady

If the wind remains steady around the turns, analyses of the measurements can lead to these results:

1. Wind can be determined from the GPS-measured ground speeds and the heading, with no other reference to the normal wind measurements.
 2. Determining a possible bias in the true-airspeed measurement TASX: If present, the measured windspeed will change from upwind to downwind direction.
 3. Determining biases in heading and sideslip: If present, the measured windspeed will change from crosswind-right to crosswind-left positions.

4. An offset in sideslip can be separated from an offset in heading by checking for the expected sign reversal in sideslip between left-turn and right-turn circles.

5. Departures from constant wind can be used to determine possible time shifts, especially by comparing results from left-turn and right-turn circles.

Each of these will be explored in this section. To get accurate circle patterns, it is important that the wind be relatively steady and non-turbulent and that the roll angle be maintained constant. For this flight segment, the left-turn circles had a roll angle of -26.92 ± 0.17 and the right-turn circles had roll angle 27.08 ± 0.12 , while the mean true airspeed for these circles was 153.6 ± 0.5 . Most of the standard deviation in true airspeed arose from the normal fluctuations created by the flight management system, as discussed in Sect. 5.2.2 (cf. Fig. 30). The steadiness of these measurements indicate that this maneuver was flown with good precision and symmetrically, so it will therefore be a good approximation to assume that these patterns are circular.

Finding the wind from GPS If it is assumed that \bar{u}_x , \bar{u}_y , TAS, and $\delta\psi$ (the two components of the horizontal wind, the true airspeed, and an assumed error in heading) are constant, then the expected ground-speed components will be:

$$\begin{aligned} v_x &= \bar{u}_x + TAS \sin(\psi + \delta\psi) \\ v_y &= \bar{u}_y + TAS \cos(\psi + \delta\psi) \end{aligned} \quad (36)$$

where ψ is the heading. These ground-speed components should then match the independently measured ground-speed components from the GPS. Figure 33 shows that these two sets of ground-speed components are in good agreement during the circle maneuvers and suggests that more detailed comparison should constrain the uncertainty in the measurements. The error between these expressions for the ground speed and the measured ground-speed components g_x and g_y then can be minimized to find the four constant parameters in (36), by using this expression as a measure of the error:

$$\chi^2 = \sum ((g_x - v_x)^2 + (g_y - v_y)^2) \quad (37)$$

The resulting best-fit values, with wind converted to wind direction \bar{v}_d and wind speed \bar{v}_s , are shown in Table 4.

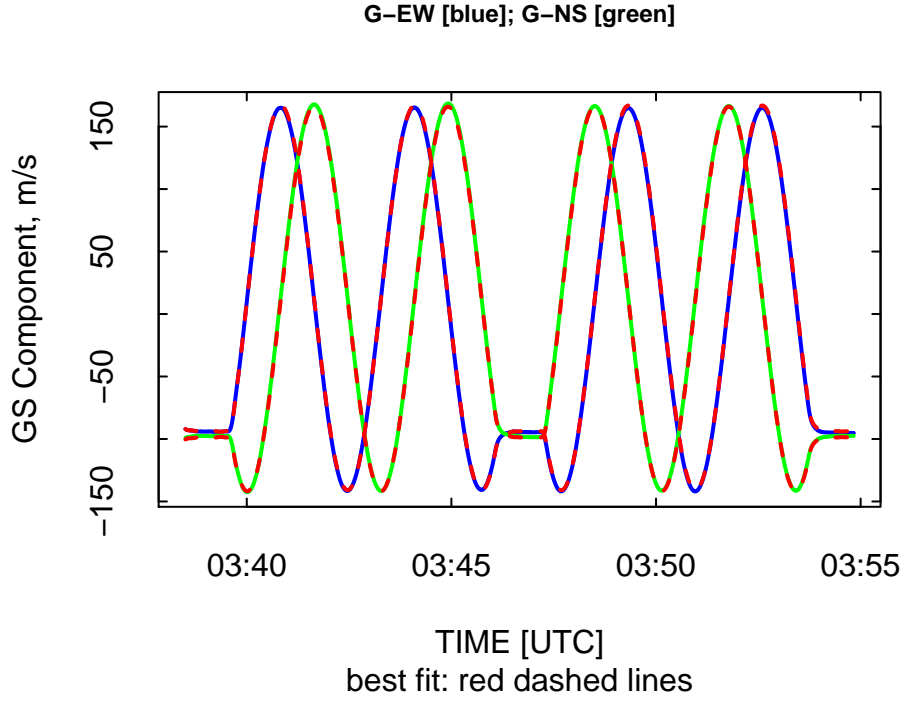


Figure 33: The ground-speed components measured by GPS (blue line, EW; green line, NS) and the corresponding results from the fit (red dashed lines) for the period of the circle maneuver.

	\bar{v}_d [$^{\circ}$]	\bar{v}_s [m/s]	TAS [m/s]	$\delta\psi$ [$^{\circ}$]	residual error [m/s]
all turns	223.1	17.7	153.8	-0.2	3.8
mean of measurements	223.1	17.8	153.6		
left turns	223.0	18.2	154.2	1.4	1.1
left-turn measurements	222.8	18.4	153.8		
right turns	222.5	17.1	153.7	-1.7	0.3
right-turn measurements	222.7	17.5	153.4		

Table 4: The results obtained by minimizing the error measure (37) for the full circle maneuver. The lines "mean of measurements", "left-turn measurements" and "right-turn measurements" are based on the wind measurements from the aircraft data system; other lines are based on minimizing (37) while using only the measured heading ψ .

Repeating this analysis for the left-turn circles and right-turn circles separately reveals a difference in the deduced wind that is about 1 m/s, as also listed in Table 4:

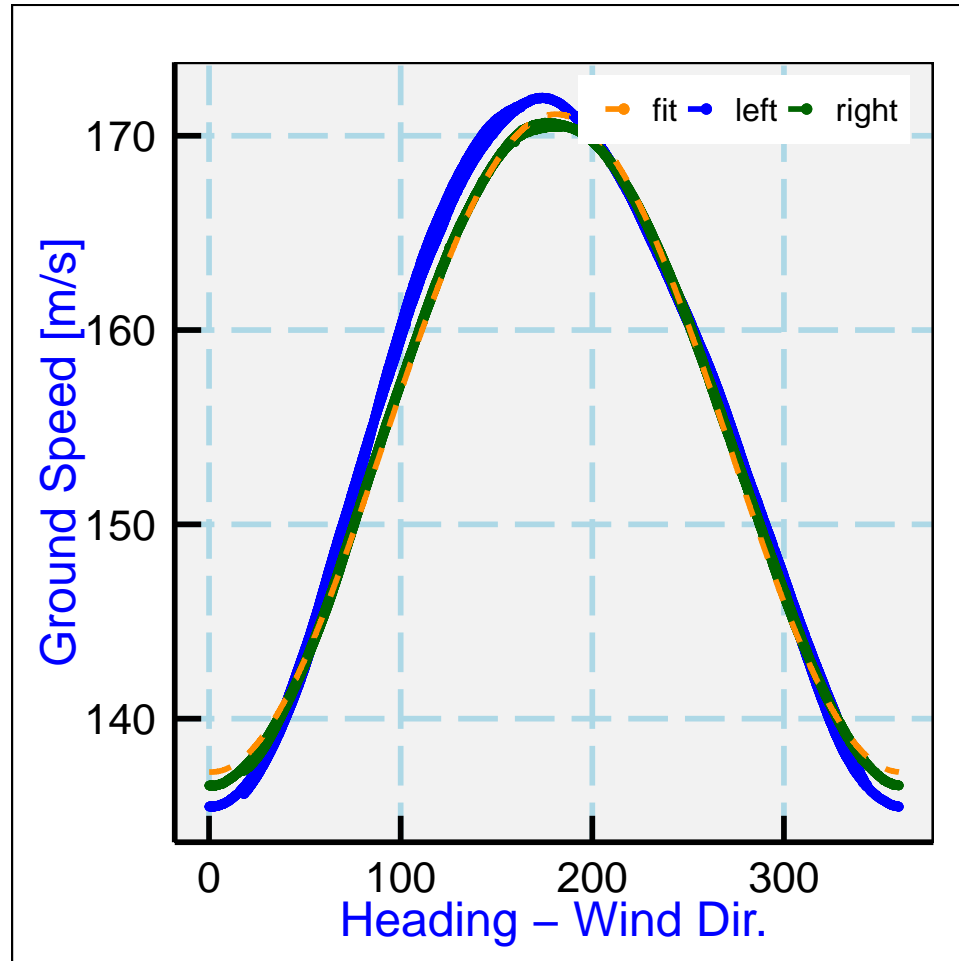


Figure 34: Ground speed (GGSPD) vs the angle of flight relative to the mean wind direction, for the circle pattern shown in Fig. 32. The dashed orange line represents a fit to a sinusoidal pattern for the right-turn segment only.

A plausible case can be made for this difference in wind speed being real. Figure 34 shows the GPS-derived measurements of ground speed. The amplitude of the variation around the circle is larger for the left-turn circles vs. the right-turn circles. The difference between maximum and minimum ground speeds is 36.5 m/s for left-turn circles but 34.1 m/s for right-turn circles, indicating a difference in wind speed of 1.2 m/s between the two turn directions.⁸ This difference is determined from the GPS-derived ground-speed measurements only and doesn't involve any other aspect of the wind-measuring systems on the aircraft. Even heading or sideslip can be in significant error without affecting this result because the analysis is based only on the maximum vs. minimum values of the ground speed. It is expected from instrument specifications that the measurement of ground speed is much less uncertain than this, so the suggested conclusion is that the difference in wind is real.

⁸If circles are fitted to the variations, the result is a difference of 0.8 m/s.

	\bar{v}_d [°]	\bar{v}_s [m/s]	TAS [m/s]	$\delta\psi$ [°]	residual error [m/s]
all turns	223.0	17.7	153.9	-0.15	1.0
mean of measurements	223.1	17.8	153.6		
left turns	223.0	18.2	154.2	-0.11	1.1
left-turn measurements	222.8	18.4	153.8		
right turns	222.5	17.1	153.7	-0.13	0.3
right-turn measurements	222.7	17.5	153.4		

Table 5: The same results as shown in Table 4 but with a time shift applied to the GPS measurements of ground track to advance the measurements by 840 ms.

The error in heading shown in Table 4 approximately reverses sign for right-turn vs left-turn circles. This error would arise if there is a timing error between the measurement of heading and that of ground speed, here obtained from the GPS system (variables GGVIEW and GGVNS) of about 0.46 s, because the turn rate in these turns is about $1.8^\circ/\text{s}$ so the indicated errors of about 1.5° suggest that, for both turn directions, advancing the GPS ground-speed measurements by about 0.8 s would remove the errors from all the circles. Fitting to minimize the standard error of the fits gave a minimum chisquare for a shift of 21 samples or $21 \times 40 = 840$ ms, as shown in Table 5. With this shift, the indicated errors in heading are all quite small and consistent with expected errors in heading ($<0.05^\circ$). The residual error for the right-turn circles, 0.3 m/s, is also very good; variations of this magnitude were present in the wind field and hence in TAS, so this is as low as could be expected.

The preceding fit used a constant true airspeed, but it is also possible to fit in the same way for an assumed error in true airspeed, by using $V = V_m + \delta V$ where V_m is the measured value and δV is an assumed error in that measurement. There is some small variation in measured true airspeed during the maneuver, perhaps created by the normal oscillation that results from the flight management system and is discussed elsewhere in this report, so this approach may be preferable. However, the resulting best-fit values were the same as those shown in Table 4, to the level of significance listed in that table.

Offsets in TAS and heading An alternate way of determining the offsets in airspeed and heading, which illustrates the value of the circle maneuver for developing these constraints, is to plot the dependence of measured wind speed v_s on the heading. The expected variation is for v_s to change by $2\delta V$ from upwind to downwind flight and by $2V\delta\psi$ from crosswind-right to crosswind-left flight direction (i.e., 90° right of downwind vs. 90° left). The net effect is to produce a variation in v_s given by:

$$v_s = \bar{v}_s + \delta V \cos \theta + V \delta\psi \sin \theta \quad (38)$$

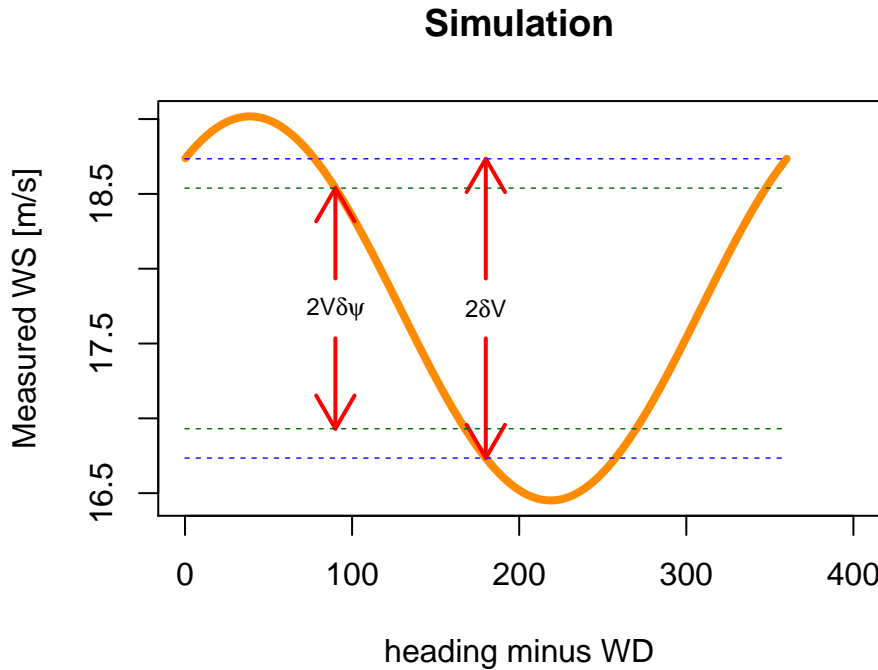


Figure 35: Predicted dependence of measured wind speed on direction of flight relative to the wind direction, for assumed errors of $\delta V = 1$ m/s and $\delta \psi = 0.3^\circ$.

	mean wind [m/s]	δV [m/s]	$\delta \psi$ [$^\circ$]	residual error [m/s]
left-turn circles	18.4	-0.6	0.29	0.23
right-turn circles	17.4	-0.2	0.03	0.2

Table 6: Fit results for the left-turn and right-turn circles as fitted by (38).

where θ is the difference between the heading and the wind direction.⁹ Figure 35 illustrates the expected dependence that would result from errors of $\delta V = 1$ m/s and $\delta \psi = 0.3^\circ$. The plot is constructed so that 0° corresponds to downwind flight and the difference between values at 0 and 180° corresponds to $2\delta V$, while the difference from 90 to 270° represents $2V\delta\psi$.

It is possible to determine δV and $\delta \psi$ by fitting (38) to observations. The measurements will be shown separately for the left-turn circles and the right-turn circles because a significant difference appears between them as discussed earlier. Figures 36 and 37 show the measurements, and the results of the fits are shown in Table 6.¹⁰

⁹As developed later, if there is non-zero sideslip the heading and the angle θ should be corrected by adding $\delta\beta \cos(\phi)$ where ϕ is the roll. Also, an error in sideslip will contribute to $\delta\psi$.

¹⁰The values for wind speed are slightly higher than those listed in Table 4, but the fit is slightly different and preferable in Table 6 because measured variations in V are included.

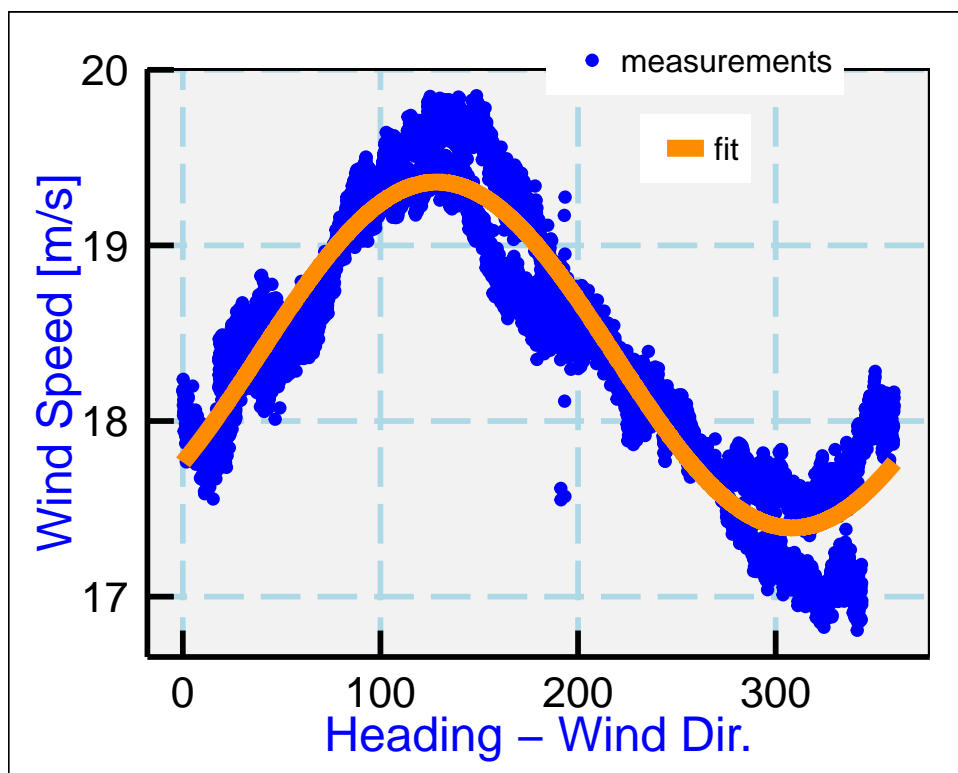


Figure 36: Measured wind speed from the left-turn circles in the circle pattern shown in Fig. 32, as a function of the difference between the heading and the mean wind direction.

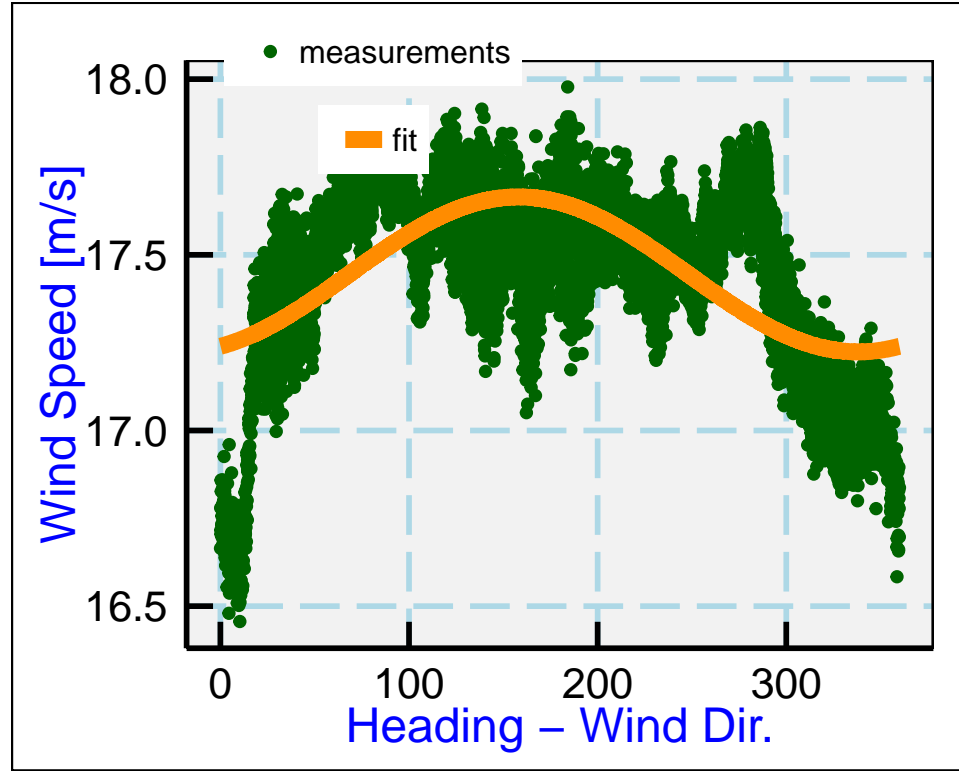


Figure 37: As for Fig. 36 but for the right-hand circles.

A difference of about 0.4° in heading offset translates to a change in wind speed of about 1 m/s at representative GV flight speeds, so small errors can be quite significant. Because the wind is more nearly uniform and the pattern of measurements is closer to a pure sinusoidal pattern for the right-turn circles, and because Fig. 34 shows better consistency for the two right-turn circles vs the left-turn circles, here the right-turn circles will be emphasized. They indicate that the wind measurements (with time-shifting as discussed above) are quite good, with indicated errors of only 0.2 m/s in true airspeed and 0.03° in heading. For the right-turn circles, the significant departures are for parts of the circles nearly into the wind direction, where the circles start and end, so it may be that those small deviations arise from imperfect flight patterns for those times. Without those parts of the curve, the indicated sinusoidal variation in Fig. 37 would be even smaller.

However, there is a complication in regard to heading that needs further exploration, so the next section will discuss that complication before offering a concluding assessment regarding uncertainty.

Offset in Sideslip In the preceding, the error $\delta\psi$ was discussed as an error in heading, but the error could also be one in sideslip. These errors are difficult to separate and normal reverse-heading maneuvers do not provide a separation. Furthermore, heading errors likely change during a flight because error terms undergo a Schuler oscillation and are also affected by horizontal accelerations such as occur persistently in turns like those in the circle maneuver. The error term determined as in the above tables should be represented by $\delta\psi'$ given by

$$\delta\psi' = \delta\psi + \cos\phi\delta\beta \quad (39)$$

where ϕ is the roll angle and $\delta\beta$ is the offset in sideslip. The sideslip calibration was determined in Sect. 4.2 from yaw maneuvers, but those maneuvers also cannot separate an offset in heading from an offset in sideslip so the first coefficient in the calibration, representing the zero offset, is not constrained well by these maneuvers. Because the dependence in (39) is on the cosine of the roll which is an even function, left and right turns are affected in the same way and also cannot distinguish the two terms in the equation.

Because the roll angle changes when circles are flown at different altitudes, results from different-altitude circles could be used to distinguish a sideslip offset from a heading offset. Perhaps a more straightforward test, though, is to compare the sideslip measurement in left vs right turns. The measurements of sideslip¹¹ are shown in Fig. 38. In the turns, some sideslip is introduced as the aircraft configuration remains slightly nose-up during the turn, and that sideslip should reverse sign by symmetry when the flight pattern changes from left-turn to right-turn circles. The lift required to maintain altitude would be the same if the roll angles were opposite, as they nearly are for these maneuvers (0.45° larger for right turns), and the angle of attack is also close to the same, so the expected sign reversal in sideslip can be used to determine the offset in sideslip.

```
## [1] " mean for maneuver: 0.01; left turns -0.30 and right turns 0.30"
```

The mean value for the full maneuver, and the average of the right-turn and left-turn circles, both require an offset of $0 \pm 0.01^\circ$ to be added to the sideslip if sideslip is to be symmetrical for left-turn and right-turn circles. This indicates that the first sideslip sensitivity coefficient representing the offset should be increased to 0.09. The required correction¹² to the combination of heading and sideslip was found in Table 6 to be -0.03° and, with a different analysis approach, in Table 5 to be $+0.02^\circ$, but it appears that the latter is a more reliable estimate because the distribution of measurements caused the former to be somewhat insensitive to forced changes in the angle. That indicates that the correction to heading (cf. (39)), calculated by taking into account the cosine of the roll in that equation, is 0.02° .

When this approach was applied to the C-130, it was found that for that aircraft the pitch could differ significantly for right vs. left turns, so a different approach taking into account the influence of all angles on vertical wind was also used. The transformation equations from [Lenschow and Spyres-Duran \[1989\]](#) (see also [Lenschow \[1972\]](#)), with some small-angle simplifications, lead to this equation for the vertical wind:

$$u_z = w_p + V(\sin\phi\tan\beta + \cos\phi\tan\alpha - \sin\theta) \quad (40)$$

where w_p is the vertical motion of the aircraft, V its true airspeed, ϕ the roll angle, β the sideslip angle, α the angle of attack, and θ the pitch angle. If it is assumed that the vertical wind is zero,

¹¹The sensitivity coefficients as determined in Sect. 4.2 have been used to construct this figure.

¹²Signs are such that the corrections needed are of opposite sign to the errors listed in the tables of this section

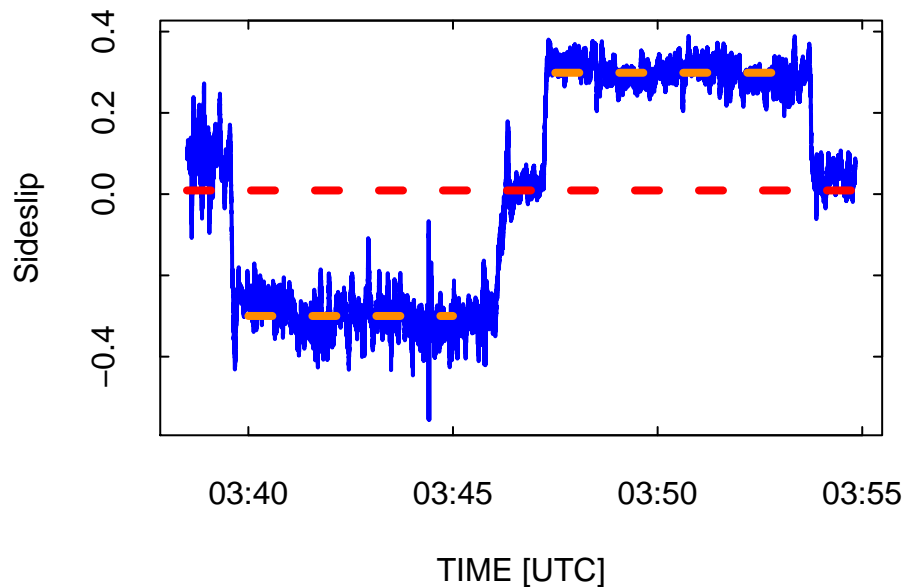


Figure 38: Measurement of sideslip during the circle maneuver from DEEPWAVE flight 15, with left-turn circles from 3:40:00 – 3:46:00 UTC, followed by a straight segment and then right-turn circles 3:47:30 – 3:53:40 UTC.

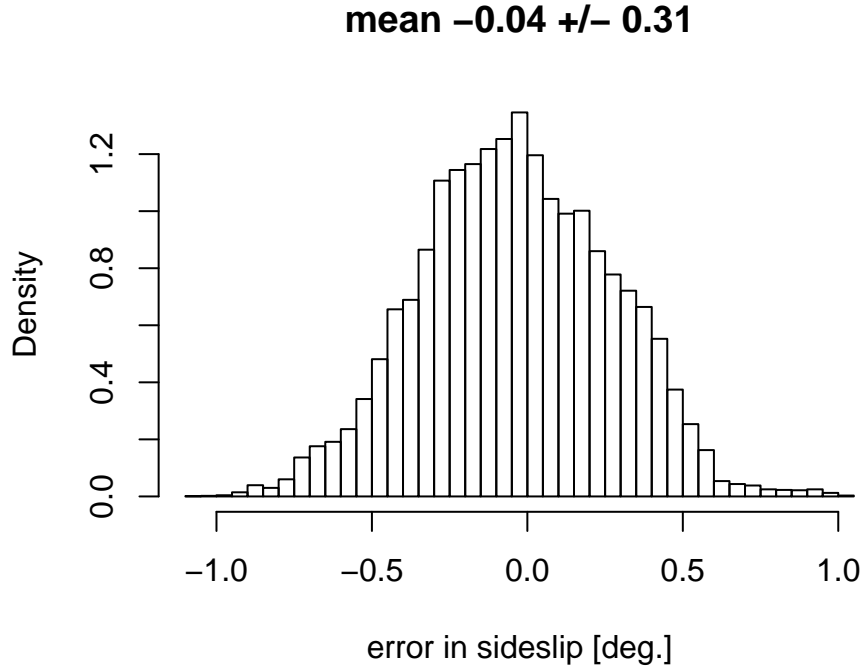


Figure 39: Distribution of measurements of sideslip error determined from (42) for all measurements from the circle maneuver.

this equation predicts that the sideslip angle will be β^* given by

$$\beta^* \approx \frac{\theta - \alpha \cos \phi - (w_p/V)}{\sin \phi}. \quad (41)$$

This is not valid in straight flight where the roll is near zero, but it provides a valid equation for sideslip in the case of steady turns. The key assumption is that the vertical wind is zero; a vertical wind of 0.1 m/s will typically increase the deduced sideslip from this equation by about 0.06° , so it is important that the circle maneuver be flown where there is no mean updraft. It is then possible to determine the offset in sideslip by comparing this prediction to the measured sideslip β_m :

$$\delta\beta = \beta_m - \beta^*. \quad (42)$$

```
## [1] "mean error in sideslip: -0.037 +/-0.002"
```

This result, indicating that $-0.037 \pm 0.002^\circ$ should be added to the sideslip, is very close to the indication from Fig. 38, where no offset was required.¹³ The uncertainty in the mean of this

¹³This is a result of iteration; first processing gave an offset of -0.07° but the sensitivity coefficients for sideslip were then adjusted and the flight data were reprocessed to make this offset zero in the netCDF files used for this analysis.

result is very low, and this result is more general, so this value will be used to correct the sideslip offset. This indicates that the sideslip sensitivity coefficients should be $\{e_0, e_1\} = \{0.129, 22.302\}$. Because this result is dependent on the vertical wind being zero, an uncertainty of at least 0.06° should be assigned to the first coefficient to recognize that the vertical wind might typically be 0.1 m/s in a region such as this.¹⁴

¹⁴The measured vertical wind was 0.1 m/s over the period of these circles.

6.1.3 Summary

The results obtained from analysis of the circle maneuvers are these:

1. The more uniform right-turn circles indicate that the measured true airspeed (TASX) with current LAMS-based pressure corrections is accurate to within expected uncertainty. The test indicates an error of -0.2 m/s which is within the expected ($\pm 0.3 \text{ m/s}$) uncertainty limits for TAS.
2. The offset in sideslip should be increased by 0.12° . The sensitivity coefficients for the radome should be changed to $\{0.21, 22.302\}$. Cf. the discussion in Section 4 and the summary section 4.4.2 at the end of that section.
3. The heading should be adjusted by the addition of -0.08° . This correction is linked to the preceding sideslip correction, such that both should be applied together and neither should be changed without considering the effect on the other. Their sum is the more reliable measure determined from the circle maneuvers.
4. The ground-speed measurements GGVIEW and GGVNS from the Novatel GPS need to be moved forward in time by 840 ms. Because the heading (THDG) in the processed files was moved forward by 80 ms, the indicated shift means that the difference between GGVIEW/GGVNS and THDG time lags should be 760 ms.¹⁵

6.2 The complementary filter

Wind measurements combine a measurement of relative wind with a measurement of aircraft motion to determine the air motion relative to the ground. The aircraft motion has long been measured by an IRS, and recently also by a GPS. These have complementary strengths: The IRS provides very good information on short-term motion but drifts with a characteristic period of more than an hour, while the GPS provides good absolute accuracy but sometimes is unable to receive the GPS signals and (except in differential-GPS mode) can have short-term errors that make short segments of the track look jagged. To take advantage of the strengths of each, a complementary-filter calculation was developed and implemented in the 1980s, but it was never documented publicly. This section is partly an attempt to remedy that and partly a suggestion to make some minor changes to how it is implemented. This discussion is complementary to the information in ProcessingAlgorithms.pdf, section 3.4, and contains additional detail as well as notes regarding implementation of changes.

To accomplish this combining of measurements, a low-pass filter, $F_L(\{GVNS, GVIEW\})$, is applied to the GPS measurements of groundspeed, $\{GVNS, GVIEW\}$, which are assumed to be valid for frequencies at or lower than the cutoff frequency f_c of the filter. Then the complementary high-pass filter, denoted $(1 - F_L)(\{VNS, VEW\})$, is applied to the IRS measurements

¹⁵This is a puzzling result needing further investigation because the Novatel GPS measurements have associated time stamps and so should be the best reference timings of any variables. However, the alternative of changing the THDG time lag to have the opposite sign is not reasonable because those measurements cannot be applicable to times later than when the measurements were made as would be required for an opposite-sign time lag.

of groundspeed, {VNS,VEW}, which are assumed valid for frequencies at or higher than f_c . Ideally, the transition frequency would be selected where the GPS errors (increasing with frequency) are equal to the IRS errors (decreasing with frequency). The filter used is a three-pole Butterworth lowpass filter, coded following the algorithm described in Busic, S. M., 1980: *Digital and Kalman filtering : An Introduction to Discrete-Time Filtering and Optimum Linear Estimation*, p. 49. The digital filter used is recursive, not centered, to permit calculation during a single pass through the data. If the cutoff frequency lies where both the GPS and INS measurements are valid and are almost the same, then the detailed characteristics of the filter in the transition region (e.g., phase shift) do not matter because the complementary filters have cancelling effects when applied to the same signal. The transition frequency f_c was chosen to be (1/600) Hz (but this value can be overridden via the “defaults” file). The Butterworth filter was chosen because it provides flat response away from the transition. The resulting variables for aircraft motion, {VNSC,VEWC}, are then each the sum of two filtered signals, calculated as described in the following box:

VEW = IRS-measured east component of the aircraft ground speed
 VNS = IRS-measured north component of the aircraft ground speed
 GVEW = GPS-measured east component of the aircraft ground speed
 GVNS = GPS-measured north component of the aircraft ground speed
 $F_L()$ = three-pole Butterworth lowpass recursive digital filter

$$\begin{aligned}\{VNSC\} &= \{VNS\} + F_L(\{GVNS\} - \{VNS\}) \\ \{VEWC\} &= \{VEW\} + F_L(\{GVEW\} - \{VEW\})\end{aligned}$$

This is straightforward and effective when both sets of measurements (IRS and GPS) are available. The approach in use becomes more complicated when the GPS signals are lost, as sometimes happens in sharp turns. Then some means is needed to avoid sudden discontinuities in velocity (and hence windspeed), which would introduce spurious effects into variance spectra and other properties dependent on a continuously valid measurement of wind. To extrapolate measurements through periods when the GPS measurements are not available, a fit is determined to the difference between the best-estimate variables {VNSC,VEWC} and the IRS variables {VNS,VEW} for the period before GPS reception was lost, and that fit is used to extrapolate through periods when GPS reception is not available. The procedure is described in section 3.4 of ProcessingAlgorithms.pdf.

The following provides more documentation of the fit procedure used to determine the Schuler oscillation. The errors are assumed to result primarily from this oscillation, so the three-term fit is of the form $\Delta = c_1 + c_2 \sin(\Omega_{Sch}t) + c_3 \cos(\Omega_{Sch}t)$, where Ω_{Sch} is the angular frequency of the Schuler oscillation (taken to be $2\pi/(5067s)$) and t is the time since the start of the flight. A separate fit is used for each component of the velocity and each component of the position (discussed below under LATC and LONC). The fit matrix used to determine these coefficients is updated each time step but the accumulated fit factors decay exponentially with about 30-min decay constant, so the terms used to determine the fit are exponentially weighted over the period of valid data with a time constant that decays exponentially into the past with a characteristic

time of 30 min. This is long enough to determine a significant portion of the Schuler oscillation but short enough to emphasize recent measurements of the correction. The procedures for accumulating the matrices for the fit are as follows:

Define u_G as the aircraft eastward velocity measured by the GPS and u_I the corresponding velocity measured by the IRS, so that the difference is

$$\delta u = u_G - u_I$$

If Ω_S is the Schuler oscillation period, with $\Omega_S = 2\pi t/T_s$ where $T_s = 5040$ s, τ_u is the time constant for the update (1800 s), t is the time from the start of the flight, and the measurement matrix is A_{ij} , then updated terms of the measurement matrix each sample period ($A'_{i,j}$) are (for δu):

$$\begin{aligned} A'_{0,1} &= A_{0,1}\left(1 - \frac{1}{\tau_u}\right) + \delta u \\ A'_{1,1} &= A_{1,1}\left(1 - \frac{1}{\tau_u}\right) + \delta u \sin(\Omega_S t) \\ A'_{2,1} &= A_{2,1}\left(1 - \frac{1}{\tau_u}\right) + \delta u \cos(\Omega_S t) \end{aligned}$$

The matrix components $A_{j,0}$ apply to the northward velocity component and so are represented by the same equations with δu replaced by δv . Similar matrices are calculated for latitude θ and longitude ϕ , based on the differences $\delta\theta$ and $\delta\phi$ between GPS and IRS measurements. The information matrix H_{ij} is calculated via

$$H_{i,j} = H_{i,j}\left(1 - \frac{1}{\tau_u}\right) + V_{i,j}$$

where $V_{0,0} = 1$, $V_{0,1} = V_{1,0} = \sin(\Omega_S t)$, $V_{0,2} = V_{2,0} = \cos(\Omega_S t)$, $V_{1,1} = \sin^2(\Omega_S t)$, $V_{1,2} = V_{2,1} = \sin(\Omega_S t) \cos(\Omega_S t)$, and $V_{2,2} = \cos^2(\Omega_S t)$. When the fit is needed, the matrix $H_{i,j}$ is inverted and the result multiplied by the measurement matrix $A_{i,j}$ to get the fit coefficients C_{ij} to use for predicting the results for δu , δv , $\delta\theta$, and $\delta\phi$ via equations like $\delta u = C_{0,1} + C_{1,1} \sin(\Omega_S t) + C_{2,1} \cos(\Omega_S t)$.

7 Uncertainty components and summary

7.1 Radome-based system

7.1.1 Preliminary estimates of uncertainty

Vertical wind Because the calculation of wind from the contributing measurements involves coordinate transformations, evaluation of the uncertainty in wind components involves difficult error propagation through the transformation matrices and other equations of Sect. 2.1. For application to straight-and-level flight (or flight where the intent is to remain level), simplified equations suffice for evaluation of the error terms, but it will also be useful to employ Monte-Carlo simulations to be sure that error contributions are propagated correctly.

For the vertical wind, Eq. 35 provides an approximate relationship that leads to straightforward error propagation, esp. if it is assumed that the angle of attack α and pitch ϕ are small angles so that

$$w = V(\alpha - \phi) + w_p \quad (43)$$

and errors in w (δw) can be related to the errors in the basic measurements (δV , $\delta \alpha$, $\delta \phi$, δw_p) by differentiating Eq. 43:

$$\delta w = (\alpha - \phi)\delta V + V(\delta \alpha - \delta \phi) + \delta w_p . \quad (44)$$

Correlations among these error terms are possible, so a full evaluation that does not assume independence among the errors leads to:

$$\begin{aligned} \langle (\delta w)^2 \rangle &= (\alpha - \phi)^2 \langle (\delta V)^2 \rangle + V^2 (\langle (\delta \alpha)^2 \rangle + \langle (\delta \phi)^2 \rangle) + \langle (\delta w_p)^2 \rangle \\ &\quad + 2((\alpha - \phi)(V(\langle \delta V \delta \alpha \rangle - \langle \delta V \delta \phi \rangle) + \langle \delta V \delta w_p \rangle)) \\ &\quad + 2V (\langle \delta \alpha \delta w_p \rangle + \langle \delta \phi \delta w_p \rangle) - 2V^2 \langle \delta \alpha \delta \phi \rangle \end{aligned} \quad (45)$$

The approximate magnitudes of these terms, discussed in detail below, are: $\delta V = 0.1$ m/s, $\delta \alpha = 0.1^\circ \simeq 2$ mrad, $\delta \phi \simeq 1$ mrad, and $\delta w_p = 0.03$ m/s. Other typical magnitudes are $V \simeq 200$ m/s, $\alpha \simeq \phi \simeq 2^\circ \simeq 3.5$ mrad. For these typical magnitudes, the only terms in Eq. 45 that make potentially significant contributions are:

$$\langle (\delta w)^2 \rangle = V^2 (\langle (\delta \alpha)^2 \rangle - 2 \langle \delta \alpha \delta \phi \rangle + \langle (\delta \phi)^2 \rangle) \quad (46)$$

The error in pitch arises from measurements from the IRU and is affected mostly by an initial offset during alignment and then further changes in this error arising from the Schuler oscillation and from accelerations that affect this error. The error in angle-of-attack, on the other hand, arises from a combination of measurement error from the pressure transducers and error in

the formula used to deduce angle-of-attack from the pressure measurements. However, the calibration of the radome to determine sensitivity coefficients for calculating angle-of-attack relies on matching the angle-of-attack to the pitch angle when the aircraft flies level and there is no vertical wind, so a calibration error in pitch would produce the same calibration error in angle-of-attack and errors that are positively correlated. This positive correlation would reduce the net variance in vertical-wind measurements, but other errors arising from sources like uncertainty in the measurements from the pressure transducers likely produce errors in angle-of-attack uncorrelated with those in pitch. The calibration procedure averages over long periods of flight during which any pitch error likely undergoes a Schuler oscillation and other changes, so the angle-of-attack calibration averages over such errors in pitch. Because of these arguments and the difficulty of determining the true correlation between these errors, it seems appropriate to drop the correlation term from Eq. 46 and then consider the result as an upper limit to the squared error in vertical wind.

It is possible to estimate the magnitudes of these errors from measurements. Because the GV instrumentation includes two identical inertial systems, the difference in measurements of pitch from those two systems provides one lower-bound estimate of the uncertainty in pitch. Measurements discussed in Sect. 2.2.2 suggest that, for periods when the roll of the aircraft was within 5° of zero, the difference between these redundant measurements was about 0.3 mrad. This is comparable to the estimated uncertainty in angle-of-attack, for which the variance spectra discussed in Sect. 5.2.2 suggest a random error of about $0.02^\circ \simeq 0.35$ mrad.¹⁶ The estimated uncertainties in angle-of-attack and pitch are thus comparable, and both influence the uncertainty in vertical wind. The rough-estimate uncertainty in vertical wind (to be refined later) is, for flight at about 230 m/s, about $230\sqrt{0.0003^2 + 0.00035^2} \simeq 0.1$ m/s. Other factors, esp. the radome calibration, need to be considered for a refined estimate.

Horizontal wind Errors in measurements affect the longitudinal and lateral components of the horizontal wind in different ways. For the longitudinal component, and relative-wind measurement has been calibrated by comparison to measurements of the single-beam LAMS to an estimated standard uncertainty of about 0.1 m/s (Cooper et al., 2014). The lateral component is measured using the sideslip angle, which is determined in a manner similar to that used to calibrate the measurement of angle-of-attack. However, the zero reference angle for attack is determined well by assuming that, on average in quiescent air, the vertical wind should be zero. No similar reference angle exists for sideslip, and trim adjustments to the aircraft can change the mean sideslip angle, so a different procedure with additional sources of uncertainty must be used. Two maneuvers are particularly effective for determining the zero reference for sideslip (at which angle the lateral horizontal component of the relative wind would be zero): (i) Reverse-heading maneuvers, where a straight leg is flown for a short time (typically 2 min), then the flight track reverses heading and flies back along the reverse heading, with the result that the wind component perpendicular to the longitudinal axis of the aircraft should reverse sign; or (ii) constant-bank circles flown drifting with the wind, for which the lateral component

¹⁶DEEPWAVE flight 15, 3:40–3:55, spectrum for AKRD, compared to simulated spectrum with random-noise amplitude of 0.07. As generated, this has mean of half the amplitude, so it corresponds to a standard deviation of $0.07/\sqrt{12} \simeq 0.02^\circ \simeq 0.35$ mrad.

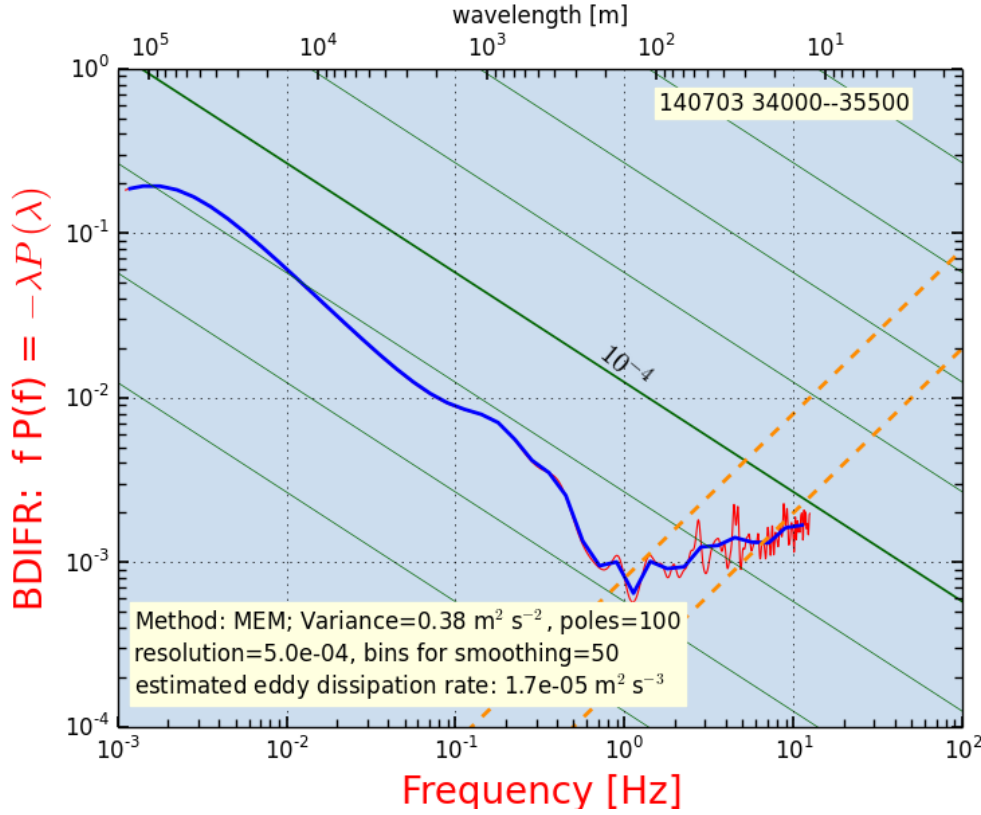


Figure 40: Variance spectrum for BDIFR for DEEPWAVE flight 15, 3:40–3:55 UTC. The dashed orange lines indicate expected white-noise spectra for respective standard deviations of 0.1 and 0.05 hPa. Units for $fP(f)$ are hPa² per logarithmic interval in frequency.

of the wind should exhibit a sinusoidal variation around the circle. Both can provide a reference for zero sideslip angle.

As for vertical wind, the GPS-measured components of aircraft motion relative to the Earth have uncertainty significantly less than that of the relative wind, so errors are dominated by those arising from the relative-wind components. The first-order equation for the lateral component of the relative wind (v_y), analogous to Eq. 43, is $v_y = V\psi$ where ψ is the sideslip angle, and V is known to typically 0.05% so the error is dominated by that in sideslip. For the random error, one limit is obtained as for angle-of-attack by examining the variance spectrum in calm conditions. However, BDIFR and SSLIP do not exhibit such pure noise spectra at high frequency as did ADIFR and AKRD. QCF and QCF show noise spectra representative of random errors of about 0.15 hPa, slightly higher than estimated for ADIFR. For BDIFR, an example is shown in Fig. 40.

The slope in the high-frequency region does not match that expected for a white-noise signal, for which the variance would be constant and in these plots, where the spectral density is multiplied by the frequency, the plotted line should increase linearly with frequency parallel to the orange dashed lines. Instead, the spectrum for BDIFR has smaller slope than this, looking perhaps as if the spectrum starts out at a point where a white-noise spectrum with standard deviation 0.1 hPa

element	source of uncertainty	bias	random error	δ_w bias	δ_w random
1	ADIFR transducer	0.07 hPa	0.002 hPa	–	–
2	$\text{AKRD} = c_0 + c_1(\text{ADIFR/QCF})$	0.03°	0.001°	0.12 m/s	0.04
3	BDIFR transducer	0.07 hPa	0.002 hPa	–	–
4	QCF transducer	0.34 hPa	0.01 hPa	<0.02	0.001
5	pitch	0.05°	0.02°	0.19	0.08
6	aircraft vertical velocity	0.03 m/s	<0.03 m/s	0.03	<0.03
7	horiz. velocity components of GV	0.03 m/s	<0.03 m/s	–	–
8	PSF transducer	0.10 hPa	0.001 hPa	–	–
9	ATX	0.3°	0.1°C	–	–

Table 7: Elemental contributions to the uncertainty in measurement of vertical wind.

would be appropriate, but then is filtered or otherwise smoothed¹⁷ so that at the high-frequency limit the equivalent white-noise standard deviation would be 0.05 hPa. The spectrum for SSLIP looks similarly filtered, with an equivalent white-noise spectrum somewhere in the range of 0.02°, similar to that characterizing AKRD. The resulting preliminary estimate of the standard uncertainty in the lateral component of the relative wind is about 0.1 m/s, as for the vertical wind. Like vertical wind, this needs to be refined for application to the Earth-relative wind by consideration of the uncertainty in the determination of sensitivity coefficients for sideslip, the uncertainty in heading (needed for transformation to coordinates fixed relative to the Earth), and other contributions to the net uncertainty in wind.

7.1.2 Elemental sources of uncertainty in vertical wind, tabulated

Next, we tabulate the elemental sources of uncertainty in the measurement of vertical wind and attempt to reconcile them with the indications of uncertainty in the preceding paragraphs. Table 7 summarizes the results. The following is a discussion of the individual elements in that table.

1. **ADIFR:** See Sect. 2.2.5 and Table 1. The uncertainty listed there is assigned to bias because it is likely a calibration uncertainty and the resolution and stability are much smaller than this bias. However, a calibration bias in this measurement does not affect the final wind measurement because the procedure in Sect. 4.1.2, determines the angle of attack from flight data in a way that can be considered a calibration of the measurement of angle of attack, and a bias in ADIFR would be reflected in a change in sensitivity coefficients determined in that section that would compensate for bias in ADIFR. Only random errors in ADIFR would propagate to the final measurement w , and such errors are

¹⁷perhaps by the response in the lines connecting the ports to the pressure sensors

thought to be negligible, so the propagated error for ADIFR is listed as negligible. The next item considers the determination of sensitivity coefficient for angle of attack and is the dominant contribution to uncertainty in w arising from the measurement of angle of attack.

2. **AKRD:** The calibration procedure of Sect.]4.1.2 effectively removes the effects of possible biases in ADIFR and QCR and instead introduces uncertainties arising from the coefficients $\{c_0, c_1\}$ in (28). The estimated bias and random error are those obtained by simulation in that section using the estimated uncertainties in the coefficients in (28). For propagation to vertical wind w , (22) indicates that the result is approximately $\delta w = V \delta \alpha$ where V is true airspeed TASX, with additional contributions from correlated errors involving V that are small in comparison to that listed. A typical value for V is about 220 m s^{-1} , leading to the listed elemental uncertainties in w arising from uncertainty in AKRD.
3. **BDIFR:** The sideslip angle has negligible effect on the vertical wind as long as the roll angle is small, so for measurements made during straight-and-level flight this contribution to uncertainty in vertical wind is negligible.
4. **QCF:** The values listed are the characteristics of the transducer. Application of the calibration procedure based on comparison to the laser air motion sensor (Cooper et al. [2014]) led to an alternate uncertainty estimate of 0.3 hPa . As in the case of ADIFR, the procedure to determine sensitivity coefficients removes any effect of bias in QCF by calibration in terms of the coefficients $\{c_0, c_1\}$ so the effect on bias in w is replaced by possible bias in those coefficients, as discussed for element 2. The effect of a random error in QCF of 0.01 hPa is, from (28), to introduce an uncertainty in angle of attack of about 0.0002° or a contribution to uncertainty in w of less than 0.001 m s^{-1} . QCF is also used to determine the true airspeed, which affects w , but the effect is negligible for the estimated uncertainty in QCF ($<0.2\%$ of the measured value of w , or 0.02 m s^{-1} for 10 m s^{-1} vertical wind).
5. **PITCH:** The bias listed is from the specifications for the IRU, assuming that the specification for “accuracy” from the manufacturer is best assigned to bias because it largely results from errors in initial alignment to determine the vertical direction and from errors introduced by accelerations during flight. The assignment depends on the interval considered, though, because Schuler precession will cause variation in this error with the Schuler-oscillation period of about 84 min and so for periods long compared to this will appear as a random-error component. The estimate of random error tabulated here arises from comparison between two identical IRUs during flight. The propagated uncertainty in w arising from the listed bias, at 220 m s^{-1} , is about 0.19 m s^{-1} .
6. **Aircraft Vertical Velocity:** The measurement used for vertical motion of the aircraft is discussed in Sect. 5.2. The values listed here are those specified for measurements when “OmniSTAR” corrections are available; if not, the values should be increased to about 0.1 m s^{-1} . This is likely a mixture of bias and random error, because the primary source is uncertainty in ionospheric corrections which will be persistent for important parts of

flights but likely to change at least from flight to flight. Because of the likely persistence of the error, it is assigned here primarily to bias.

7. **Horizontal Velocity Components of the Aircraft:** For straight-and-level flight, the measurement of vertical wind is not dependent on the ground-speed components, so these are listed as negligible.
8. **PSF:** The measured ambient pressure affects vertical wind only through the dependence of true airspeed TASX on PSF, as described in the document on [RAF processing algorithms](#), Section 4.7.1. Evaluation at typical values shows that the dependence of measured vertical wind on uncertainty in this variable is negligible. For example, TASX for PSF=300 hPa, QCF=80 hPa, and ATX=−40°C differs from that for PSF=300.1 by 0.03 m s^{-1} or about 0.01%, so this would also be the percentage change in vertical wind.
9. **ATX:** Temperature is needed to calculate TASX, but as for PSF the effect is negligible. This was tested as for PSF by evaluating at representative points. A representative result was that the listed bias in temperature would lead to a bias in TASX of about 0.05%, leading to a similar percentage change in the value of the vertical wind. This is negligible in comparison to other sources of uncertainty.

The result of adding the elemental sources of uncertainty in quadrature is a bias estimate of 0.23 m s and a random-uncertainty estimate of 0.09 m s^{-1} . It is unrealistic, though, to add the bias terms in this way. With such a small number of contributions, it is more likely that they will correlate so as to give addition or subtraction as a more realistic result. There is a more fundamental correlation, though. The calibration of angle-of-attack depends on the measurement of pitch, and for a given flight period over which the pitch bias remains constant the calibration of angle of attack will compensate for an error in pitch. For this reason, the bias arising from the calibration of angle of attack alone would be representative of flight segments for which the sensitivity coefficients have been determined. In that case, the representative bias in vertical wind would be 0.12 m s^{-1} , the bias in angle-of-attack. Furthermore, bias in pitch would not be a function of other measurements so the first coefficient in the representation of angle of attack, or c_0 in (28), also addresses the bias in pitch. If that bias stayed the same, only the bias in angle of attack would be needed to determine the bias in vertical wind.

This suggests that, when calculating vertical wind, the coefficient c_1 should be kept at the value determined in Sect. 4.1.2, (28). However, there is justification for adjusting c_0 to compensate for the varying bias in pitch, as long as it does not vary by more than about 0.05° , the estimated bias in the pitch measurement. The error in pitch is key to maintaining low uncertainty in the measurement of vertical wind, so anything that can reduce that error can lead to important improvement in the wind measurement. Investigations might examine if the CMIGITS IRU, which incorporates a Kalman filter to control the errors in its measurements, might provide better information. The APPLANIX IRU should provide another route to improvement. Also, a more ambitious project to incorporate adjustment of the measurement of pitch based on the expected changes produced by accelerations and the Schuler oscillation could lead to significant improvement.

7.2 Gust-pod system

8 Net uncertainty in measurements of wind

9 Potential for improvement in measurement of wind

Acknowledgements

The analyses reported here were mostly performed using R¹⁸R Core Team [2013], with RStudio¹⁹ RStudio [2009] and knitr²⁰ Xie [2013, 2014]. Substantial use also was made of the ggplot2 package²¹ Wickham [2009] for R.

¹⁸R Core Team (2014). R: A language and environment for statistical computing. R Foundation for Statistical Computing, Vienna, Austria. URL <http://www.R-project.org/>.

¹⁹RStudio (2012). RStudio: Integrated development environment for R (Version 0.98.879) [Computer software]. Boston, MA. Available from <http://www.rstudio.org/>

²⁰Xie, Y. (2013), “knitr: A general-purpose package for dynamic report generation in R. R package version 1.3,” Version 1.6 was used for this work. See also Xie, Y (2014), “Dynamic documents with R and knitr,” CRC Press, Chapman and Hall, 190 pp.

²¹H. Wickham. ggplot2: elegant graphics for data analysis. Springer, New York, 2009.

References

- W. A. Cooper, S. M. Spuler, M. Spowart, D. H. Lenschow, and R. B. Friesen. Calibrating airborne measurements of airspeed, pressure and temperature using a doppler laser air-motion sensor. *Atmospheric Measurement Techniques*, 7(9):3215–3231, 2014. doi: 10.5194/amt-7-3215-2014. URL <http://www.atmos-meas-tech.net/7/3215/2014/>.
- D. H. Lenschow. The measurement of air velocity and temperature using the NCAR Buffalo Aircraft Measuring System. Technical report, 1972. URL <http://nldr.library.ucar.edu/repository/collections/TECH-NOTE-000-000-000-064>.
- D. H. Lenschow and P. Spyers-Duran. Measurement techniques: air motion sensing. Technical report, 1989. URL <https://www.eol.ucar.edu/raf/Bulletins/bulletin23.html>.
- R Core Team. *R: A language and environment for statistical computing*. R Foundation for Statistical Computing, Vienna, Austria, 2013. URL <http://www.R-project.org>.
- RStudio. *RStudio: Integrated development environment for R (Version 0.98.879)*, 2009. URL <http://www.rstudio.org>.
- M. Schuler. The perturbation of pendulum and gyroscope instruments by acceleration of the vehicle. *Physik. Z.*, 24(16):344–357, 1923. URL <http://www.webcitation.org/6JBR8WNRq>.
- S. M. Spuler, D. Richter, M. P. Spowart, and K. Rieken. Optical fiber-based laser remote sensor for airborne measurement of wind velocity and turbulence. *Appl. Optics*, 50(6):842–851, FEB 20 2011. ISSN 1559-128X. doi: 10.1364/AO.50.000842.
- H. Wickham. *ggplot2: elegant graphics for data analysis*. Springer New York, 2009. ISBN 978-0-387-98140-6. URL <http://had.co.nz/ggplot2/book>.
- Y. Xie. *Dynamic Documents with R and knitr*. Chapman and Hall/CRC, Boca Raton, Florida, 2013. URL <http://yihui.name/knitr/>. ISBN 978-1482203530.
- Y. Xie. *knitr: A general-purpose package for dynamic report generation in R*, 2014. URL <http://yihui.name/knitr/>. R package version 1.6.